MECHANISTIC INSIGHTS INTO INTERFACIAL EVAPORATION SELECTIVE CRYSTALLIZATION FOR ONE-STEP HIGH-PURITY SALT EXTRACTION FROM SALINE WATER

YANG LIU

PhD

The Hong Kong Polytechnic University

2025

The Hong Kong Polytechnic University

Department of Civil and Environmental Engineering

Mechanistic Insights into Interfacial Evaporation Selective Crystallization for One-Step High-Purity Salt Extraction from Saline Water

Yang LIU

A thesis submitted in partial fulfillment of the requirements for the degree of

Doctor of Philosophy

Jun, 2025

Certificate of originality

I hereby declare that this thesis is entirely my own work and, to the best of my knowledge, contains no material previously published, written by another person, or submitted for any degree or diploma, except where proper acknowledgment is given.

Hong Kong, August 2025

_____

Yang LIU

Abstract

Extracting high-purity (>99%) salt resources from saline water through conventional separation processes typically involves multiple steps, high energy consumption, and substantial waste generation, posing significant environmental challenges. While interfacial evaporation crystallization has attracted growing interest for salt extraction due to its structural simplicity, effective renewable energy utilization, and direct solid product generation, its limited crystallization selectivity often results in co-crystallization of multiple salt species, yielding mixed or low-purity products that constrain practical applicability.

In this thesis, we propose a diffusion-driven selective crystallization strategy for high-purity salt production directly from source water with mixed salts. The essence of the strategy is to purposefully suppress non-ion-selective transfer processes (e.g., convection) so to make the difference in ion diffusion drive targeted ion to selectively move to the crystallization surface. As a proof concept, a floating porous membrane evaporator was designed, which universally achieved high-purity salt production (>99.10%) from saline water of mixed ions such as Na^+/K^+, Ba^{2+}/K^+ and Mg^{2+}/Li^+. Beyond experimental insights, this thesis further established a theoretical model that accurately predicted the boundary conditions essential for achieving species-selective crystallization, providing a foundational framework that will guide precise salt separation. The

diffusion-driven selective crystallization strategy opens a new horizon for selective crystallization and enriches the toolbox of high-purity salt production.

Building on this theoretical framework, we further developed a solar interfacial evaporation crystallizer designed for practical application scenarios. To enable sustainable extraction of high-purity sodium resources, the system is designed to utilize difference in Na^+/K^+ diffusion to drive selective NaCl crystallization from real seawater, with the entire process powered by solar energy. Utilizing this system, we successfully achieved direct, one-step production of NaCl crystals with a purity of 99.36% from real seawater at a rate of 28 $g \cdot m^{-2} \cdot d^{-1}$ under regular solar radiation, all without any pre- or post-treatment. Beyond high-purity NaCl, this system also successfully achieved one-step sustainable extraction of high-purity $BaCl_2$ and $MgCl_2$ from mixed source brine. This system provides an eco-friendly and low-cost solution for large-scale one-step resource extraction from saline water.

Drawing from insights into ion transfer from our previous findings, this thesis further introduces a novel advancement in interfacial evaporation selective crystallization by leveraging the difference in salt dissolution rate. The essence of the strategy is to purposefully regulate hydrated ion transfer driven by convection from the salt crystal surface to the source water so to utilize dissolution rate difference to achieve complete dissolution of unwanted salt in crystals. As a proof of concept, a solar evaporator was rationally designed,

enabling the sustainable selective crystallization of high-purity salt from source brine with mixed ions such as Na^+/K^+ and Li^+/K^+. Beyond its success in extracting resources from saline water, this strategy can also directly extract high-purity salt crystals from mixed solid salts, such as KCl/NaCl and KCl/LiCl, in a single-step dissolution process. Finally, its real-world applicability was demonstrated by achieving 99% pure KCl production at a rate of 36.60 $g \cdot m^{-2} \cdot d^{-1}$ from real fly ash leachate. This strategy expands the mechanistic foundation of selective crystallization, and offers a versatile, low-energy approach for sustainable and high-purity salt separation.

In summary, this thesis addresses and resolves critical challenges in the efficient extraction of high-purity salts from saline water by interfacial evaporation selective crystallization technology. The findings provide a foundation for the development of sustainable, selective crystallization systems and will drive future advancements in resource recovery and industrial-scale applications in salt separation.

Acknowledgement

Looking back on my fulfilling doctoral journey, I am deeply grateful for the unwavering support and selfless help from my mentors, family members, and friends. It is with the deepest sincerity that I express my heartfelt thanks to all of you.

First and foremost, I want to extend my deepest gratitude to my parents. From childhood, you created a world of security and unconditional love, allowing me to pursue my dreams without distraction. Your tireless work ethic and infinite love have been the purest gifts in my life. Your hard work, kindness, and perseverance have been a guiding light and a lifelong inspiration for me. Your unwavering belief in me has been the foundation of everything I have achieved. You are my warmest harbor, and I will always love you dearly.

I want to sincerely thank my PhD supervisor, Professor Peng Wang. Thank you for the invaluable opportunity to pursue my doctoral degree and for your meticulous guidance and steadfast support throughout this journey. Your profound knowledge, academic rigor, and unwavering patience were invaluable. You always listened to my doubts, helped me dissect complex problems with clear thinking, and constantly encouraged me to be innovative. Your teachings are the most precious asset on my research path.

I am also immensely grateful to Professor Yi Jiang for his guidance and friendship. He has been both a mentor and a friend, providing crucial advice

and support whenever I faced challenges in my work and studies. His insights helped me solve many practical problems. My sincere thanks also go to Professor Wenbin Wang and Professor Hanchao Zhang. Despite their demanding schedules, they dedicated a significant amount of time and energy to guiding my research. Their deep professional expertise and selfless dedication have deeply inspired and motivated me. I also want to thank my master's supervisor, Professor Senlin Shao, for his rigorous training and meticulous cultivation. His rigorous and meticulous guidance laid a solid foundation and developed the research skills essential for my doctoral studies.

To my dear friends: Jiacong Xiang, Yuming Chen, Chuanjing Lin, and Bin Nie. In moments of confusion, frustration, and even sadness, you patiently listened to my concerns, offered warm comfort, and provided powerful encouragement. Your genuine friendship has been a vital source of strength for me.

A special thank you to Amy. Her exceptional professional abilities are matched by an admirable character. She faces every challenge with a warm smile and solves problems with remarkable attention to detail. She is always gentle and warmhearted, a ray of sunshine to everyone around her. I am so fortunate to work with her during my PhD studies. Our collaboration and mutual encouragement are among the most cherished memories.

Thank you to Canjie Lin and Chao Wang for their companionship. The path

of research can be lonely, but you both brought so much joy into my life. The time we spent talking, complaining, and encouraging each other was a highlight of my youth. You are not only like-minded research partners but also my best confidants.

I am grateful to the students who have walked alongside me: Jinjuan Chen, Yekai Lian, Taoli Wu, Zhenle He, and Xinyang Xie. Their youthful energy and strong support infused my research and daily work with motivation. Every day I spent with them made this journey richer and more fulfilling.

A special note of thanks to the research assistants who provided invaluable help in the lab and in the office: Weiting Sun, Lin Liu, Jiaping Chen, Zihan Zhang, and Donghang Jiang. Their hard work and professional assistance were essential to the smooth progress of my research. I also want to thank the dedicated staff of the CEE. Their efficient and professional support provided a solid foundation for our work.

Lastly, I want to thank myself. Thank you for the patience to overcome countless experimental failures, the perseverance to revise this manuscript, and the dedication to complete the final data analysis late into the night. Thank you for having the courage to think independently, to tackle academic challenges head-on, and to maintain a passion for research even in moments of doubt. This doctoral journey has not only imparted specialized knowledge but has also shown me how to find growth in adversity and strength in solitude.

This resilience and independent spirit are the most valuable assets I will carry forward in my life.

I know that I could not stand here today by my own efforts alone. This achievement is a testament to the hard work, wisdom, and expectations of everyone who has loved and supported me. Your companionship, encouragement, and help have carried me to this point. I will hold this profound kindness in my heart forever.

Table of contents

List of abbreviations

Nanofiltration (NF)

Thenoyltrifluoroacetone–trioctylphosphine oxide (TTA–TOPO)

Lithium manganese oxide (LMO)

Mechanical vapor recompression (MVR)

Single/multiple-effect evaporation (SEE/MEE)

Single/multi-stage mechanical vapor recompression (SVR-MVR)

Zero liquid discharge (ZLD)

Diffusion-driven selective crystallization strategy (DiSC)

Molecular dynamic (MD)

Simple point charge (SPC/E) model

Particle-particle-particle-mesh (PPPM)

12-6 Lennard-Jones (LJ) potential

Periodic boundary conditions (PBC)

Large-scale atomic/molecular massively parallel simulator (LAMMPS)

X-ray diffraction (XRD)

De-ionized (DI) water

Water content angle (WCA)

Inductively coupled plasma-optical emission spectrometry (ICP-OES)

Glass fiber membrane (GFM)

Polystyrene (PS) foam

Péclet number (Pe)

Solubility product constants (Ksp)

Dissolution rate (DR)

Municipal solid waste (MSW)

Energy-dispersive X-ray spectroscopy (EDS)

List of figures

List of tables

1 Background

1.1 Necessity of extracting high-purity salt from saline water

As global modernization accelerates, high-purity salts are becoming indispensable across diverse industries, including chemical manufacturing[1-3], energy storage[4-6], and pharmaceuticals[7-9].For example, the demand for high-purity LiCl (typically >99.5%), a critical component in electric vehicle batteries and renewable energy storage, is projected to increase by over 500%, reaching an astounding 500,000 metric tons by 2030[10]. Similarly, the demand for high-purity KCl (generally >99%)—essential for producing high-quality potassium fertilizers—is expected to rise by 30% over the next decade, driven by growing food production needs[11]. These trends underscore the escalating global reliance on high-purity salts for various essential applications.

Despite escalating resource demand, terrestrial reserves are rapidly depleting and are progressively failing to meet these needs[10,11]. For example, land-based lithium reserves are projected to be exhausted by 2080, based on consumption rates anticipated by 2050[10]. Beyond resource scarcity, extracting salt resources from land-based sources also carries significant environmental risks[12]. Studies document that salt mining activities elevate toxic heavy metal concentrations in sediments, particularly arsenic (As) and lead (Pb). In the Urmia Salt Lake (USL) case, sediment analysis revealed an average arsenic concentration of 15.2 ± 8.8 $mg \cdot kg^{-1}$ (range: 6.4-24.0 $mg \cdot kg^{-1}$). These levels

exceeded Earth's crust background values (1.5-2 mg·kg^{-1}) by 7.6 to 10 times, and surpassed safe thresholds[13]. As environmental awareness grows and global sustainability efforts intensify, there's a pressing need to explore alternative solutions that can meet resource demands while minimizing harmful environmental impacts.

Considering these growing challenges, attention has increasingly shifted to the vast and largely untapped resources in water. Oceans, for example, contain an estimated 230 billion tons of lithium. This quantity is four orders of magnitude greater than land-based lithium reserves, positioning seawater as a potentially massive resource to meet global demand[10]. Besides these natural sources, waste brines generated by industrial processes (e.g., desalination, mining, chemical production) and various other human activities also contain valuable salts that need extraction for both essential resource recovery and environmental impact mitigation[14]. Meanwhile, compared to traditional terrestrial mineral extraction, extracting salt resources from aqueous sources generally does not involve strong acid-base treatments, as the salts are already dissolved in the solution. This not only simplifies the extraction process but also significantly reduces the use of harmful chemical reagents, which greatly lowers the risk of environmental pollution and ecological damage. Therefore, extracting high-purity salts from water sources offers both a sustainable method of resource recovery and a significant contribution to environmental preservation.

While the salts present in water offer a crucial solution to resource scarcity, their complex coexistence in water presents great challenges for direct resource utilization. Take seawater, for example, as a potential chlor-alkali feedstock due to its high concentration of NaCl (26.5 $g \cdot L^{-1}$), is invariably coupled with $MgCl_2$. However, during direct electrolysis of seawater, severe $Mg(OH)_2$ scaling forms on cathode surfaces due to the coexistence of $MgCl_2$, leading to substantial current efficiency losses. In a single-compartment cell with 0.053 M $MgSO_4$ (seawater-level Mg^{2+}) at 0.1 $A \cdot cm^{-2}$, the formation of $Mg(OH)_2$ scaling reducing the electrochemically active surface area (ECSA) by 44%[15]. Similarly, when utilizing KCl extracted from brine as a fertilizer, the coexisting NaCl also poses significant challenges[16,17], as it can induce phytotoxicity to adversely affect plant growth and yield.

These challenges associated with complex mixed salts in water are exacerbated when dealing with waste brines containing highly toxic metal ions[18,19]. For instance, industrial effluents from mining and electroplating often contain heavy metals like Cd^{2+} and Hg^{2+}[20,21], Their concentrations can exceed 0.15-0.3 and 0.02-0.05 $mg \cdot L^{-1}$, respectively. These levels far surpass WHO safety thresholds of 0.003 $mg \cdot L^{-1}$ for Cd^{2+} and 0.006 $mg \cdot L^{-1}$ for Hg^{2+}, which could lead to severe toxicity in extracted salt products[22].

Consequently, the effective separation of high-purity salts from complex mixtures in water is essential for alleviating resource scarcity and addressing

the growing demands of economic and environmental sustainability.

1.2 Challenges of high-purity salt extraction from saline water

Salt resources in water—including seawater, salt lakes, and waste brines—exist as complex mixtures of dissolved ionic species such as Na^+, K^+, Mg^{2+}, Cl^-, Ca^{2+}, and SO_4^{2-}. This complexity presents significant challenges in separating and extracting high-purity salts. Firstly, some coexisting salts in water share highly similar physicochemical properties, making effective separation challenging and ultimately lowering salt purity. Secondly, complex ionic interactions between these ions and different separation materials can lead to the damage of separation material and hinder the separation processes. Moreover, current separation methods often demand high energy and equipment investment, increasing costs and reducing the sustainability of resource extraction.

1.2.1 Physicochemical similarity of coexisting salts

The coexistence of salt ions with highly similar physicochemical characteristics is common in various water sources. For instance, in natural brine systems, such as salt lakes, valuable ions like Li^+ and K^+ commonly coexist with high concentrations of Na^+ (Table 1.1)[23].These ions exhibit the same charge, similar hydrated radii, and comparable solubility[24], presenting substantial challenges in the extraction of high-purity salts using conventional methods. For example, although membrane separation techniques have been

widely applied in the field of ion separation, the hydrated radii of Li^+, Na^+ and K^+ (Li^+ 0.38 nm, Na^+ 0.36 nm, and K^+ 0.33 nm) in water are nearly identical, differing by less than 15.2%[1]. This difference falls below the selectivity threshold of most commercial nanofiltration membranes (NF), thereby hindering the direct extraction of high-purity LiCl.

Table 1.1 Chemical compositions of salt lakes in China[23]

Salt lake	Chemical composition (%)						
	Na^+	K^+	Mg^{2+}	Ca^{2+}	Li^+	Cl^-	SO_4^{2-}
Qarham	2.37	1.25	4.89	0.051	0.031	18.8	0.44
Da Qadam	6.92	0.71	2.14	-	0.016	14.64	4.05
East Taiji	5.13	1.47	2.99	0.02	0.085	14.95	4.78
West Taiji	8.26	0.69	1.99	0.031	0.022	16.17	1.14
Yiliping	2.58	0.91	1.28	0.016	0.021	14.97	2.88
Zabuye	10.01	3.16	0.002	-	0.08	12.06	2.98

Similarly, the selective extraction of K^+ from seawater or salt lakes also faces great challenges. In seawater, the concentration of Na^+ is approximately 10,800 mg·L^{-1}, which is about 28 times higher than the concentration of K^+, typically around 380 mg·L^{-1}. However, both K^+ and Na^+ are monovalent alkali

metal ions with similar size, leading to very low selectivity for conventional separation methods aimed at high-purity KCl extraction from seawater (membrane separation factor < 3[25-27]).

Thus, the physicochemical similarities among salt ions underscore the urgent demand for advanced separation technologies to address these fundamental challenges and facilitate high-purity salt extraction.

1.2.2 Corrosion, osmotic pressure, and scaling in saline aqueous systems

Besides the challenges of ion separation, saline aqueous systems impose severe challenges to extraction operations through three primary pathways: corrosion, osmotic pressure, and scaling. Firstly, saline water often contain high concentrations of corrosive chloride ions[28], typically exceeding 10,000 $mg \cdot L^{-1}$. These aggressive ions can cause sustained and severe damage to systems made of steel or other metals prone to corrosion, leading to reduced equipment lifespan, increased maintenance costs, and potential safety risks. Since steel corrosion is an electrochemical process, elevated temperatures accelerate the reaction. The Arrhenius-type relationship between temperature and corrosion rate (*CR*) follows[29,30]

$$CR = A \exp\left(-\frac{E_a}{RT}\right) \qquad \text{Equation 1.1}$$

where *CR*: reaction rate, *A* is the Arrhenius pre-exponential factor, *Ea*: activation energy, *R*: gas constant, *T*: Absolute temperature.

For instance, Mechanical vapor recompression (MVR) systems, commonly used in evaporative crystallization processes to extract solid salt resources from saline water at high temperatures, are particularly susceptible to chloride corrosion. This corrosion not only compromises the longevity and reliability of the machinery but also contributes to operational inefficiencies.

Osmotic pressure presents another fundamental barrier for salt extraction. For saline water, osmotic pressure arises predominantly from dissolved salt ions and can be quantified by the Van't Hoff equation:

$$\pi = iCRT \qquad \text{Equation 1.2}$$

where π is the osmotic pressure (Pa), i is van't Hoff factor, C is the salt molar concentration ($mol \cdot m^{-3}$), R is the gas constant (8.314 $J \cdot mol^{-1} \cdot K^{-1}$), and T is the temperature (K).

Osmotic pressure generally poses a critical thermodynamic barrier in membrane-based salt separation processes such as NF and electrodialysis. For example, for salt extraction from seawater, where the total dissolved solids (TDS) concentration averages 35,000 $mg \cdot L^{-1}$, the osmotic pressure is approximately 27 bar at 25°C[31]. To counteract this pressure, membrane filtration systems must operate at hydraulic pressures 1.5-2.5 times higher than osmotic pressure. Therefore, diluted brine is often used in the NF process for $LiCl/MgCl_2$ separation to reduce osmotic pressure, allowing for the use of relatively low operating pressures[32,33]. However, this leads to increased energy

consumption and operational complexity.

Salt scaling is another common issue encountered when extracting high-purity salts from saline water[34,35]. In the membrane separation processes, sparingly soluble salts (e.g., $CaSO_4$, $CaCO_3$, $BaSO_4$) often crystallize and deposit onto membrane surfaces or within pore structures, leading to salt scaling. This can significantly impair the efficiency of filtration and separation systems by blocking the flow pathways[36,37]. For instance, during NF, inorganic $CaCO_3$ scaling resulted in a marked decrease of over 40% in the retention of solutes in feedwater[36,37]. Meanwhile, as scaling accumulates, higher transmembrane pressures become necessary to maintain the desired permeate flux, significantly increasing energy consumption. For instance, in a salt production system designed to extract resources from mine wastewater, salt scaling significantly increased energy consumption per ton of salt produced by approximately 21%[38].

1.2.3 Energy and cost intensiveness

Besides the separation challenges posed by complex coexisting salts, the application of current salt separation technologies for high-purity salt extraction from water is often limited by high energy consumption and substantial capital investment. Thermal-driven evaporation crystallization technologies, for example, widely used for brine processing, face significant energy and capital challenges. Even with efficiency improvements like latent heat recycling, MVR

still consumes 20 to 60 kWh·t^{-1} of salt produced, which is significantly higher than the energy consumption in conventional mining methods[39,40]. Furthermore, MVR systems necessitate corrosion-resistant titanium alloy components, costing $2-5 million per unit. Scaling issues in high-salinity brines further escalate maintenance costs by 20-30%[41].

Similarly, membrane separation technologies, such as NF, offer a promising alternative for selective salt extraction[42,43]. However, NF often requires pressure-driven operations (typically range from 3.5 to 16 bar), demanding significant energy input and capital investment. Furthermore, long-term operation renders NF systems susceptible to salt scaling and membrane fouling, which require costly cleaning procedures and shorten the membrane's operational lifespan[35].

1.3 Research objective

To address these challenges in resource extraction, this thesis aims to develop selective high-purity (>99%) salt crystallization technology for the efficient and sustainable extraction of salt resources from water. Our specific objectives, structured across distinct phases, are outlined below:

Objective 1: Unlocking selectivity through the difference in ion diffusion

Current evaporation crystallization methods often struggle with selectivity, making it difficult to extract target salts with high purity. During interfacial evaporation, salt ions diffuse differently under a stable concentration gradient

due to their varying diffusion coefficients. We aim to exploit these differences in ion diffusion to develop a novel selective crystallization strategy. To achieve this, we've designed a custom floating porous membrane evaporator. With the entire evaporation process powered by sustainable energy, this membrane is specifically engineered to suppress non-selective ion transfer, enabling selective salt crystallization driven by ion diffusion differences. Using this evaporator, we'll demonstrate the one-step selective crystallization of high-purity salts from various complex and mixed-ion solutions. Furthermore, we'll develop a comprehensive theoretical model to accurately predict the boundary conditions for species-selective crystallization, which will serve as a foundational tool for rational design and optimization. Ultimately, this thesis seeks to expand the possibilities for high-purity salt production, positioning our diffusion-driven selective crystallization strategy as a transformative and robust final step in various industrial separation processes.

Objective 2: Translating theory into practice: Na^+/K^+ separation of real seawater

Building upon the foundational understanding gained from Objective 1, this stage moves beyond theoretical exploration to practical application. As sodium is a vital element in numerous industrial processes and is abundantly available in seawater, the efficient separation of Na^+ and K^+ is crucial for the extraction of high-purity NaCl from real seawater. To achieve efficient and sustainable

one-step high-purity NaCl production, we will develop a novel solar crystallizer which can effectively mitigate non-ion-selective transfer processes to utilize the difference in ion diffusion for solar-driven selective crystallization. Initially, we will demonstrate the system's excellent Na^+/K^+ separation performance and high-purity NaCl production efficiency of simulated seawater under regular solar radiation. Subsequently, we aim to demonstrate the broad applicability of this solar crystallizer beyond Na^+/K^+, extending its use to other challenging mixed salt system. Finally, we will evaluate the practical application potential and economic viability of this technology by demonstrating sustainable one-step high-purity NaCl production from real seawater without pre- or post-treatment. Our goal is to present a viable and scalable solution that can significantly improve the purity of extracted salts and contribute to large-scale sustainable resource extraction.

Objective 3: Pioneering selective crystallization strategies through the difference in dissolution

A limited understanding of fundamental mechanisms currently hinders the widespread application of selective crystallization. While salt dissolution is a common phenomenon in interfacial evaporation crystallization, the significant differences in dissolution rates among various salts have rarely been explored for selective crystallization. Our primary objective is to introduce, develop, and validate a novel dissolution-driven selective crystallization strategy for the direct

production of high-purity salts across various challenging mixed salt systems. Recognizing that mixed salt solids are commonly encountered in current industrial production, we aim to use this strategy to directly extract high-purity salts from these solids through a single-step dissolution process. Finally, we'll quantify the technology's practical potential by extracting high-purity KCl from fly ash leachate in outdoor tests, assessing its performance and scalability for real-world applications. Ultimately, this thesis seeks to uncover and harness the untapped potential of salt dissolution as a transformative and sustainable pathway for efficient, high-purity salt production.

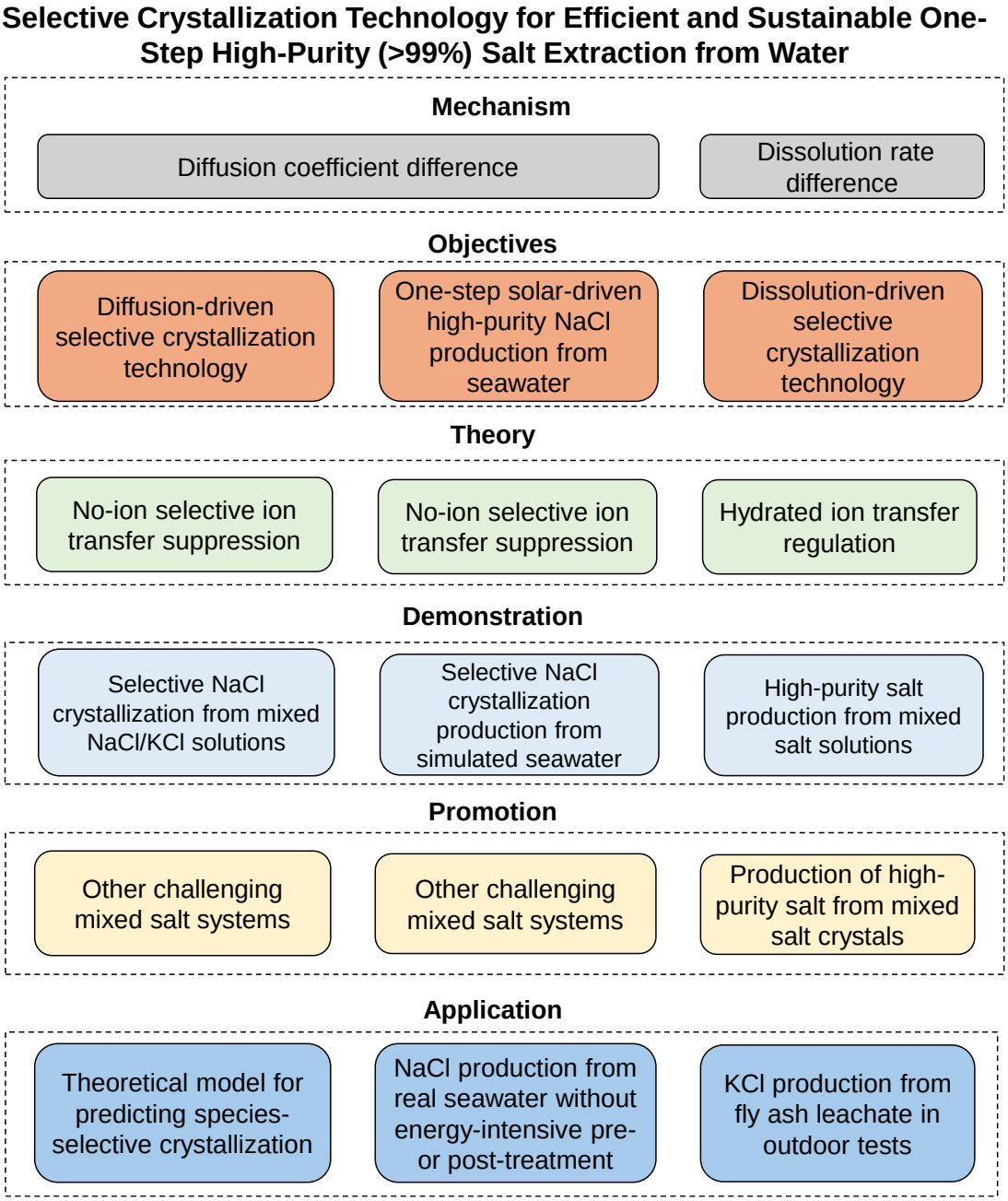

Figure 1.1 The block diagram that illustrates the overall framework and the interconnection of different components of this thesis.

This comprehensive research not only advances the fundamental scientific understanding of selective crystallization technologies but also delivers tangible, sustainable solutions for critical resource extraction. By successfully achieving

our objectives, we anticipate paving the way for more efficient and environmentally friendly technologies within the vital domains of resource extraction and water management, thereby contributing significantly to global sustainability efforts.

1.4 Thesis organization

This thesis systematically explores the development of selective high-purity (>99%) salt crystallization technology, organized into six distinct chapters. This structure ensures a comprehensive exploration from foundational concepts to experimental results and future implications.

Chapter 1: Introduction

This introductory chapter establishes the context for the thesis by outlining the critical challenges in salt resource extraction and highlighting the urgent need for advanced separation technologies. It then defines the research aims and objectives, and presents the primary strategies adopted throughout the thesis.

Chapter 2: Literature review on salt separation technologies

This chapter provides a comprehensive review of salt separation technologies. We begin by summarizing conventional methods, detailing their underlying principles, inherent advantages, limitations, and typical application scenarios. Given their ultimate reliance on evaporative crystallization to obtain high-purity solid salt products, we subsequently focus on evaporative

crystallization techniques for salt separation. These are categorized into bulk and interfacial evaporative crystallization, each discussed in terms of working mechanisms, strengths and weaknesses, practical applications, and current technical challenges. Finally, in light of recent breakthroughs in achieving high-purity salt extraction from complex aqueous systems, we present an in-depth review of interfacial evaporative selective crystallization, highlighting emerging principles and innovations that shape and inspire our research direction.

Chapter 3: Diffusion-driven selective crystallization for high-purity salt production

This chapter introduces a novel strategy for high-purity salt extraction. By suppressing non-ion-selective processes during interfacial evaporation, we successfully utilize a designed porous membrane that leverages differences in ion diffusion to achieve selective crystallization from various mixed salt systems. Meanwhile, a theoretical simulation framework for this novel selective crystallization method has been established. This framework accurately predicts the boundary conditions for species-selective crystallization, showing high consistency with experimental data and laying the foundation for future practical applications.

Chapter 4: Sustainable one-step high-purity NaCl production from seawater via solar interfacial evaporation and crystallization

This chapter details the development of a highly efficient solar crystallizer

for sustainable one-step high-purity NaCl production from seawater. Building upon the separation mechanisms established in Chapter 1, we designed a novel solar crystallizer capable of mitigating non-ion-selective processes. This enables the difference in Na^+/K^+ diffusion to drive selective high-purity NaCl crystallization from seawater under solar radiation. Its universality was further demonstrated through high-purity salt production from other mixed salt systems. Finally, its practical potential was confirmed by the direct production of high-purity NaCl from real seawater under regular solar radiation, notably without any pre- or post-treatment.

Chapter 5: Dissolution-driven selective crystallization for high-purity salt production

This chapter introduces an innovative selective mechanism that leverages the differences in salt dissolution. Our strategy centers on precisely regulating hydrated ion transfer from crystal surfaces to the source water, enabling the difference in salt dissolution rate to selectively retain targeted salt crystals while promoting the dissolution of unwanted salts into the source solution. High-purity salt production was achieved from various mixed salt systems. Furthermore, obtaining high-purity solid salts from mixed salt through selective dissolution process demonstrated the strategy's immense potential for integration with existing industries. Practical application was validated by outdoor high-purity KCl production from fly ash leachate.

Chapter 6: Conclusion and future outlook

This final chapter synthesizes the key findings and contributions of this thesis. It provides a comprehensive summary of the research conclusions and discusses their broader significance and implications for sustainable resource extraction and industrial applications. The chapter also outlines recommendations and potential avenues for future work, identifying promising directions for further research and development.

Reference

1 Epsztein, R., DuChanois, R. M., Ritt, C. L., Noy, A. & Elimelech, M. Towards single-species selectivity of membranes with subnanometre pores. *Nat. Nanotechnol.* **15**, 426–436 (2020).

2 Qiao, M. Selective separation of similar-sized solutes. *Nat. Chem. Eng.* **2**, 235–235 (2025).

3 Long, L. *et al.* Assessment of permeance and selectivity of thin-film composite polyamide membranes for diverse applications. *Nat. Water* (2025).

4 Yao, A., Benson, S. M. & Chueh, W. C. Critically assessing sodium-ion technology roadmaps and scenarios for techno-economic competitiveness against lithium-ion batteries. *Nat. Energy* (2025).

5 Yang, S., Wang, Y., Pan, H., He, P. & Zhou, H. Lithium extraction from low-quality brines. *Nature* **636**, 309–321 (2024).

6 Zhang, G. *et al.* Spontaneous lithium extraction and enrichment from brine with net energy output driven by counter-ion gradients. *Nat. Water* **2**, 1091–1101 (2024).

7 Xin, W. *et al.* Biomimetic KcsA channels with ultra-selective K^+ transport for monovalent ion sieving. *Nat. Commun.* **13**, 1701 (2022).

8 Thompson, A. N. *et al.* Mechanism of potassium-channel selectivity revealed by Na^+ and Li^+ binding sites within the KcsA pore. *Nat. Struct. Mol. Biol.* **16**, 1317–1324 (2009).

9 Xue, M. *et al.* Integrated biosensor platform based on graphene transistor arrays for real-time high-accuracy ion sensing. *Nat. Commun.* **13**, 5064 (2022).

10 Yang, S., Zhang, F., Ding, H., He, P. & Zhou, H. Lithium Metal Extraction from Seawater. *Joule* **2**, 1648–1651 (2018).

11 Brownlie, W. J. *et al.* Global food security threatened by potassium

neglect. *Nat. Food* **5**, 111–115 (2024).

12 Vera, M. L., Torres, W. R., Galli, C. I., Chagnes, A. & Flexer, V. Environmental impact of direct lithium extraction from brines. *Nat. Rev. Earth Environ.* **4**, 149–165 (2023).

13 Ekrami, J., Nemati Mansour, S., Mosaferi, M. & yamini, Y. Environmental impact assessment of salt harvesting from the salt lakes. *J. Environ. Health Sci. Eng* **19**, 365–377 (2021).

14 Zhang, C. *et al.* Designing a next generation solar crystallizer for real seawater brine treatment with zero liquid discharge. *Nat. Commun.* **12**, 998 (2021).

15 Fareza, A. R. *et al.* Cell Engineering Can Mitigate Cathode Scaling during Water Electrolysis in the Presence of Mg^{2+}. *ACS Electrochem.* **1**, 763–773 (2025).

16 Huang, Z. *et al.* Highly efficient potassium fertilizer production by using a gemini surfactant. *Green Chem.* **21**, 1406–1411 (2019).

17 Chao, X., Zhang, T.-a., Lyu, G., Liang, Z. & Chen, Y. Sustainable application of sodium removal from red mud: Cleaner production of silicon-potassium compound fertilizer. *J. Clean Prod.* **352** (2022).

18 DuChanois, R. M. *et al.* Prospects of metal recovery from wastewater and brine. *Nat. Water* **1**, 37–46 (2023).

19 Zhang, W., Oswal, H., Renew, J., Ellison, K. & Huang, C.-H. Removal of heavy metals by aged zero-valent iron from flue-gas-desulfurization brine under high salt and temperature conditions. *J. Hazard. Mater.* **373**, 572–579 (2019).

20 Qasem, N. A. A., Mohammed, R. H. & Lawal, D. U. Removal of heavy metal ions from wastewater: a comprehensive and critical review. *NPJ Clean Water.* **4**, 36 (2021).

21 Mitra, S. *et al.* Impact of heavy metals on the environment and human

health: Novel therapeutic insights to counter the toxicity. *Journal of King Saud University - Science* **34**, 101865 (2022).

22 Hama Aziz, K. H. *et al.* Heavy metal pollution in the aquatic environment: efficient and low-cost removal approaches to eliminate their toxicity: a review. *RSC Adv* **13**, 17595 – 17610 (2023).

23 Long, P. *et al.* Lithium enrichment in the Qarhan Salt Lake (China) was a long-term process driven by interglacial-glacial cycles. *Commun. Earth Environ.* **6**, 307 (2025).

24 Ye, T. *et al.* Artificial sodium-selective ionic device based on crown-ether crystals with subnanometer pores. *Nat Commun* **12**, 5231 (2021).

25 Yang, Y. *et al.* Atomistic insights into the K^+/Na^+ separation across amino modified graphene nanopore: The assisting role of Cl^-. *J. Mol. Liq.* **415**, 126371 (2024).

26 Fan, F. *et al.* A Bioinspired Membrane with Ultrahigh Li^+/Na^+ and Li^+/K^+ Separations Enables Direct Lithium Extraction from Brine. *Adv. Sci.* **11**, 2402898 (2024).

27 Cao, L. *et al.* Switchable Na^+ and K^+ selectivity in an amino acid functionalized 2D covalent organic framework membrane. *Nat. Commun.* **13**, 7894 (2022).

28 Sharkh, B. A. *et al.* Seawater desalination concentrate—a new frontier for sustainable mining of valuable minerals. *NPJ Clean Water.* **5** (2022).

29 Hussain, R. R. Groundbreaking Electrochemical Computation of Dispersed Individual Activation Energies and Development of Activation Energy Model for Chloride Induced Corrosion of RC Structures under Ambient Temperature. *Int. J. Electrochem. Sci.* **7**, 3656 – 3671 (2012).

30 Xia, S. *et al.* Effects of Temperature on Corrosion Behavior of Reinforcements in Simulated Sea-Sand Concrete Pore Solution. *Buildings* **12**, 407 (2022).

31 Elimelech, M. & Phillip, W. A. The Future of Seawater Desalination: Energy, Technology, and the Environment. *Science* **333**, 712–717 (2011).

32 Wang, R., Alghanayem, R. & Lin, S. Multipass Nanofiltration for Lithium Separation with High Selectivity and Recovery. *Environ. Sci. Technol.* (2023).

33 Bi, Q. & Xu, S. Separation of magnesium and lithium from brine with high Mg^{2+}/Li^{+} ratio by a two-stage nanofiltration process. *Desalin. Water Treat.* **129**, 94–100 (2018).

34 Rolf, J. *et al.* Inorganic Scaling in Membrane Desalination: Models, Mechanisms, and Characterization Methods. *Environ. Sci. Technol.* **56**, 7484–7511 (2022).

35 Zheng, L. *et al.* Mixed scaling patterns and mechanisms of high-pressure nanofiltration in hypersaline wastewater desalination. *Water Res.* **250**, 121023 (2024).

36 Vogel, D. *et al.* Effects of fouling and scaling on the retention of trace organic contaminants by a nanofiltration membrane: The role of cake-enhanced concentration polarisation. *Sep. Purif. Technol.* **73**, 256–263 (2010).

37 Li, Y. *et al.* Fouling behavior of nanofiltration membrane during the refining treatment of morphlines-dominant reverse osmosis concentrate. *J. Environ. Manage.* **364**, 121443 (2024).

38 Turek, M. *et al.* Improving the Performance of a Salt Production Plant by Using Nanofiltration as a Pretreatment. *Membranes* **12**, 1191 (2022).

39 Dahmardeh, H., Akhlaghi Amiri, H. A. & Nowee, S. M. Evaluation of mechanical vapor recompression crystallization process for treatment of high salinity wastewater. *Chem. Eng. Process.: Process Intensif.* **145**, 107682 (2019).

40 Shamet, O. & Antar, M. Mechanical vapor compression desalination technology – A review. *Renew. Sust. Energ. Rev.* **187**, 113757 (2023).

41 Tucker, C. I., Bartholomew, T. V., Dudchenko, A. V. & Mauter, M. S.

Component innovations for lower cost mechanical vapor compression. *Water Res.* **260**, 121950 (2024).

42 Yong, M. *et al.* Nanofiltration Membranes for Efficient Lithium Extraction from Salt-Lake Brine: A Critical Review. *ACS Environ. Au* **5**, 12–34 (2025).

43 Zhang, L. *et al.* A review of the nanofiltration membrane for magnesium and lithium separation from salt-lake brine. *Sep. Purif. Technol.* **354**, 129169 (2025).

2 Literature review

2.1 Conventional separation methods and their challenges

Conventional salt separation methods exploit differences in physicochemical properties among salts, such as chemical precipitation based on solubility products, membrane separation based on salt ion size and charge, and adsorption guided by specific ion-material interactions. While effective in specific scenarios, these methods still face significant limitations in efficiency, cost, selectivity, and sustainability. This drives ongoing research to develop innovative separation methods for more efficient and environmentally friendly salt separation.

2.1.1 Chemical precipitation

Salt separation by chemical precipitation is based on the principle of inducing targeted salts to form salt with low solubility products (Ksp) through the addition of specific reagents. This method allows selective precipitation of desired components while leaving others in solution, which is particularly effective for selectively separating salts when target ion concentrations are relatively high. For example, in industrial-scale lithium extraction from brine via carbonate precipitation, it is generally necessary that the lithium chloride concentration be above approximately 15 $g \cdot L^{-1}$ to ensure efficient precipitation and high recovery rates[1-3]. Lower concentrations would significantly reduce the precipitation efficiency and selectivity[2]. This method is relatively simple and

scalable, requiring minimal infrastructure, making it suitable for large-scale industrial operations[4,5].

However, this method faces significant challenges in practical applications, including a high consumption of chemical reagents, substantial sludge generation, and limited separation efficiency at low salt concentrations. For example, KR-slag and $Ca(OH)_2$ with carbonation have been applied for the separation of Cd^{2+} and Pb^{2+} from waste brine via chemical precipitation. However, the process generates sludge with a volume of up to 103 $mL \cdot L^{-1}$, significantly complicating its subsequent treatment. Moreover, at low salt concentrations, the separation efficiency drops sharply due to incomplete precipitation. For example, using various phosphate precipitants, a lithium recovery rate of over 80% can be achieved when the initial lithium concentration is 1000 $mg \cdot L^{-1}$ or higher. In contrast, when the concentration falls below 250 $mg \cdot L^{-1}$, lithium precipitation becomes nearly negligible[6]. More importantly, chemical precipitation shows clear limitations in extracting salts with a relatively large Ksp. For instance, salts like KCl and NaCl, with Ksp values of 21.7 and 37.7 at 25^{o}C, respectively, making selective precipitation challenging and inefficient.

2.1.2 Solvent extraction

Solvent extraction, also known as liquid-liquid extraction, is a separation method that relies on the differential solubility of salts in two immiscible liquids,

typically an aqueous phase and an organic phase[7,8]. This method is widely used for separating and concentrating specific salts at lower concentrations due to its high selectivity and efficiency. For instance, a solvent extraction method using kerosene as the organic phase has been used to extract Li^+ from seawater. In this process, 65 % of lithium ion were effectively extracted from seawater by the chelating agent thenoyltrifluoroacetone–trioctylphosphine oxide (TTA–TOPO) dissolved in kerosen[9].

However, several limitations hinder its widespread adoption. Conventional solvent extraction processes often employ organic solvents like toluene, chloroform, or carbon tetrachloride. These solvents are inherently flammable, volatile, or toxic, posing significant environmental and safety risks during handling and disposal[8,10,11]. Furthermore, solvents can remain in the crystallized salt, which reduces product purity and necessitates additional purification steps (e.g., vacuum distillation or activated carbon filtration) to meet industrial-grade specifications[12]. Another fundamental challenge of this method lies in separating salts with similar chemical properties, such as NaCl and KCl[13]. For example, when separating K^+ from Na^+ in an alkaline solution using solvent extraction with 4-tert-butyl-2-(α-methylbenzyl)phenol, the separation factor was less than 5[14].

2.1.3 Adsorption

Adsorption is a surface-based separation process in which salt ions

(adsorbates) from a liquid solution accumulate on the surface of a solid material (adsorbent) through intermolecular forces[15,16]. This method demonstrates great separation efficiency in complex multicomponent systems and low-concentration salt enrichment scenarios. For example, adsorption is an effective method for the recovery of Li^+ from seawater (0.17 $mg \cdot L^{-1}$)[17]. When lithium manganese oxide (LMO) powder is used as adsorbent and loaded into a multi-stage column system, it achieved a maximum adsorption capacity of 23.9 $mg \cdot g^{-1}$ from Li-spiked seawater[18,19]. Meanwhile, adsorption processes can be designed for continuous operation and scaled up for industrial applications, making them suitable for large-volume salt separation needs. A prime example is the breakthrough in lithium extraction from Qinghai salt lakes in China, where adsorption-based technologies have enabled an annual production capacity of 200,000 metric tons of battery-grade lithium carbonate.

Despite its advantages, adsorption for salt separation also has limitations and challenges. After reaching saturation, adsorbents lose their salt extraction capability and require regeneration to restore their effectiveness. Generally, adsorbent regeneration can be achieved through thermal regeneration or by using desorption reagents, such as inorganic acids (e.g., HCl, HNO_3) or organic acids (e.g., acetic acid). This process increases energy consumption and leads to chemical pollution. Meanwhile, although desorption reagents offer good regeneration efficiency, they can destroy adsorption sites, thereby reducing the

adsorbent's capacity[20-22]. Furthermore, separating salts with similar physicochemical properties, such as NaCl and KCl, also remains challenging. For example, manganese dioxide ion-sieves only achieve the selectivity coefficients of Na^+ for K^+ of 1.08[23].

2.1.4 Membrane filtration

Membrane-based separation is a versatile method that utilizes selective membranes to separate salts from aqueous solutions based on differences in salt ion charge and size[24]. For example, NF can effectively separate Li^+ and Mg^{2+} from salt lakes by leveraging differences in both ionic size and charge, enabling efficient lithium extraction[25,26]. As an emerging and increasingly important technology in salt separation, membrane-based processes offer several advantages, including modular design, scalability, and the ability to operate continuously without the need for chemical additives. For example, theoretical simulation showed that a four-pass NF process with brine recirculation can simultaneously achieve an ultrahigh Li/Mg selectivity of over 4500 and a Li recovery of over 95%[27].

Despite their advantages, membrane separation technologies still face significant challenges in practical applications, particularly related to membrane fouling, energy consumption, and limited ion selectivity. In the context of lithium extraction from brine using NF, coexisting salts such as $MgSO_4$ can precipitate or deposit on the membrane surface[28], leading to pore blockage and a marked

decline in both permeability and separation efficiency. Beyond inorganic fouling, NF membranes are also susceptible to the accumulation and adsorption of organic macromolecules and colloidal substances, such as carboxylic acids and aromatic compounds on the membrane surface[29,30]. Similar to inorganic fouling, this also results in pore clogging and degradation of membrane performance over time.

Meanwhile, membrane separation processes are also significantly influenced by salt concentration. Firstly, high salinity levels generate substantial osmotic pressure, necessitating elevated operating pressures for membrane filtration to overcome this resistance and maintain adequate flux, which consequently increases energy consumption. In addition, elevated salt concentrations induce charge screening effects that weaken charge exclusion, thereby diminishing the membrane's ion selectivity and overall separation efficiency[27,31]. Consistent with previously discussed separation methodologies, a significant limitation arises when separating salt ions with similar physicochemical properties, such as Na^+ and K^+. For example, UiO-66-COOH metal-organic frameworks with ~0.6 nm-sized windows and ~0.8-1.1 nm-sized cavities demonstrated a high K^+/Mg^{2+} selectivity of ~103 and a Na^+/Mg^{2+} selectivity of ~102. However, the K^+/Na^+ selectivity was less than 2[32].

2.2 Evaporation Crystallization Methods for High-Purity Salt Separation

Traditional separation methods, while effective under specific conditions,

often rely on evaporative crystallization as the final step for producing solid salt products. This dependence has positioned evaporative crystallization as a cornerstone in the extraction of salt resources from aqueous systems. Depending on operational conditions, it is typically categorized into bulk evaporation crystallization and interfacial evaporation crystallization. To streamline the extraction of high-purity solid salts and achieve one-step production, current research increasingly focuses on enhancing crystallization selectivity through interface engineering, kinetic control, and innovative system designs.

2.2.1 Bulk evaporation crystallization technology

Bulk evaporation crystallization is a widely employed salt separation method that relies on thermal energy[33-35]. The process involves heating the solution to evaporate the solvent, typically water, thereby increasing the concentration of dissolved salts until supersaturation is achieved. At this point, spontaneous nucleation occurs, followed by crystal growth, leading to the formation of solid salt products. Owing to its robust capacity for handling high salinity, this method is particularly effective for recovering salts from concentrated brines. For instance, as an effective bulk evaporation and crystallization technology, single/multiple-effect evaporation (SEE/MEE) combined with single/multi-stage mechanical vapor recompression (SVR-MVR) systems (Figure 2.1) were frequently applied for salt production from brine with

high salinity (70 g·kg^{-1})[36]

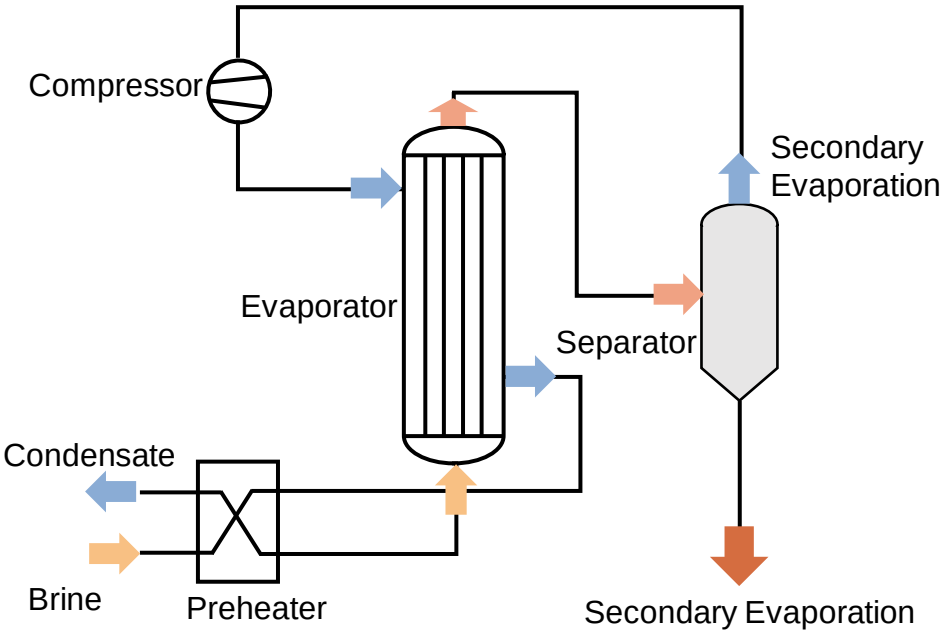

Figure 2.1 Schematic of MVR system

When applied for high-purity salt extraction, bulk evaporative crystallization faces several significant drawbacks. Primarily, different dissolved salts in the solution tend to crystallize simultaneously once their respective solubility limits are exceeded, which directly results in lower purity of the extracted salts. For instance, in an MVR system, evaporation typically occurs very close to the salt saturation point (300,000 ppm or 300 g·kg^{-1})[36], leading to the simultaneous crystallization of most dissolved salts and thus the production of mixed salt products.

Beyond its limited selectivity, the crystallizer's vigorous boiling and chaotic fluid motion during evaporation render the crystallization process difficult to

control for salt separation. For instance, in the MVR system, the circulating solution's mass flow rate can reach as high as 50 $m^3 \cdot h^{-1}$, which significantly complicates the control of the crystallization process[37]. This technology's application is also limited by high energy consumption, particularly when treating streams requiring extensive water removal[38]. It is estimated that the energy consumption of the bulk evaporation and crystallization by MVR is 53-66 $kW \cdot hm^{-3}$. Meanwhile, the aggressive operating environment, characterized by high salinity and elevated temperatures, accelerates the corrosion of metallic equipment. This necessitates the use of expensive corrosion-resistant materials for the crystallizer[39], which significantly increases both capital expenditure and maintenance costs.

2.2.2 Interfacial evaporation crystallization technology

Interfacial evaporation crystallization is an emerging technology that fundamentally differs from conventional bulk thermal evaporation. This method confines heat generation and evaporation specifically to the air-water interface [38,40,41]. This is typically achieved using a floating crystallizer, which converts energy sources—such as sunlight or electricity—into localized heating concentrated at the crystallizer surface. This localized heat then drives rapid water evaporation within the crystallizer, leading to salt crystallization on the evaporation surface (Figure 2.2). By confining heat to the interface rather than the bulk solution, this design significantly reduces energy losses, avoids

unnecessary heating of the entire liquid volume, and enables more efficient and targeted crystallization.

Figure 2.2 Schematic illustration of interfacial evaporation crystallization technology

Meanwhile, interfacial evaporation crystallizers require only three layers: a heating generation layer, a water transport layer, and an insulating substrate. This simplifies design, reduces equipment complexity, and lowers capital investment, making them suitable for decentralized or small-scale applications. For example, a designed 3D-cup solar crystallizer successfully achieved zero liquid discharge (ZLD) from real seawater brine with a total salinity of 21.6 wt%[42]. Compared to commercial ZLD systems, which range in cost from $250000 to over $2 million for capacities of 5-100 m^3 per day, this solar crystallizer provides

a low-cost alternative for small to medium-volume brine treatment (10-15 m^3)[42].

However, interfacial evaporation crystallization technology also faces significant challenges in high-purity salt production. Similar to bulk evaporation, interfacial evaporation crystallization primarily separates water from solutes and is generally unable to achieve selective salt crystallization[40,42,43]. For example, although the 3D-cup solar crystallizer achieved stable ZLD, both $MgSO_4$ and NaCl were present in the crystallized solid, leading to the generation of waste solids[42].

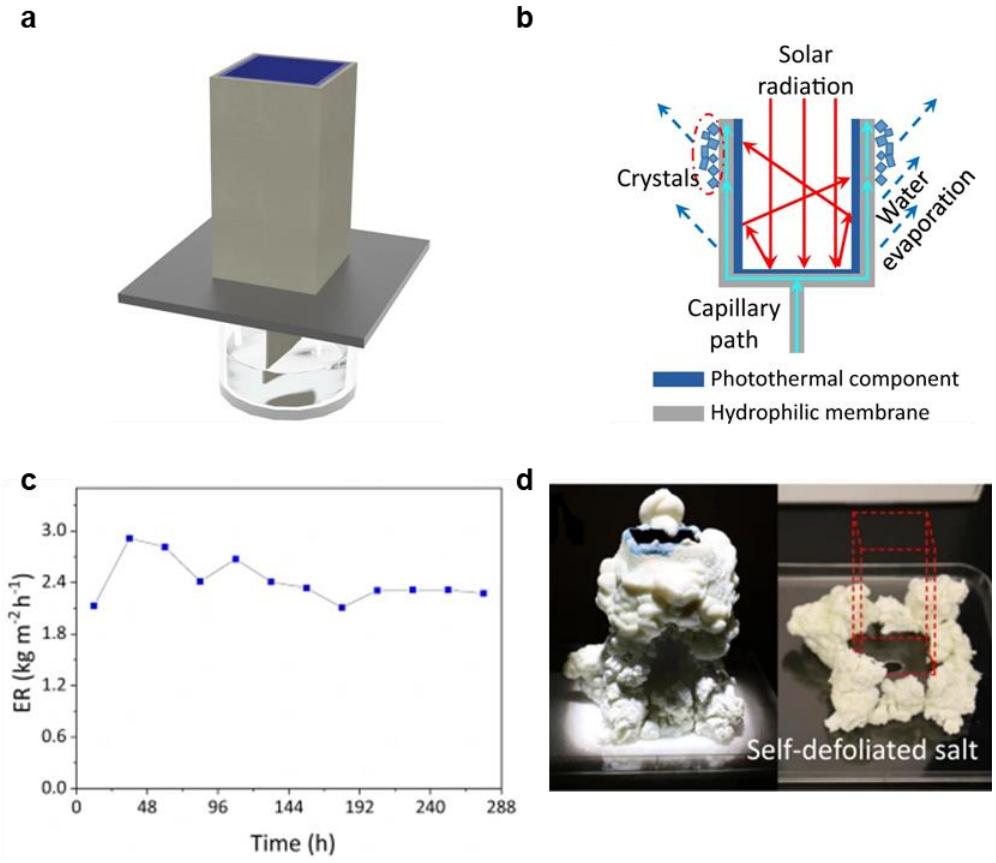

Figure 2.3 Designed 3D-cup solar evaporation crystallizer to achieve ZLD of real seawater brine. (a) Schematic illustration of the solar crystallizer. (b)

Schematic of cross-sectional view of the solar crystallizer. (c) Evaporation rate of the solar crystallizer during evaporation of real seawater brine (each point on the curve was the average evaporation rate of 24 h). (d) Photos of the solar crystallizer and self-defoliated salt after 48-h evaporation (the red dotted frame represents the position of removed solar crystallizer)[42].

2.2.3 Interfacial evaporation selective crystallization technology

Interfacial evaporation selective crystallization technology is an advanced salt extraction method built upon the principles of interfacial evaporation. It's specifically aimed at selectively extracting target solutes (mineral resources) from complex solutions[44]. This technology not only offers high energy efficiency and a simple device structure, but more importantly, it enables direct high-purity salt production. Existing selective crystallization mechanisms can generally be categorized into two types: one involves coupling traditional salt separation technologies, such as nanofiltration[45,46], with interfacial evaporation, while the other leverages the intrinsic physicochemical differences of mixed salts, such as solubility[47]. For the first selective crystallization mechanism, a membrane-based solar evaporator is employed. This device consists of an upper photothermal layer for water evaporation, a hydrophilic porous membrane in the middle to generate capillary pressure for water transport, and an ultrathin nanofiltration membrane at the bottom to achieve efficient LiCl/$MgCl_2$

separation[46]. This system enables the extraction of LiCl crystals with 94% purity from simulated salt lakes[46].

As for the second type, based on the different solubility of LiCl and NaCl, a twisted and slender 3D porous natural cellulose fiber structure was proposed to achieve spatially separated LiCl and NaCl crystallization[47]. This process can selectively concentrate lithium by over 39-fold from continental brine and 675-fold from seawater, respectively. Similarly, a wood-derived crystallizer was designed to separate NaCl and Na_2SO_4 in industrial brine by exploiting the charge differences of the salt anions. This process achieved 99.34% Na_2SO_4 crystal extraction from mixed Na_2SO_4/NaCl with a mass ratio of 4:1[48].

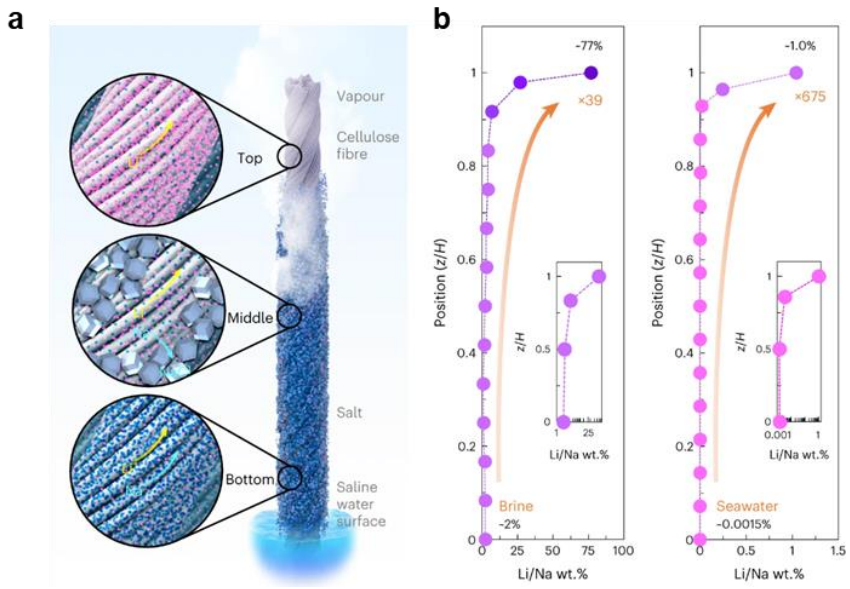

Figure 2.4 Interfacial evaporation selective crystallization of LiCl from mixed LiCl/NaCl solution based on solubility difference. (a) Schematic of the 3D spatial crystallization process. At the bottom position (Bottom), mixed LiCl and NaCl are carried upward via capillary flow. At the middle position (Middle), NaCl

saturates and crystallizes due to a lower solubility, while LiCl continue to move upward with the water flow. At the top position (Top), LiCl crystallize when the saline water completely evaporates. (b-c) The Li/Na ratio increased along the 3D fiber crystallizer, with LiCl concentrated when using brine as bulk solution (b) and when using seawater as bulk solution (c)[47].

Despite significant breakthroughs, this technology faces challenges due to limited separation mechanisms and uncertainties in practical application. Existing methods primarily exploit differences in solubility and ion charge. Consequently, for salts with similar solubilities and identical ion charges, such as NaCl and KCl, these approaches exhibit clear limitations in separation performance. Furthermore, current selective crystallization techniques remain at laboratory scale, creating a considerable gap from real-world scenarios. For instance, artificial salt-lake brines typically composed of simple binary mixtures such as $MgCl_2$ and LiCl are often used to evaluate selective LiCl crystallization performance, but they poorly represent the complexity of natural saline environments that contain a broader range of salts[46,49], such as NaCl and KCl. This disparity renders laboratory results less representative of actual conditions, increasing practical application uncertainty.

Reference

1 Wang, R., Alghanayem, R. & Lin, S. Multipass Nanofiltration for Lithium Separation with High Selectivity and Recovery. *Environ. Sci. Technol.* (2023).

2 Khalil, A., Mohammed, S., Hashaikeh, R. & Hilal, N. Lithium recovery from brine: Recent developments and challenges. *Desalination* **528**, 115611 (2022).

3 Garcia, L. V., Ho, Y.-C., Myo Thant, M. M., Han, D. S. & Lim, J. W. Lithium in a Sustainable Circular Economy: A Comprehensive Review. *Processes* **11**, 418 (2023).

4 Choe, G. *et al.* Re-evaluation of battery-grade lithium purity toward sustainable batteries. *Nat. Commun.* **15**, 1185 (2024).

5 Awais Ashraf, M. *et al.* Lithium extraction from high magnesium salt lake brine with an integrated membrane technology. *Sep. Purif. Technol.* **302** (2022).

6 Shin, J. *et al.* Preparation of lithium carbonate from waste lithium solution through precipitation and wet conversion methods. *Hydrometallurgy* **210**, 105863 (2022).

7 Gulliani, S., Volpe, M., Messineo, A. & Volpe, R. Recovery of metals and valuable chemicals from waste electric and electronic materials: a critical review of existing technologies. *RSC Sustain.* **1**, 1085–1108 (2023).

8 Li, Z., Dewulf, B. & Binnemans, K. Nonaqueous Solvent Extraction for Enhanced Metal Separations: Concept, Systems, and Mechanisms. *Ind. Eng. Chem. Res.* **60**, 17285–17302 (2021).

9 Harvianto, G. R., Kim, S.-H. & Ju, C.-S. Solvent extraction and stripping of lithium ion from aqueous solution and its application to seawater. *Rare Metals* **35**, 948–953 (2016).

10 Bezdomnikov, A. A. *et al.* Specific features of lithium solvent extraction from perchlorate media with benzo-15-crown-5. *Polyhedron* **244**, 116612

(2023).

11 Bai, R., Wang, J., Wang, D., Zhang, Y. & Cui, J. Selective separation of lithium from the high magnesium brine by the extraction system containing phosphate-based ionic liquids. *Sep. Purif. Technol.* **274**, 119051 (2021).

12 Kim, H. H. & Chang, Y. K. Removal of potassium chloride from ion-exchanged solution containing potassium clavulanate by diafiltration with nanomembrane and its modeling. *J. Membr. Sci.* **342**, 173–178 (2009).

13 Docker, A. *et al.* Selective Potassium Chloride Recognition, Sensing, Extraction, and Transport Using a Chalcogen-Bonding Heteroditopic Receptor. *J. Am. Chem. Soc.* **144**, 14778–14789 (2022).

14 Xing, P., Wang, C.-y., Chen, Y.-q. & Ma, B.-z. Separation of potassium from sodium in alkaline solution by solvent extraction with 4-tert-butyl-2-(α-methylbenzyl) phenol. *J. Cent. South Univ.* **28**, 2003–2009 (2021).

15 Swain, B. Recovery and recycling of lithium: A review. *Sep. Purif. Technol.* **172**, 388–403 (2017).

16 Lim, Y. J., Goh, K., Goto, A., Zhao, Y. & Wang, R. Uranium and lithium extraction from seawater: challenges and opportunities for a sustainable energy future. *J. Mater. Chem. A* **11**, 22551–22589 (2023).

17 Liu, C. *et al.* Lithium Extraction from Seawater through Pulsed Electrochemical Intercalation. *Joule* **4**, 1459–1469 (2020).

18 Shin, J. *et al.* Recovery of Li from seawater using $Li_{1.33}Mn_{1.67}O_4$ immobilized multi-stage column system. *Desalination* **583**, 117656 (2024).

19 Coterillo, R. *et al.* Selective extraction of lithium from seawater desalination concentrates: Study of thermodynamic and equilibrium properties using Density Functional Theory (DFT). *Desalination* **532**, 115704 (2022).

20 Huang, Y. & Wang, R. Green recovery of lithium from water by a smart imprinted adsorbent with photo-controlled and selective properties. *Chem. Eng. J.* **378**, 122084 (2019).

21 Sharma, M., Vyas, R. K. & Singh, K. A review on reactive adsorption for potential environmental applications. *Adsorption* **19**, 161 – 188 (2013).

22 Vera, M. L., Torres, W. R., Galli, C. I., Chagnes, A. & Flexer, V. Environmental impact of direct lithium extraction from brines. *Nat. Rev. Earth Environ.* **4**, 149 – 165 (2023).

23 Liu, D.-F., Sun, S.-Y. & Yu, J.-G. Electrochemical and adsorption behaviour of Li^+, Na^+, K^+, Ca^{2+}, and Mg^{2+} in $LiMn_2O_4$/ λ -MnO_2 structures. *Can. J. Chem.* **97**, 1589 – 1595 (2019).

24 Epsztein, R., DuChanois, R. M., Ritt, C. L., Noy, A. & Elimelech, M. Towards single-species selectivity of membranes with subnanometre pores. *Nat. Nanotechnol.* **15**, 426 – 436 (2020).

25 Yang, Z. *et al.* Dual-skin layer nanofiltration membranes for highly selective Li+/Mg2+ separation. *J. Membr. Sci.* **620**, 118862 (2021).

26 Liu, X. *et al.* High-permeance Mg^{2+}/Li^+ separation nanofiltration membranes intensified by quadruple imidazolium salts. *J. Membr. Sci.* **667**, 121178 (2023).

27 Wang, R., Alghanayem, R. & Lin, S. Multipass Nanofiltration for Lithium Separation with High Selectivity and Recovery. *Environ. Sci. Technol.* **57**, 14464 – 14471 (2023).

28 Wang, X.-m. & Waite, T. D. Role of Gelling Soluble and Colloidal Microbial Products in Membrane Fouling. *Environ. Sci. Technol.* **43**, 9341 – 9347 (2009).

29 Li, Y., Zhao, Y. J., Wang, M. & Wang, H. Y. Enhanced anti-fouling and selective performance of GO-modified nanofiltration membranes for lithium extraction from salt lake brine. *Chem. Eng. J.* **499**, 156269 (2024).

30 Wang, J. *et al.* Enhanced gypsum scaling by organic fouling layer on nanofiltration membrane: Characteristics and mechanisms. *Water Res.* **91**, 203 – 213 (2016).

31 Li, S. *et al.* Nanofiltration Membranes with Salt-Responsive Ion Valves for Enhanced Separation Performance in Brackish Water Treatment: A Battle against the Limitation of Salt Concentration. *Environ. Sci. Technol.* **57**, 14452–14463 (2023).

32 Lu, J. *et al.* Efficient metal ion sieving in rectifying subnanochannels enabled by metal–organic frameworks. *Nat. Mater.* **19**, 767–774 (2020).

33 Zhang, X. *et al.* A renewable energy harvesting system using a mechanical vibration rectifier (MVR) for railroads. *Appl. Energy* **204**, 1535–1543 (2017).

34 Han, D., Yue, C., He, W., Liang, L. & Pu, W. Energy saving analysis for a solution evaporation system with high boiling point elevation based on self-heat recuperation theory. *Desalination* **355**, 197–203 (2015).

35 Liu, G., Yang, Q., Zhao, Y., Li, L. & Wang, L. Experimental research on MVR system for industrial wastewater treatment. *Desalin. Water Treat.* **147**, 99–105 (2019).

36 Dahmardeh, H., Akhlaghi Amiri, H. A. & Nowee, S. M. Evaluation of mechanical vapor recompression crystallization process for treatment of high salinity wastewater. *Chem. Eng. Process.: Process Intensif.* **145**, 107682 (2019).

37 Han, D., Chen, J., Zhou, T. & Si, Z. Experimental investigation of a batched mechanical vapor recompression evaporation system. *Appl. Therm. Eng.* **192**, 116940 (2021).

38 Tao, P. *et al.* Solar-driven interfacial evaporation. *Nat. Energy* **3**, 1031–1041 (2018).

39 Ouyang, M. *et al.* Investigating the corrosion behaviour of Alloy 34 in a simulated waste sulfuric acid recovery environment. *Constr. Build. Mater.* **472**, 140813 (2025).

40 Xia, Y. *et al.* Spatially isolating salt crystallisation from water

evaporation for continuous solar steam generation and salt harvesting. *Energy Environ. Sci.* **12**, 1840–1847 (2019).

41 Xu, K., Wang, C., Li, Z., Wu, S. & Wang, J. Salt Mitigation Strategies of Solar‐Driven Interfacial Desalination. *Adv. Funct. Mater.* **31** (2020).

42 Zhang, C. *et al.* Designing a next generation solar crystallizer for real seawater brine treatment with zero liquid discharge. *Nat. Commun.* **12**, 998 (2021).

43 Wang, Y. *et al.* Salt isolation from waste brine enabled by interfacial solar evaporation with zero liquid discharge. *J. Mater. Chem. A* **10**, 14470–14478 (2022).

44 Zheng, S., Oelckers, B., Khandelwal, A. & Ren, Z. J. Interfacial solar evaporation for sustainable brine mining. *Nat. Water* **3**, 135–137 (2025).

45 Song, Y. *et al.* Solar transpiration–powered lithium extraction and storage. *Science* **385**, 1444–1449 (2024).

46 Zhang, S. *et al.* Solar-driven membrane separation for direct lithium extraction from artificial salt-lake brine. *Nat. Commun.* **15**, 238 (2024).

47 Chen, X. *et al.* Spatially separated crystallization for selective lithium extraction from saline water. *Nat. Water* **1**, 808–817 (2023).

48 Zhang, W. *et al.* Solar-Driven Nanofluidic Ion Regulation for Fractional Salt Crystallization and Reutilization. *ACS Nano* **19**, 6320–6331 (2025).

49 Eskafi, A. F., De Finnda, C., Garcia, C. A. & Mi, B. Mineral Scaling in 3D Interfacial Solar Evaporators—A Challenge for Brine Treatment and Lithium Recovery. *Environ. Sci. Technol.* **59**, 892–901 (2025).

3 Diffusion-driven selective crystallization of high-purity salt through simple and sustainable one-step evaporation

Abstract

High-purity salt extraction from seawater, wastewater, and salt lakes is complex, energy-intensive, and environmentally unsustainable, primarily due to the need for multiple separation stages and the generation of hazardous byproducts. In this Chapter, we propose a diffusion-driven selective crystallization strategy for high-purity salt production directly from source water with mixed salts. The essence of the strategy is to purposefully suppress non-ion-selective transfer processes (e.g., convection) so to make the difference in ion diffusion drive targeted ion to selectively move to the crystallization surface. As a proof of concept, we designed a floating porous membrane designed with precise control over pore size, evaporation rate, and thickness. This enabled a simple but precise ion separation and one-step selective crystallization of high-purity salt (>99.10%) from such mixed source solutions as Na^+/K^+, Ba^{2+}/K^+ and Mg^{2+}/Li^+. To pave the way for future practical applications, this study further established a theoretical model that accurately predicts the boundary conditions necessary for species-selective crystallization via this strategy. This diffusion-driven selective crystallization strategy opens a new horizon for

precise ion separation and enriches the toolbox for high-purity salt production.

3.1 Introduction

Salt resources such as lithium, sodium, potassium, and magnesium are indispensable for modern technologies[1-5], including but not limited to resource extraction[2,3], chemical synthesis, energy storage[1,6-8], and water treatment[9-12]. These critical salts are widely distributed in aqueous environments, making their extraction from seawater, industrial wastewater, and salt lakes a subject of increasing attention[13,14]. However, the presence of these salts in aqueous systems, primarily as complex ionic mixtures, demands the development of highly efficient and selective ion separation technologies to recover and purify target products with minimal environmental impact. Over the past decades, conventional processes, such as precipitation[15], membrane filtration[4,16,17], and adsorption[18-20], have contributed significantly to ion separation, supporting the fast development of well-beings of human society. However, these methods still face key challenges, including limited separation efficiency, waste generation, and high energy consumption[13,21].

As the ultimate goal of ion separation is to produce high-purity salts from water[4,16,17], evaporation followed by immediately subsequent crystallization is frequently used as the last step in harvesting high-purity solid products during multi-step and complex ion separations, which typically are accompanied with high energy consumption and tedious product refinement. With ever-tightening

environmental regulations and a global commitment to carbon neutrality, there is now a heightened demand for sustainable ion separation with low energy consumption and minimal carbon footprint[22,23].

In recent years, substantial efforts have been devoted to integrating renewable energy-driven evaporation into conventional separation processes[24-26], but are met with limited success[13]. Therefore, a simple and sustainable one-step method for high-purity salt production is highly desired but remains elusive. In this Chapter, we propose a diffusion-driven selective crystallization strategy (DiSC) for direct high-purity salt crystallization from mixed source solutions (Figure 1a). The essence of the strategy is to purposefully suppress non-selective ion transfer processes (e.g., convection) so that the difference in ion diffusion coefficients could drive selective high-purity salt crystallization. Conceptually, a floating porous membrane evaporator that has precise control over its pore size, thickness, and evaporation rate to suppress its ion convection and match the evaporation-driven ion flow rate with ion diffusion rate would fulfill the requirements by DiSC and result in selective crystallization of the ions with lower diffusion coefficients.

As a proof of concept, DiSC was initially but successfully demonstrated by integrating sustainable wind and solar energy to drive the evaporation of a mixed NaCl/KCl source solution, which was chosen due to the significantly different ion diffusion coefficients of Na^+ (0.87×10^{-9} $m^2 \cdot s^{-1}$) and K^+ ($2.17 \times 10^{-}$

[9] $m^2 \cdot s^{-1}$). The pair was chosen also because they are quite similar in other physicochemical properties[4], making their separation difficult by conventional methods. This study also presented a theoretical model that precisely predicted the boundary conditions for no salt crystallization, selective crystallization, and mixed salt crystallization from mixed source solution. The modelling results helped the rational design and fabrication of the porous membrane evaporator, which achieved selective crystallization of NaCl on its surface with a purity over 99% from the mixed source solution at a NaCl/KCl mass ratio of 5:1. Building upon this initial success, we further developed a solar evaporation system capable of directly extracting NaCl crystals with a purity of 99.38% from real seawater without any pre- and post-treatment required. Selective crystallization was also demonstrated with Ba^{2+}/K^{+} and Mg^{2+}/Li^{+} mixed source solutions to produce high-purity salt (>99.10%). These findings enrich the fundamental separation theory. DiSC offers a sustainable solution for high-purity salt extraction which is particularly suitable as the last valorization step of many industrial separation processes, such as strategic mineral extraction from salt lakes and ocean, and resource recovery from industrial wastewater.

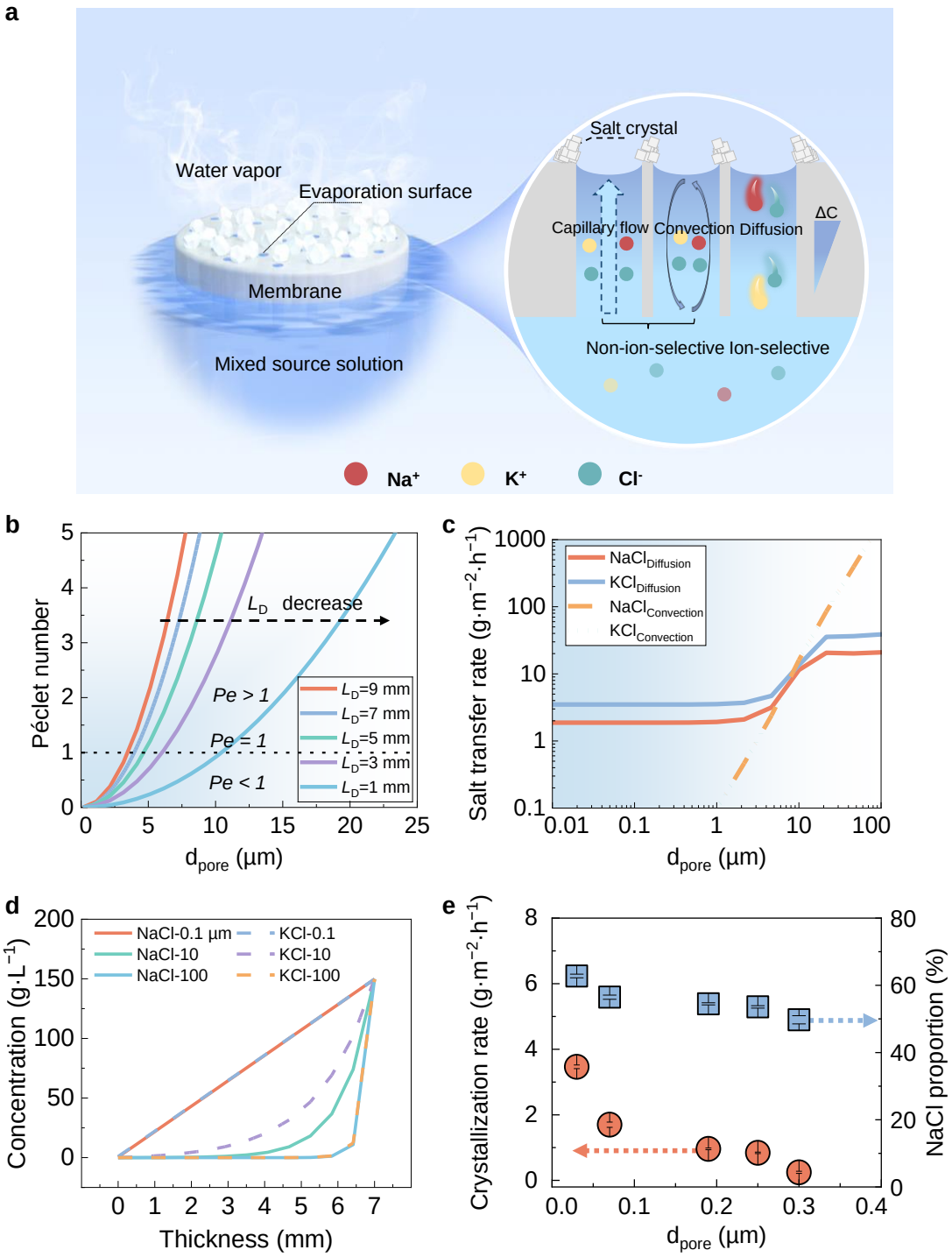

Figure 3.1 System design and convection suppression for diffusion-driven selective crystallization. (a) Schematic illustration of selective crystallization. (b) Calculated Péclet number (*Pe*) of the porous membrane with different pore sizes (d_{pore}) and diffusion length (L_D). (c) The effect of the pore size on the

convection and diffusion rates of NaCl and KCl through the porous membranes. The dashed line represents the convection rate of KCl, while the dash dot line represents the convection rate of NaCl. (d) COMSOL simulated concentration profiles of NaCl and KCl within the porous membrane with different pore sizes (both NaCl and KCl were maintained at a saturated surface concentration of 150 $g \cdot L^{-1}$). The thickness in the figure is measured from the bottom surface of the membrane. The solid and dashed lines represent the concentration of NaCl and KCl in the membrane, respectively. (e) The experimentally measured crystallization rate and the proportion of NaCl in the crystallized salts from the mixed NaCl/KCl solution with a mass ratio of 1:1 and a total salt concentration of 40 $g \cdot L^{-1}$ on the surface of the porous membrane at different pore sizes. The evaporation was driven by wind at 25^{o}C. (Error bars represent standard deviation from five measurements)

3.2 Results

3.2.1 System design for diffusion-driven selective crystallization

The core of our strategy lies in leveraging the ion diffusion differences to achieve selective salt crystallization, where the disparity in ion diffusion coefficients governs the composition of the crystallized salts. During evaporation and crystallization through a floating porous medium, ion transfer is primarily occurs via three mechanisms[24,27-34]: capillary flow, ion diffusion, and

convection (Figure 3.1a). Capillary flow carries ions along with water to the evaporation surface, where the ions are concentrated as water evaporates. Convection, on the other hand, refers to the fluid motion driven by density gradients caused by ion accumulation at the evaporation surface. As water evaporates, ions become more concentrated at the surface, increasing local density. This density difference induces a downward movement of the concentrated solution into the bulk, while less dense fluid rises to replace it[29,32]. Moreover, the concentration gradient also drives upward water osmosis, which is non-selective. However, the flux of osmosis flow is calculated to be as low as 3×10^{-5} kg·m^{-2}·h^{-1}, which is negligible compared to the evaporation rate, typically exceeding 0.1 kg·m^{-2}·h^{-1} (Supplementary Text 3.1). Both capillary flow and convection are non-ion-selective processes because they transfer ions through bulk fluid movement[28,32], thus interfering with selective crystallization. In contrast, ion diffusion, driven by the concentration gradient between the mixed source solution and the evaporation interface where the ions are concentrated, allows ions to move independently according to their respective diffusion coefficients[35,36] (Na^+: 0.87×10^{-9} m^2·s^{-1} and K^+: 2.17×10^{-9} m^2·s^{-1}) (Supplementary Text 3.2).

To achieve selective high-purity salt crystallization, it is crucial to suppress and minimize the non-selective processes. Notably, convection can be suppressed by controlling the pore size of the evaporator according to

literature[29]. Therefore, when convection is suppressed, surface ion concentration primarily governed by upward capillary flow and downward diffusion[3,28]. For a specific ion, the critical scenario arises when its concentration reaches saturation at the evaporation surface, and its diffusion rate is maximized. If the upward capillary flow rate surpasses the maximum downward diffusion rate, crystallization will take place; otherwise, crystallization will not occur[3,15,28]. Therefore, under a rationally controlled design, ions with higher diffusion coefficients can be made to diffuse back into the mixed source solution, while ions with lower diffusion coefficients can be made to selectively accumulate at the evaporation interface, leading to their selective crystallization. This process would enable an efficient ion separation by favoring the crystallization of ions with lower diffusion coefficients.

3.2.2 Convection suppression

Péclet number (*Pe*) defined by the ratio of ion convection rate to its diffusion rate is commonly used to assess the effect of convection on overall ion transfer[32]. When *Pe* is below 1, the contribution by convection is smaller than by diffusion[29]. According to *Carman-Kozeny* equation[32], the ion transfer via convection within the pores of the porous membrane is effectively suppressed due to the increased mass transfer resistance. As the pore size decreases, ion convection is further decreased, as indicated by the calculated

Pe in Figure 3.1b. For the floating porous membrane, the diffusion length can be considered to be equivalent to the membrane thickness, which affects *Pe* via affecting diffusion rate. As the membrane thickness decreases, *Pe* is reduced because the diffusion rate increases disproportionately. These results suggest that reducing either the pore size or the membrane thickness can lead to a reduced convection effect on overall ion transfer.

We first used COMSOL to simulate the transfer process of Na^+/K^+ through a 7 mm-thick membrane with different pore sizes. To simulate the crystallization process, both NaCl and KCl were maintained at a saturated surface concentration of 150 $g \cdot L^{-1}$. Due to the constraint of electroneutrality, the transfer rates of Na^+ and K^+ were assessed using NaCl and KCl, with their diffusion coefficients represented by the mutual diffusion coefficients of NaCl and KCl, which are 1.34×10^{-9} $m^2 \cdot s^{-1}$ and 2.51×10^{-9} $m^2 \cdot s^{-1}$, respectively (see more details in Supplementary Texts 3.1 and 3.3). As shown in Figure 3.1c, our COMSOL simulation demonstrates that the convection rates of NaCl and KCl decrease consistently as the pore size is reduced, becoming lower than the diffusion rates once the pore size is smaller than 5 μm. In contrast, the diffusion rates of NaCl and KCl follow a similar trend: they decrease as the pore size is reduced from 100 to 1 μm and remain stable thereafter, at ~1.9 $g \cdot m^{-2} \cdot h^{-1}$ for NaCl and ~3.5 $g \cdot m^{-2} \cdot h^{-1}$ for KCl, respectively (Figure 3.1c). The initial decline in diffusion rates can be attributed to the changes in the concentration gradient

caused by convection suppression (Figure 3.1d). Notably, at a pore size of 0.1 μm, the diffusion rates of NaCl and KCl were significantly higher than their corresponding convection rates, exceeding them by three orders of magnitude. This finding indicates that diffusion dominates ion transfer when the pore size is reduced below 0.1 μm, resulting in different ion transfer rates due to the distinct diffusion coefficients of Na^+ (0.87×10^{-9} $m \cdot s^{-1}$) and K^+ (2.17×10^{-9} $m \cdot s^{-1}$) (Supplementary Text 3.1 and Figure 3.1). Consequently, the ratio of the downward transfer rates of KCl to NaCl increased from 1 to 1.86 as the pore size decreased from 10 to below 0.1 μm, after which this ratio stabilized (Supplementary Figure 3.2). Furthermore, for a membrane pore size of 0.1 μm, the NaCl/KCl concentration profile across the 7-mm-thick membrane exhibits an approximately linear gradient extending from the evaporation surface to the membrane bottom (Figure 3.1d). This observation aligns with Fick's law of diffusion, suggesting that ion transport under these conditions is predominantly diffusion-controlled. In contrast, at larger pore sizes of 10 μm and 100 μm, the NaCl concentration drops sharply from 150 $g \cdot L^{-1}$ to near zero within the upper half of the membrane, suggesting that convection becomes dominant in these cases (Figure 3.1d).

During the evaporation process, salt crystals can form on the membrane surface once the concentrations of NaCl or KCl at the evaporation interface reach their saturation points[3,15]. At pore sizes smaller than 0.1 μm, the

difference in the downward transfer rates of Na^+ and K^+ caused by diffusion would be enhanced, thereby promoting selective NaCl crystallization. Conversely, at larger pore sizes where convection dominates, increased downward convective transfer of salts suppresses surface salt crystallization, and the diminished difference between Na^+ and K^+ transfer rates reduce selectivity. To further validate this selective crystallization process, a ceramic membrane (Supplementary Figures 3.3 and 3.4), which has no inherent ion selectivity, was used as the evaporator (Supplementary Text 3.3) to eliminate the potential influence of the membrane material on crystallization during wind-driven evaporation. As shown in Figure 3.1e, the evaporation of a mixed NaCl/KCl solution with an equal mass ratio at a total salt concentration of 40 $g \cdot L^{-1}$ revealed that the salt crystallization rate increased as the pore size decreased (Supplementary Figure 3.5). Notably, the purity of NaCl in the crystallized salts increased from ~50% to ~63% as the pore size was decreased to 30 nm (Figure 3.1e), demonstrating enhanced selectivity for Na^+ crystallization. These findings preliminarily confirm that suppressing convection can effectively enrich NaCl in the crystallized salts from a mixed NaCl/KCl solution.

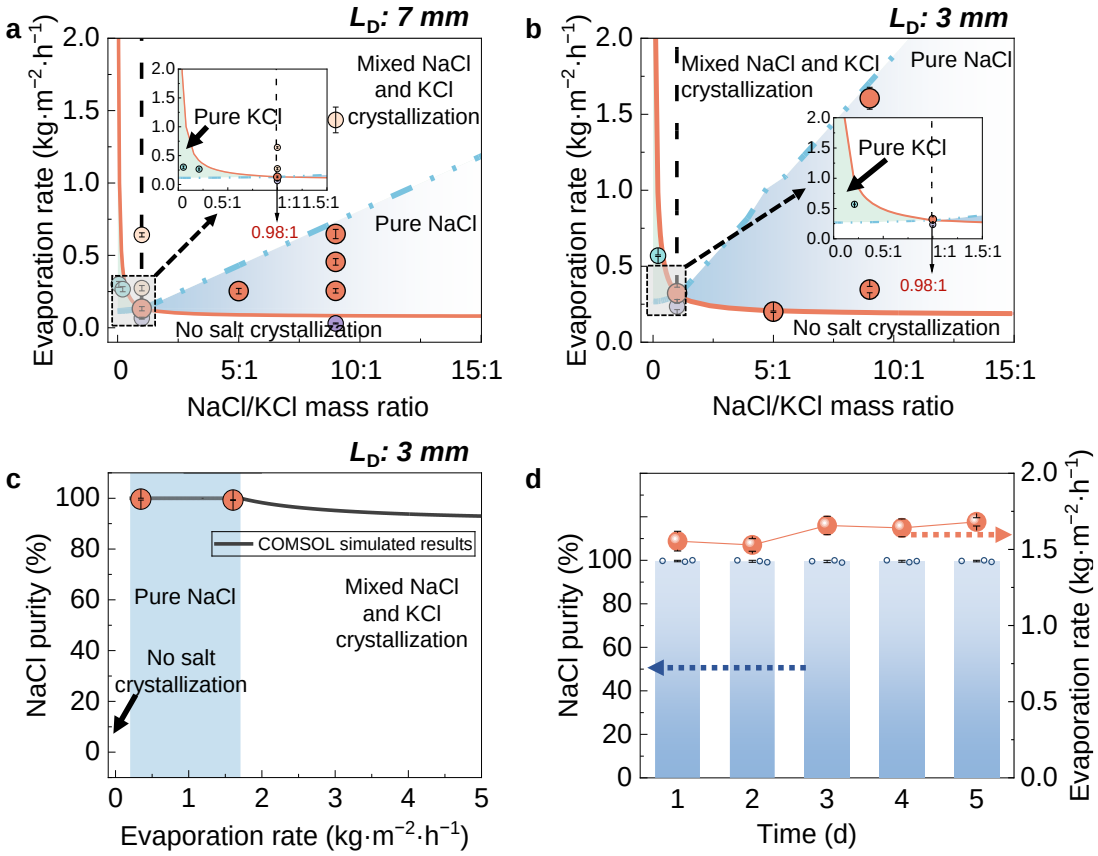

Figure 3.2 COMSOL simulation and experimental results of the salt crystallization states on the surface of the ceramic membranes by controlling the capillary flow and ion diffusion. Salt crystallization states under different evaporation rates and NaCl/KCl mass ratios through the ceramic membrane with the diffusion length (L_D) of (a) 7 mm, and (b) 3 mm. The total salt concentration of mixed NaCl/KCl solution was maintained at 40 g·L^{-1}. The four regions divided by the red solid line and blue dot dash line in the Figures represent different crystallization states: pure NaCl, no salt crystallization, mixed NaCl and KCl crystallization, and pure KCl. The data points in different regions represent experimental crystallization states from five-day continuous measurements for the verification of COMSOL simulated results, and error bars

represent standard deviation from five measurements. The inset highlights the boundary between pure KCl and pure NaCl crystallization regions. (c) The effect of evaporation rate on the NaCl purity in the crystallized salts when evaporating simulated seawater with a NaCl/KCl mass ratio of 9:1 through a 3 mm-thick ceramic membrane. The blue shaded region represents the COMSOL simulated evaporation rate for pure NaCl crystallization and the data points represent experimental evaporation rate for pure NaCl crystallization from five-day continuous measurements. The dashed line represents simulated NaCl purity under different evaporation rates. (d) The stability of the 3 mm-thick ceramic membrane for high-purity NaCl production from the simulated seawater. The evaporation was driven by wind at 25^{o}C.

3.2.3 Capillary flow and diffusion control for high-purity salt production

Reducing the pore size of the porous membrane effectively suppresses convection, enabling ion transfer within the membrane to occur primarily through capillary flow and diffusion. To further explore the selective crystallization, we utilized a ceramic membrane with a pore size of 30 nm as the evaporator (Pe=2.20 × 10^{-4}), paired with a mixed NaCl/KCl solution at a total salt concentration of 40 g·L^{-1}. In this evaporation system, selective crystallization is primarily governed by the competition between the capillary flow rate (U, kg·m^{-2}·h^{-1}) and the downward diffusion rate (R, kg·m^{-2}·h^{-1}) of NaCl

and KCl. As mentioned above, R reaches its maximum value (R_{max}) when the salt concentration at the evaporation interface approaches saturation. Since salt crystal forms only when its capillary flow rate exceeds the maximum diffusion rate, salt crystallization can be categorized into four states based on the disparity of U and R_{max} of NaCl/KCl:

$U_{NaCl} > R_{max}^{NaCl}$ and $U_{KCl} > R_{max}^{KCl}$	Mixed NaCl and KCl
$U_{NaCl} > R_{max}^{NaCl}$ and $U_{KCl} \leq R_{max}^{KCl}$	Pure NaCl
$U_{NaCl} \leq R_{max}^{NaCl}$ and $U_{KCl} \leq R_{max}^{KCl}$	No salt crsystallization
$U_{NaCl} \leq R_{max}^{NaCl}$ and $U_{KCl} > R_{max}^{KCl}$	Pure KCl

U can be governed by the Equation 1[28,29]:

$$U_i = \frac{w_i}{w_{H_2O}} E_V \qquad \text{Equation 3.1}$$

where w_i and w_{H_2O} represent the mass proportion of salt i and water in the mixed source solution, and E_V is the evaporation rate ($kg \cdot m^{-2} \cdot h^{-1}$).

R can be modulated according to Fick's first law (Equation 2)[28,36]:

$$R_i = D_i \frac{\Delta c}{L_D} \qquad \text{Equation 3.2}$$

where R_i is the mutual diffusion coefficient ($m^2 \cdot s^{-1}$) of salt, Δc is the salt concentration difference ($g \cdot L^{-1}$), and L_D is the diffusion length (m).

The COMSOL simulation results are shown as different regions in Figure 3.2a. When the diffusion length was 7 mm, no salt crystallization occurred at a

low evaporation rate. Under these conditions, both U_{KCl} and U_{NaCl} were smaller than their respective R_{max}, preventing NaCl and KCl from reaching saturation at the evaporation surface (Supplementary Figure 3.6). With a slight increase in the evaporation rate, interestingly, salt crystallization occurred, yielding either pure NaCl or pure KCl crystals, depending on the NaCl/KCl mass ratio in the mixed source solution (Figure 3.2a). When the NaCl/KCl mass ratio exceeded 0.98:1, pure NaCl could be selectively crystallized. In this case, the R_{max}^{NaCl} was calculated to be consistently lower than R_{max}^{KCl} due to the lower diffusion coefficient of Na^+. Consequently, as evaporation rate was increased, U_{NaCl} exceeded R_{max}^{NaCl} first, while U_{KCl} remained below R_{max}^{KCl}. Conversely, when the NaCl/KCl mass ratio was below 0.98:1, pure KCl was selectively crystallized due to the higher concentration of K^+ in the mixed source solution. As the evaporation rate was increased further, both U_{NaCl} and U_{KCl} exceeded their respective R_{max}, resulting in the co-crystallization of NaCl and KCl (Supplementary Figure 3.7).

To validate the COMSOL model, selective crystallization experiments were conducted at various NaCl/KCl mass ratios, with the evaporation rate controlled using wind (data points in Figures 3.2a-c). According to our simulation results presented in Figure 3.2a (Pure NaCl region), when the NaCl/KCl mass ratio was 1:1 and the membrane thickness was maintained at 7 mm, selective crystallization was predicted to occur within a narrow evaporation rate range of

0.13~0.14 $kg \cdot m^{-2} \cdot h^{-1}$. Under these conditions, slight variations in environmental factors such as temperature, humidity, and wind speed could cause fluctuations in the evaporation rate, leading to a decrease in NaCl purity. As indicated by the data points in Figure 3.2a, the purity of the collected salt at a NaCl/KCl ratio of 1:1 was only 78% when the average evaporation rate was controlled at 0.14 $kg \cdot m^{-2} \cdot h^{-1}$ (Supplementary Figure 3.7). When the average evaporation rate was further increased to 0.25 $kg \cdot m^{-2} \cdot h^{-1}$, the NaCl purity in the collected salt decreased to approximately 61% (Supplementary Figure 3.7), consistent with the COMSOL simulation results (Mixed NaCl and KCl crystallization region in Figure 3.2a). When the NaCl/KCl mass ratios were increased to 5:1 and 9:1, the membrane was predicted to support broader evaporation rate ranges for high-purity NaCl crystallization, specifically between 0.09~0.43 $kg \cdot m^{-2} \cdot h^{-1}$ and 0.08~0.73 $kg \cdot m^{-2} \cdot h^{-1}$, respectively (Figure 3.2a). Consequently, NaCl with purities of 95.32% and 99.59% were selectively crystallized at average evaporation rates of 0.25 and 0.65 $kg \cdot m^{-2} \cdot h^{-1}$, respectively (Figure 3.2a and Supplementary Figures 3.8 and 3.10). In the region where pure KCl could be selectively crystallized, at a mass ratio of 0.2:1, the corresponding evaporation rate range was between 0.12~0.42 $kg \cdot m^{-2} \cdot h^{-1}$ (Pure KCl region in Figure 3.2a). Under these conditions, the collected salt exhibited a KCl purity of 91.23% at an average evaporation rate of 0.26 $kg \cdot m^{-2} \cdot h^{-1}$ (Supplementary Figure 3.11).

Reducing the diffusion length enhances the diffusion rate (Equation 3.2),

thereby amplifying the difference between R_{max}^{NaCl} and R_{max}^{KCl} and leading to a broader evaporation rate range for high-purity salt crystallization. As shown in Figure 3.2b, using a 3 mm-thick membrane allows selective crystallization to be achieved over an expanded evaporation rate range compared to a 7 mm-thick membrane (Figure 3.2a). For instance, at a NaCl/KCl mass ratio of 1:1, high-purity NaCl crystallization was predicted within an increased evaporation rate range of 0.3~0.33 $kg \cdot m^{-2} \cdot h^{-1}$ (Pure NaCl region in Figure 3.2b), resulting in crystallized salts with a NaCl purity of 90.77% at an average evaporation rate of 0.32 $kg \cdot m^{-2} \cdot h^{-1}$ (Supplementary Figure 3.13). When the NaCl/KCl mass ratios were increased to 5:1 and 9:1, the evaporation rate ranges for high-purity NaCl crystallization expanded to 0.22~1.01 $kg \cdot m^{-2} \cdot h^{-1}$ and 0.20~1.71 $kg \cdot m^{-2} \cdot h^{-1}$, respectively (Figure 3.2b). Consequently, NaCl with purities of 99.94% and 99.28% were obtained at average evaporation rates of 0.20 $kg \cdot m^{-2} \cdot h^{-1}$ and 1.60 $kg \cdot m^{-2} \cdot h^{-1}$, respectively (Supplementary Figures 3.14 and 3.15). For pure KCl crystallization, the evaporation rate range was predicted to be between 0.3~1.0 $kg \cdot m^{-2} \cdot h^{-1}$ at a NaCl/KCl mass ratio of 0.2:1 (Pure KCl region in Figure 3.2b), and experimental results demonstrated 99.49% purity of KCl crystallization at an average evaporation rate of 0.57 $kg \cdot m^{-2} \cdot h^{-1}$ (Supplementary Figure 3.16). These results demonstrate that high-purity salt crystallization can be achieved by simply regulating diffusion and capillary flow, underscoring the feasibility of the diffusion-driven selective crystallization strategy.

Since selective crystallization has significant implications for resource extraction and wastewater treatment[33,37], our strategy can be also employed for selective NaCl extraction from simulated seawater, which has an NaCl/KCl mass ratio of 9:1. Both theoretical calculations and experimental results confirmed that pure NaCl could be extracted at evaporation rates between 0.20 and 1.71 $kg \cdot m^{-2} \cdot h^{-1}$ using a 3 mm-thick membrane by evaporating simulated seawater (Pure NaCl region in Figure 3.2c). Moreover, to test its stability, we conducted five-day continuous evaporation measurements of NaCl extraction from simulated seawater. As shown in Figure 2d, an exceptionally high NaCl purity of 99.64% was obtained continuously (Supplementary Figure 3.17), convincingly demonstrating the capability of DiSC to selectively extract high-purity NaCl.

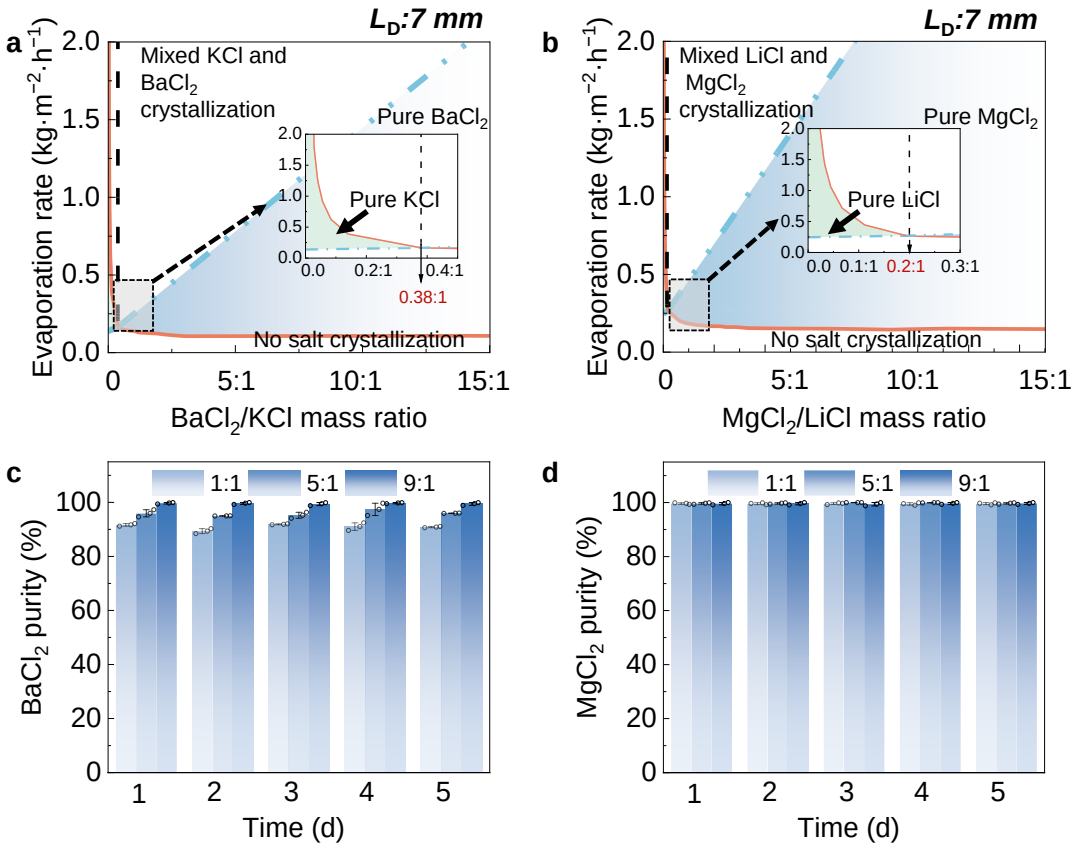

Figure 3.3 Selective crystallization of mixed Ba^{2+}/K^+ and Mg^{2+}/Li^+ system. COMSOL simulated salt crystallization states of the (a) $BaCl_2$/KCl and (b) $MgCl_2$/LiCl through the 7 mm-thick ceramic membrane. The four regions divided by the red solid line and blue dot dash line in the Figures represent COMSOL simulated different crystallization states: pure $BaCl_2$ or $MgCl_2$, no salt crystallization, mixed salt crystallization, and pure KCl or LiCl. The inset highlights the boundary between different single salt crystallization regions (pure $BaCl_2$ and pure KCl in Figure a and pure $MgCl_2$ and pure LiCl in Figure b). The five-day continuous experimental measurements for high-purity salt production via a 7 mm-thick ceramic membrane from mixed (c) $BaCl_2$/KCl and (d) $MgCl_2$/LiCl solution with a mass ratio of 1:1, 5:1 and 9:1. The total

concentrations of $BaCl_2$/KCl solution and $MgCl_2$/LiCl solution were maintained at 40 and 80 g·L^{-1}, respectively. The evaporation of $BaCl_2$/KCl solution was driven by wind at 25°C, while the evaporation of $MgCl_2$/LiCl solution was driven by electrical heating at 40°C.

3.2.4 Versatility demonstration

In addition to the Na^+/K^+ system, DiSC can also be applied to other mixed ion systems. We demonstrated the versatility of this strategy with Ba^{2+}/K^+ and Mg^{2+}/Li^+ separations, where the paired ions exhibit similar solubility but different diffusion coefficients (Supplementary Figure 3.18). For $BaCl_2$/KCl mixed source solutions, $BaCl_2$ has a lower diffusion coefficient (1.39×10^{-9} $m^2 \cdot s^{-1}$) compared with KCl, allowing high-purity $BaCl_2$ to be selectively crystallized when the mass ratio of $BaCl_2$/KCl exceeds 0.38:1 and the evaporation rate is above approximately 0.10 kg·m^{-2}·h^{-1} in the 7 mm-thick ceramic membrane (Pure $BaCl_2$ region in Figure 3.3a). Similarly, high-purity $MgCl_2$ can be selectively crystallized due to its lower diffusion coefficient (1.25×10^{-9} $m^2 \cdot s^{-1}$ for $MgCl_2$ and 1.37×10^{-9} $m^2 \cdot s^{-1}$ for LiCl) when the mass ratio of $MgCl_2$/LiCl exceeds 0.2:1 and the evaporation rate is above approximately 0.15 kg·m^{-2}·h^{-1} (Pure $MgCl_2$ region Figure 3.3b).

Guided by the simulation results, five-day continuous measurements were

conducted to crystallize high-purity $BaCl_2$ and $MgCl_2$ using the 7 mm-thick ceramic membrane. Wind-driven evaporation at 25°C was employed to facilitate the selective crystallization of a $BaCl_2$/KCl mixed solution. As shown in Figure 3.3a, high-purity $BaCl_2$ crystallization was predicted within an expanded evaporation rate range of 0.14~0.30 $kg \cdot m^{-2} \cdot h^{-1}$ at a $BaCl_2$/KCl mass ratio of 1:1. Correspondingly, the purity of $BaCl_2$ in the crystallized salts reached 91.15% when the average evaporation rate was controlled at 0.27 $kg \cdot m^{-2} \cdot h^{-1}$ (Figure 3c and Supplementary Figure 3.19). When the $BaCl_2$/KCl mass ratios were increased to 5:1 and 9:1, the evaporation rate ranges for high-purity $BaCl_2$ crystallization expanded to 0.12~0.80 $kg \cdot m^{-2} \cdot h^{-1}$ and 0.11~1.32 $kg \cdot m^{-2} \cdot h^{-1}$, respectively (Figure 3.3a). Consequently, $BaCl_2$ with purities of 95.89% and 99.64% were obtained at average evaporation rates of 0.77 and 0.21 $kg \cdot m^{-2} \cdot h^{-1}$, respectively (Supplementary Figure 3.19).

For the crystallization of high-purity $MgCl_2$ from an $MgCl_2$/LiCl mixed solution, the evaporation rate is restricted by the low saturated vapor pressure of the mixed $MgCl_2$/LiCl solution during wind-driven evaporation[38]. Therefore, heat-driven evaporation was applied for the selective crystallization. As illustrated in Figure 3.3b, the evaporation rate ranges for high-purity $MgCl_2$ crystallization were predicted to be extensive (e.g., 0.17~0.48 $kg \cdot m^{-2} \cdot h^{-1}$ at a mass ratio of 1:1, 0.15~1.39 $kg \cdot m^{-2} \cdot h^{-1}$ at a mass ratio of 5:1, and 0.14~2.34 $kg \cdot m^{-2} \cdot h^{-1}$ at a mass ratio of 9:1). Consequently, all crystallized salts in our

experimental results (Figure 3.3d) exhibited $MgCl_2$ purities exceeding 99.60% when the average evaporation rates were controlled at 0.40, 0.38, and 0.43 $kg \cdot m^{-2} \cdot h^{-1}$, respectively (Supplementary Figure 3.20). These results demonstrate the versatility of the DiSC strategy across various ion systems. Overall, the unprecedented ion separation performance based on ion diffusion coefficients was clearly demonstrated through the one-step evaporation process using the designed porous membrane. This represents the first successful selective crystallization of high-purity salts directly from a mixed source solution based on differences in diffusion coefficients.

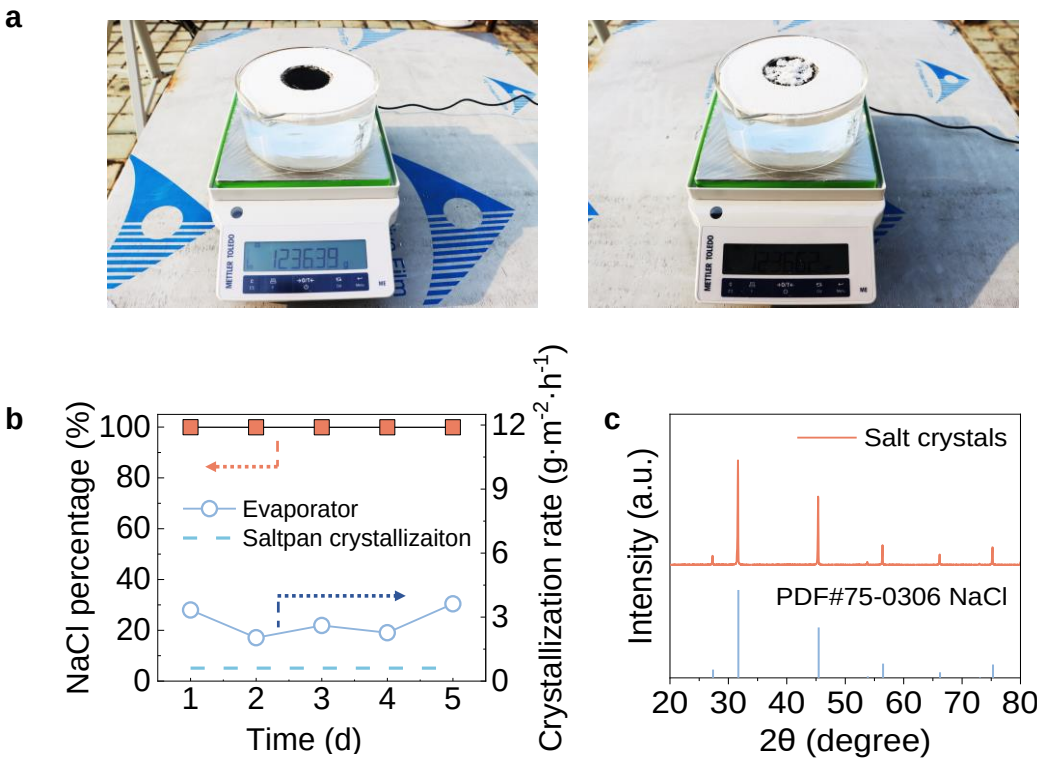

Figure 3.4 Outdoor high-purity NaCl production. (a) Photograph of the solar evaporation system under natural solar irradiation. (b) Solar intensity and wind

velocity during the outdoor experiment. (c) NaCl proportion in salt crystals and evaporation rate during long-term evaporation of mixed Na^+/K^+ solution prepared from real seawater.

3.2.5 Outdoor high-purity NaCl production

A solar-driven evaporation system based on ceramic membranes was developed for Na^+/K^+ separation from real seawater to assess its potential for high-purity NaCl extraction in real-world applications. To validate its performance, a practical application test of this evaporation system was conducted at Sun Yat-Sen University (Guangzhou, China). As shown in Figure 5a, the 7 mm-thick ceramic membrane modified with a black polypyrrole (PPy) was floated on seawater (Figure 3.4). Under natural sunlight, the NaCl proportion in the collected salt crystals remained stable at 99.91%, with an average evaporation rate of 0.64 $kg \cdot m^{-2} \cdot h^{-1}$ (Figures 3.4b and 3.4c). This demonstrates that the selective crystallization system is effective not only under controlled laboratory conditions but also in practical applications (Figure 3.4c), providing stable and efficient Na^+/K^+ separation. These results underscore the practical potential of the system for selective NaCl crystallization from seawater, even under natural environmental conditions.

3.3 Discussion

3.3.1 Role of solubility on the selective crystallization efficiency

Beyond diffusion coefficients, salt solubility plays a crucial role in separation efficiency. During salt crystallization, the concentration gradient (Δc) is defined by the difference between the salt's saturation concentration and its bulk concentration. Higher solubility leads to a greater saturation concentration, resulting in a larger concentration gradient and an increased diffusion rate (R). For example, the solubility of KCl increases with temperature (38 g KCl/100 g H_2O at 25°C and 51 g KCl/100 g H_2O at 90°C), which enhances the concentration gradient and consequently increases the back diffusion rate. As a result, when evaporating a 1:1 mixed NaCl/KCl solution using electric heating at 90°C, 61% NaCl selectively crystalized on the 7 mm-thick ceramic membrane at an evaporation rate of 4.5 $kg \cdot m^{-2} \cdot h^{-1}$ (Supplementary Figure 3.22). In contrast, the NaCl proportion in salt crystals remained around 50% at an evaporation rate of 0.6 $kg \cdot m^{-2} \cdot h^{-1}$ at 25°C (Supplementary Figure 3.7). Our simulation results further indicate that even at higher evaporation rates, the NaCl proportion would stabilize at 50% (Figure 3.2). These findings strongly suggest that the solubility of the salt plays a critical role in determining the selectivity of crystallization.

3.3.2 Conventional solar evaporator for salt rejection or salt crystallization

Solar-driven evaporation systems show promising prospects for environmentally friendly and cost-effective seawater desalination. However, a significant challenge in these systems is the accumulation of crystallized salts on the evaporator's surface due to water evaporation, which blocks sunlight and diminishes efficiency[29,30,34,39]. Traditional designs typically address this issue by preventing salt crystallization through enhancing convection or diffusion process[29,30,40,41]. The "no salt crystallization" region shown at the bottom of Figure 3.2a illustrates this salt rejection approach commonly employed in these evaporators. Conversely, innovative strategies have achieved stable salt crystallization and water evaporation by rationally separating the light absorbing surface from the salt crystallization surface and reducing convection and diffusion processes[34,39]. This approach is illustrated by the "mixed salt crystallization" region at the top of Figure 3.2a. Our theoretical simulations provide a comprehensive and robust framework for elucidating and modeling ion transfer and salt crystallization in diverse solar evaporator designs. This framework is highly versatile and can be broadly applied to performance optimization for solar evaporators across different designs and operational conditions.

3.3.3 Effect of membrane microstructure on the ion diffusion and convection flow

Ion diffusion and convection flow are significantly affected by the microstructure of the porous membrane such as porosity and pore size[32,36]. The ion diffusion coefficients in the porous membranes are typically lower than those in the mixed source solutions due to the reduced solution phase volume and increased diffusion length[41,45]. This effect is captured via multiplying the bulk diffusion coefficient by the tortuosity and porosity of the membrane. Thus, in COMSOL simulation, the ion diffusion coefficient of Na^+ and K^+ in the ceramic membrane were 2.33×10^{-11} and 5.83×10^{-11} $m^2 \cdot s^{-1}$, respectively. The membrane's small pore size similarly constrains convection flow due to the increased resistance to fluid flow. The increased resistance is quantified by the *Carman–Kozeny (C–K)* equation, which relates fluid flow to the pore size and porosity of the membrane. As the pore size decreases, this resistance significantly increases, thereby reducing the convection rate.

3.3.4 Strategies to further increase salt production rate in selective crystallization

Salt production rate can be increased by increasing evaporation rate. Meanwhile, diffusion rate should also be enhanced to ensure the purity of crystallized salts. According to Figures 3.2a and 3.2b, reducing the diffusion

length can lead to a higher evaporation rate for selective crystallization. High evaporation rate is generally achieved in industrial crystallization systems, such as MVR. When integrating the ceramic membrane into these industrial systems, the high-purity NaCl production rate can be increased from 8.64 × 10^{-3} kg·m^{-2}·h^{-1} at an evaporation rate of 0.24 to 1.21 kg·m^{-2}·h^{-1} at an evaporation rate of 34.16 kg·m^{-2}·h^{-1} by reducing the diffusion length from 7 to 0.05 mm. For this integration, the theoretical COMSOL model developed in this study can serve as an essential tool for guiding production processes, exhibiting considerable promise and potential for wide-ranging industrial applications.

3.3.5 Applicability of the DiSC strategy for selective crystallization of other valuable ions

Effective separation of valuable ions such as rare earth elements is critical for sustainable resource management, and the proposed method offers promising advancements in this area. Rare earth metal ions, such as La^{3+}, exhibit significantly low diffusion coefficients (0.619 × 10^{-9} m^2·s^{-1})[42], which favors their selective crystallization using the DiSC strategy. For ions with higher diffusion coefficients or mixed ion systems with minimal diffusion difference, DiSC strategy can regulate ion diffusion coefficients through the interactions between the ions and the pores of the membrane, such as electrostatic forces or coordination effects[16,43]. By incorporating functional groups into the membrane's pores, ion diffusion coefficients can be modulated

to enable selective crystallization[11,35,44]. For example, crown ether groups can be incorporated to membrane pores to selectively complex with Li^{+}[11], reducing its effective diffusion coefficient relative to Mg^{2+}, thus facilitating its crystallization[11,45]. This strategy can be extended to improve the selective crystallization of other ions, thereby enhancing the ion separation efficiency of the DiSC strategy.

3.3.6 Impacts of fluctuations in environmental conditions on selective crystallization performance

Fluctuations in environmental conditions (e.g., sudden changes in wind speed, humidity, or temperature) can cause variations in the evaporation rate during the evaporation–crystallization process[46], which may potentially affect the selectivity of salt crystallization. To address this issue, the theoretical model (as shown in this Figures 3.2 and 3.3) can be utilized to determine the allowable range of evaporation rates for maintaining selective crystallization. As shown in Figure 3.2a, when the NaCl/KCl mass ratios of the source solution is 9:1, the membrane was predicted to support broader evaporation rate ranges for high-purity NaCl crystallization, specifically 0.08~0.73 $kg \cdot m^{-2} \cdot h^{-1}$ (Figure 3.2a). Thus, when the evaporation rate fluctuates within the designed range, the selective crystallization performance remains stable and unaffected.

3.3.7 Potential solution to membrane fouling caused by organic matter or colloids in real seawater/brine

In addition to salts, real seawater or brine often contains organic matter and colloidal particles, which may accumulate on the membrane surface, leading to pore blockage[47] and, consequently, impairing the performance of selective crystallization in large-scale applications. To mitigate this issue, two strategies can be implemented. First, prior to selective crystallization, mature pretreatment processes such as flocculation, sedimentation, or sand filtration can be employed to reduce the concentration of these contaminants[48], thereby minimizing their impact on the crystallization process. Second, the membrane evaporator can be designed with anti-fouling features, such as hydrophilic coatings. For instance, applying a Polyethyleneimine (PEI) layer can effectively prevent fouling[49,50] and enhance long-term operational stability. These strategies, combined with the selective crystallization process, offer a promising approach to improve the sustainability and performance of large-scale systems.

3.4 Conclusion

This chapter presents a novel and effective strategy for selective crystallization by leveraging differences in their diffusion coefficients. Focusing on fundamental physicochemical properties simplifies the separation process and avoids the complex operational conditions typically required for such separations. Our findings not only validate the theoretical predictions but also

highlight the potential of this method for various industrial applications, such as resource extraction. This strategy paves the way for the development of advanced salt separation technologies that are both efficient and environmentally sustainable.

3.5 Methods

3.5.1 Molecular dynamic (MD) simulation of ion diffusion coefficients

To illustrate the differential diffusion of Na^+ and K^+ during evaporation, molecular simulations were conducted to determine the diffusion coefficients of Na^+ and K^+. The extended simple point charge (SPC/E) model was used to represent water molecules[51]. For the ions (Na^+, K^+, and Cl^-), the force-field parameters formulated by Merz et al. were adopted[52], optimized for hydration free energy and shell structure (Supplementary Table 3.1). Nonbonding interactions, including electrostatic and van der Waals forces, were modeled using the particle-particle-particle-mesh (PPPM) algorithm with an accuracy of 0.0001[53], and the 12-6 Lennard-Jones (LJ) potential was truncated at 0.9 nm. The SHAKE algorithm was applied to O-H bonds to mitigate high-frequency vibrations[54]. Finally, Lorentz-Berthelot mixing rules were employed to model interactions between different atomic species. To simulate the ion concentration gradient in Figure 2d, Na^+, K^+, and Cl^- concentrations in both low (Part I) and high (Part II) ion concentration segments are shown in Supplementary Table

3.2. The composite system was constructed by introducing ions into water with periodic boundary conditions (PBC) in all directions. Two baffles were placed at Z = -3.60 nm and Z = 2.45 nm to prevent cross-period movement. The PBC dimensions were 3.20 × 3.40 × 20.00 nm^3. PACKMOL software was used to randomly insert molecules and ions. All MD simulations were conducted using the Large-scale Atomic/Molecular Massively Parallel Simulator (LAMMPS)[55], with a timestep of 2.0 fs. In the pre-equilibrium stage, a baffle at Z = 0 nm allowed components to relax in the NVT ensemble for 5 ns at 298.15 K, controlled by the Nose-Hoover thermostat. After equilibrium, the baffle was removed, and the system was run for an additional 5 ns for diffusion behavior analysis.

3.5.2 Mechanistic mode development for selective salt crystallization

To design the selective crystallization system and simulate salt crystallization states, we developed a mechanistic model by coupling fluid flow and ion transfer within the porous membrane. The numerical simulation was performed using the finite element method in COMSOL Multiphysics 6.1, which integrates laminar flow and ion transport into a time-dependent solver[29,33]. To better demonstrate the impacts of convection minimization through pore size reduction on selective crystallization, membrane parameters from Figure 1e were used in the simulation, ensuring consistency between the experimental setup and the simulation conditions. Due to the symmetry of the membrane in

Figure 3.1e, a two-dimensional axisymmetric model of the membrane (Thickness:7 mm, Diameter: 55 mm, Porosity: 32%) was built for simulation analysis. The membrane was modeled as a homogenized porous medium and the concentration gradients on both sides of the membrane were assumed to be steady-state. The average pore size of membranes in Figure 1d are 0.1, 10 and 100 μm, while those in Figures 3.2 and 3.3 have an average pore size of 0.03 μm. Ion transfer in the porous membrane is governed by a combination of the continuity equation and the momentum equation, which are described by the Brinkman equations[32]. More detailed descriptions of simulation setup, parameter selection, and underlying assumptions can be seen in Supplementary Texts 3.8 and 3.9.

3.5.3 Evaporator setup for selective crystallization demonstration

The ceramic membrane for the evaporator setup was secured within a circular PS foam ring with the junctions sealed using waterproof silicone. For wind-driven evaporation, membrane surface was blown by a fan at 25°C, and the evaporation rate was controlled by the air velocity. For the heat-driven evaporation, the mixed source solution was heated by an electrical heater (Aozlla) at a certain temperature. For the solar evaporator shown in Figure 3.4, a 7-mm thick ceramic membrane was placed in a container containing pyrrole

monomer solution, ensuring the liquid level was below the membrane thickness. The treated side of the membrane was then immersed in $FeCl_3$ solution for oxidative polymerization at room temperature. Afterward, the black ceramic membrane was thoroughly washed with alcohol via ultrasonic cleaning and dried at 60°C for further experiments. To measure selective crystallization, crystallized salts were collected from the evaporator and dissolved in de-ionized (DI) water. Then the water samples were diluted properly and measured by inductively coupled plasma-optical emission spectrometry (720 ICP-OES, Agilent) and ion chromatography (CIC-D100, SHINE) to determine ion composition.

3.5.4 Real seawater for high-purity NaCl production

Seawater was collected from Victoria Harbor, Hong Kong. Initially, the seawater was filtered through a 0.45 μm cellulose acetate membrane to remove suspended solids. As the study focuses on the separation of Na^+/K^+, ions such as Mg^{2+}, Ca^{2+} and SO_4^{2-} were removed using a chemical precipitation method prior to the Na^+/K^+ separation, which could also be achieved by nanofiltration. The detailed ion compositions of both the raw and treated seawater samples are provided (Supplementary Figure 3.21).

3.5.5 Characterizations

The surface morphology of membranes was characterized by field-

emission scanning electron microscopy (SEM, TESCAN VEGA 3). The porosity and pore size distribution of membranes were measured by a mercury porosimeter (AutoPore V, Micromeritics). The water content angle (WCA) of membranes was determined by the CA meter (OCA20, DataPhysics). The UV-Vis-NIR diffuse reflectance spectra were recorded by an Agilent Cary 5000 spectrometer.

Reference

1 Zuo, P. *et al.* Near-frictionless ion transport within triazine framework membranes. *Nature* **617**, 299–305 (2023).

2 Li, Z. *et al.* Lithium extraction from brine through a decoupled and membrane-free electrochemical cell design. *Science* **385**, 1438–1444 (2024).

3 Song, Y. *et al.* Solar transpiration–powered lithium extraction and storage. *Science* **385**, 1444–1449 (2024).

4 Epsztein, R., DuChanois, R. M., Ritt, C. L., Noy, A. & Elimelech, M. Towards single-species selectivity of membranes with subnanometre pores. *Nat. Nanotechnol.* **15**, 426–436 (2020).

5 Srimuk, P., Su, X., Yoon, J., Aurbach, D. & Presser, V. Charge-transfer materials for electrochemical water desalination, ion separation and the recovery of elements. *Nat. Rev. Mater.* **5**, 517–538 (2020).

6 Sproncken, C. C. M. *et al.* Large-area, self-healing block copolymer membranes for energy conversion. *Nature* **630**, 866–871 (2024).

7 Li, H. *et al.* Na^+-gated water-conducting nanochannels for boosting CO_2 conversion to liquid fuels. *Science* **367**, 667–671 (2020).

8 Pomerantseva, E., Bonaccorso, F., Feng, X., Cui, Y. & Gogotsi, Y. Energy storage: The future enabled by nanomaterials. *Science* **366**, eaan8285 (2019).

9 Tunuguntla, R. H. *et al.* Enhanced water permeability and tunable ion selectivity in subnanometer carbon nanotube porins. *Science* **357**, 792–796 (2017).

10 Yang, Y. *et al.* Large-area graphene-nanomesh/carbon-nanotube hybrid membranes for ionic and molecular nanofiltration. *Science* **364**, 1057–1062 (2019).

11 Warnock, S. J. *et al.* Engineering Li/Na selectivity in 12-Crown-4-

functionalized polymer membranes. *Proc. Natl. Acad. Sci. U. S. A.* **118**, e2022197118 (2021).

12 Zhang, Y. *et al.* Ice-confined synthesis of highly ionized 3D-quasilayered polyamide nanofiltration membranes. *Science* **382**, 202–206 (2023).

13 Yang, S., Wang, Y., Pan, H., He, P. & Zhou, H. Lithium extraction from low-quality brines. *Nature* **636**, 309–321 (2024).

14 Vera, M. L., Torres, W. R., Galli, C. I., Chagnes, A. & Flexer, V. Environmental impact of direct lithium extraction from brines. *Nat. Rev. Earth Environ.* **4**, 149–165 (2023).

15 Chen, X. *et al.* Spatially separated crystallization for selective lithium extraction from saline water. *Nat. Water* **1**, 808–817 (2023).

16 Wang, R. & Lin, S. Pore model for nanofiltration: History, theoretical framework, key predictions, limitations, and prospects. *J. Membr. Sci.* **620** (2021).

17 Violet, C. *et al.* Designing membranes with specific binding sites for selective ion separations. *Nat. Water* **2**, 706–718 (2024).

18 Uliana, A. A. *et al.* Ion-capture electrodialysis using multifunctional adsorptive membranes. *Science* **372**, 296–299 (2021).

19 Wu, X. *et al.* Sustainable lithium extraction enabled by responsive metal-organic frameworks with ion-sieving adsorption effects. *Proc. Natl. Acad. Sci. U. S. A.* **121**, e2309852121 (2024).

20 Xia, Q. *et al.* Solar-enhanced lithium extraction with self-sustaining water recycling from salt-lake brines. *Proc. Natl. Acad. Sci. U. S. A.* **121**, e2400159121 (2024).

21 Sun, Y., Wang, Q., Wang, Y., Yun, R. & Xiang, X. Recent advances in magnesium/lithium separation and lithium extraction technologies from salt lake brine. *Sep. Purif. Technol.* **256** (2021).

22 Zhou, Z. *et al.* Carbon dioxide capture from open air using covalent organic frameworks. *Nature* **635**, 96–101 (2024).

23 Matthews, H. D. & Wynes, S. Current global efforts are insufficient to limit warming to 1.5°C. *Science* **376**, 1404–1409 (2022).

24 Tao, P. *et al.* Solar-driven interfacial evaporation. *Nat. Energy* **3**, 1031–1041 (2018).

25 Xu, N. *et al.* Going beyond efficiency for solar evaporation. *Nat. Water* **1**, 494–501 (2023).

26 Zhao, F. *et al.* Highly efficient solar vapour generation via hierarchically nanostructured gels. *Nat. Nanotechnol.* **13**, 489–495 (2018).

27 Zhou, L. *et al.* 3D self-assembly of aluminium nanoparticles for plasmon-enhanced solar desalination. *Nat. Photonics* **10**, 393–398 (2016).

28 Ni, G. *et al.* A salt-rejecting floating solar still for low-cost desalination. *Energy Environ. Sci.* **11**, 1510–1519 (2018).

29 Zhang, L. *et al.* Highly efficient and salt rejecting solar evaporation via a wick-free confined water layer. *Nat. Commun.* **13**, 849 (2022).

30 Zhang, L. *et al.* Passive, high-efficiency thermally-localized solar desalination. *Energy Environ. Sci.* **14**, 1771–1793 (2021).

31 Chen, C. *et al.* Highly Flexible and Efficient Solar Steam Generation Device. *Adv. Mater.* **29**, 1701756 (2017).

32 Nield, D. A. & Bejan, A. *Convection in Porous Media*. 5th edn, (Springer, 2017).

33 Zhang, C. *et al.* Designing a next generation solar crystallizer for real seawater brine treatment with zero liquid discharge. *Nat. Commun.* **12**, 998 (2021).

34 Shi, Y. *et al.* Solar Evaporator with Controlled Salt Precipitation for Zero Liquid Discharge Desalination. *Environ. Sci. Technol.* **52**, 11822–11830 (2018).

35 Cao, L. *et al.* Switchable Na^+ and K^+ selectivity in an amino acid

functionalized 2D covalent organic framework membrane. *Nat. Commun.* **13**, 7894 (2022).

36 Cussler, E. L. *Diffusion : mass transfer in fluid systems*. 2nd edn, (Cambridge Univ. Press, 2000).

37 Zhang, S. *et al.* Solar-driven membrane separation for direct lithium extraction from artificial salt-lake brine. *Nat. Commun.* **15**, 238 (2024).

38 Li, R., Shi, Y., Shi, L., Alsaedi, M. & Wang, P. Harvesting Water from Air: Using Anhydrous Salt with Sunlight. *Environ. Sci. Technol.* **52**, 5398–5406 (2018).

39 Xu, K., Wang, C., Li, Z., Wu, S. & Wang, J. Salt Mitigation Strategies of Solar‐Driven Interfacial Desalination. *Adv. Funct. Mater.* **31** (2020).

40 Kuang, Y. *et al.* A High-Performance Self-Regenerating Solar Evaporator for Continuous Water Desalination. *Adv. Mater.* **31**, 1900498 (2019).

41 Yang, K., Pan, T., Dang, S., Gan, Q. & Han, Y. Three-dimensional open architecture enabling salt-rejection solar evaporators with boosted water production efficiency. *Nat. Commun.* **13**, 6653 (2022).

42 Dane, J. H. & Topp, C. G. *Methods of Soil Analysis, Part 4: Physical Methods*. (Wiley, 2020).

43 Bruggen, B. V. d., J. Schaep, D. W. & Vandecasteele, C. Influence of molecular size, polarity and charge on the retention of organic molecules by nanofiltration. *J. Membr. Sci.* **156**, 29–41 (1999).

44 Liang, H., Mu, Y., Yin, M., He, P.-P. & Guo, W. Solar-powered simultaneous highly efficient seawater desalination and highly specific target extraction with smart DNA hydrogels. *Sci. Adv.* **9**, eadj1677 (2023).

45 Zofchak, E. S. *et al.* Origins of Lithium/Sodium Reverse Permeability Selectivity in 12-Crown-4-Functionalized Polymer Membranes. *ACS Macro Lett* **10**, 1167–1173 (2021).

46 Chen, Y. *et al.* Large-scale implementation of solar interfacial

desalination. *Nat. Sustain.* (2025).

47 Tayeh, Y. A., Alazaiza, M. Y. D., Alzghoul, T. M. & Bashir, M. J. K. A comprehensive review of RO membrane fouling: Mechanisms, categories, cleaning methods and pretreatment technologies. *Journal of Hazardous Materials Advances* **18**, 100684 (2025).

48 Maartens, A., Swart, P. & Jacobs, E. P. Feed-water pretreatment: methods to reduce membrane fouling by natural organic matter. *J. Membr. Sci.* **163**, 51–62 (1999).

49 Deng, L. *et al.* Fabrication of antifouling thin-film composite nanofiltration membrane via surface grafting of polyethyleneimine followed by zwitterionic modification. *J. Membr. Sci.* **619**, 118564 (2021).

50 Guan, Y. *et al.* Preparation of antifouling TFC RO membranes by facile grafting zwitterionic polymer PEI-CA. *Desalination* **539**, 115972 (2022).

51 Berendsen, H. J. C., Grigera, J. R. & Straatsma, T. P. The missing term in effective pair potentials. *J. Phys. Chem* **91**, 6269–6271 (1987).

52 Li, P., Song, L. F. & Merz, K. M. Systematic Parameterization of Monovalent Ions Employing the Nonbonded Model. *J. Chem. Theory Comput.* **11**, 1645–1657 (2015).

53 Hockney, R. W. & Eastwood, J. W. *Computer simulation using particles*. (Taylor & Francis, Inc., 1988).

54 Ryckaert, J.-P., Ciccotti, G. & Berendsen, H. J. C. Numerical integration of the cartesian equations of motion of a system with constraints: molecular dynamics of n-alkanes. *J. Comput. Phys.* **23**, 327–341 (1977).

55 Plimpton, S. Fast Parallel Algorithms for Short-Range Molecular Dynamics. *J. Comput. Phys.* **117**, 1–19 (1995).

Supporting Information for Chapter 3

1. Water osmosis in the membrane during salt crystallization

During evaporation, osmotic flow can be driven by the osmotic pressure difference between the evaporation surface and the bulk solution. Since this process is non-selective, it may reduce selective crystallization performance. To evaluate this effect, we quantified the osmotic flux during the evaporation of a mixed NaCl/KCl solution at 25°C. First, the osmotic pressure difference ($\Delta\pi$) was calculated using the van't Hoff equation[1]:

$$\Delta\pi = iCRT \qquad \text{Equation 3.3}$$

where i is the van't Hoff factor (For NaCl and KCl, under complete dissociation, $i=2$), C is the solute concentration (mol·mol^{-3}), R is the universal gas constant (8.314 J·mol^{-1}·K), T is the absolute temperature (K).

An osmotic pressure difference of ~20 kPa is generated across the ceramic membrane during salt crystallization, with the corresponding water flux (J) calculated using Darcy's law[2]:

$$J = -\frac{k\Delta P}{\mu L} \qquad \text{Equation 3.4}$$

where ΔP is the pressure difference across the membrane (Pa), k is the permeability of the membrane (m^2), μ is the dynamic viscosity of the fluid (Pa·s), L is the membrane thickness (m).

The flux of osmosis flow through the membrane (3×10^{-5} kg·m^{-2}·h^{-1}) is

significantly lower than the upward transfer rate by capillary flow (0.1 $kg \cdot m^{-2} \cdot h^{-1}$), indicating its negligible impact on selective crystallization.

2. Mutual diffusion coefficient of salt

In salt solution, ions diffuse as ion-pair rather than individually, due to the necessity of maintaining electroneutrality. As a result, the diffusion coefficient of an individual ion can be influenced by its counterion[3-5]. In this context, the mutual diffusion coefficient of the salt can be used to characterize the overall diffusion behavior, which can be quantitatively expressed by the following equation[6]:

$$D_{12}=\frac{|z_1|+|z_2|}{|z_2/D_1|+|z_1/D_2|} \qquad \text{Equation 3.5}$$

where $|z_i|$ and D_{12} are, respectively, the magnitude of the ionic charge and the transport–diffusion coefficient of each ion *i*.

NaCl and KCl share the same anion, so the difference in their diffusion rates is primarily determined by the difference in the diffusion coefficients of Na^+ and K^+, as described by the following equations:

$$D_{NaCl}=\frac{2}{\frac{1}{D_{Na^+}}+\frac{1}{D_{Cl^-}}} \qquad \text{Equation 3.6}$$

$$D_{KCl}=\frac{2}{\frac{1}{D_{K^+}}+\frac{1}{D_{Cl^-}}} \qquad \text{Equation 3.7}$$

In the mixed NaCl and KCl solutions, the diffusion coefficients of Na^+ (0.87×10^{-9} $m^2 \cdot s^{-1}$) and K^+ (2.17×10^{-9} $m^2 \cdot s^{-1}$) are both lower than that of Cl^- (2.98×10^{-9} $m^2 \cdot s^{-1}$). The mutual diffusion coefficients for NaCl and KCl are calculated

to be 1.34 × 10^{-9} $m^2 \cdot s^{-1}$ and 2.51 × 10^{-9} $m^2 \cdot s^{-1}$, respectively. Although the difference between the diffusion coefficients of Na^+ and K^+ is slightly reduced, the selective crystallization of the two salts remains primarily governed by the difference in the diffusion coefficients of Na^+ and K^+, owing to their shared anion.

3. Effect of ion partitioning and ion exchange on Na^+/K^+ separation

Kaolinite has a lamellar structure, characterized by stacked layers of octahedral alumina and tetrahedral silica. These layers are primarily held together by van der Waals forces and strong hydrogen bonds, which limit interlayer swelling. As a result, kaolinite maintains its structural integrity under varying environmental conditions. In the ceramic membrane, the arrangement of flat kaolinite particles forms interconnected voids (Supplementary Figure 3.4), facilitating ion transport. Due to steric, dielectric, and Donnan exclusion effects, ion transport between the solution and the membrane may involve ion partitioning at the solution-membrane interfaces[7,8]. However, given the large pore size of the ceramic membrane (>30 nm), significant ion partitioning for Na^+ (ionic radius: 95 pm) and K^+ (ionic radius: 133 pm) is unlikely.

Although kaolinite exhibits some cation exchange capacity[9], its impact on ion separation is minimal. Kaolinite has two types of cation exchange sites: one resulting from the isomorphic substitution of Al^{3+} for Si^{4+} in the tetrahedral sheets, and the other located on the basal surfaces. The chemical formula

$Al_2Si_2O_5(OH)_4$ indicates limited isomorphic substitution in both the octahedral and tetrahedral sheets, which results in low surface areas and cation exchange capacities. For the ceramic membrane, the measured cation exchange capacities for Na^+ and K^+ are 0.43 and 0.45 $mg \cdot g^{-1}$, respectively. Given these low values, the kaolinite particles in the ceramic membrane become quickly saturated during the evaporation process, thus having a negligible influence on the selective crystallization process.

4. Overcoming challenges in high-purity salt extraction with the DiSC strategy:

Traditional methods such as precipitation[10], membrane filtration[7,8,11], and adsorption[12-14] have advanced ion separation but still face limitations in separation efficiency, environmental impact. For instance, chemical precipitation, commonly employed in brine treatment, is heavily dependent on the use of chemicals, leading to high chemical consumption and byproducts generation[15]. Similarly, adsorption-based methods, which are effective for recovering trace-value salts such as lithium[16,17], also require acid consumption for regeneration. In contrast, membrane separation avoids complicated regeneration process, making it more environmentally friendly, but its separation efficiency is limited by salt-induced charge screening effects at higher salinities[7,18]. While thermal processes like MVR are salinity-resistant,

they are energy-intensive[19] and primarily rely on solubility differences for separation, which limits effectiveness. Compared to traditional methods, the DiSC strategy utilizes ion diffusion coefficient disparities with a floating porous membrane, powered by sustainable energy, to achieve high-purity salt crystallization without the need for chemical additives and complex regeneration steps. More importantly, the DiSC strategy also holds significant potential for optimizing traditional thermal crystallization processes, enhancing their efficiency and precision in ion separation. Based on our latest experimental results, we successfully crystallized high-purity NaCl (>99%) salt from seawater at a higher crystallization rate of 300 $g \cdot m^{-2} \cdot h^{-1}$ and a high evaporation rate of 16 $kg \cdot m^{-2} \cdot h^{-1}$ using electric-heating driven evaporation (Supplementary 3.28). By addressing the fundamental limitations of conventional separation techniques, the DiSC strategy provides an energy-efficient, cost-effective, and environmentally sustainable solution for high-purity salt production, with broad applications in industrial brine management, resource recovery, and sustainable chemical manufacturing.

5. Membrane pore structure and pore size in COMSOL modelling:

In the COMSOL simulation, the pores were modeled as randomly distributed to reflect typical experimental conditions where the membrane's microstructure is not perfectly aligned or ordered (Supplementary Figure 3.4).

This assumption simplifies the model while still capturing the key transport phenomena. Tortuosity, which reflects the deviation of the flow path from a straight line, plays an important role in the behavior of the porous medium, particularly when considering vertical pores versus tortuous (curved or winding) pores. To simplify the model while maintaining accuracy, tortuosity was utilized by assuming that tortuous pores could be represented as effective vertical pores with adjusted parameters. As a result, a homogenized porous medium model was used, which was commonly employed in membrane simulations[20-22]. This model treats the porous medium as a homogeneous material with effective properties, avoiding the need to explicitly resolve each individual pore. This approach simplifies the simulation while still accurately representing the key transport behaviors of the system. The assumption of random pore distribution is typical in porous media modeling as it provides a more generalized and realistic representation of membrane structures under practical conditions.

Regarding the pore size distribution, incorporating a more complex distribution could offer additional insights, particularly for membrane systems characterized by highly non-uniform pore structures. However, such an approach would significantly increase the computational complexity of the model[23], leading to higher resource demands and longer simulation times. This added complexity is unlikely to provide a substantial improvement in the

accuracy of the results, as the study's primary focus lies in capturing the key transport phenomena. Furthermore, the pore size distribution in the present system is relatively narrow, which makes the detailed simulation of the distribution unnecessary. Given the uniformity of the pore sizes, employing an average pore size adequately captures the relevant transport behaviors without overcomplicating the model[8,24,25].

6. COMSOL modeling

To better demonstrate the impacts of convection minimization through pore size reduction on selective crystallization, we developed a mechanistic model by coupling fluidic flow and mass transfer in the membrane from Figure 1e. The numerical simulation was conducted using the finite element method in COMSOL Multiphysics 6.1. Due to the symmetry of the membrane in Figure 1e, a two-dimensional axisymmetric model of the membrane (Thickness:7 mm Diameter: 55 mm Porosity: 32%) was built for simulation analysis. The membrane was modeled as a homogenized porous medium for simplicity, computational efficiency, and consistency with experimental conditions. The average pore size of membranes in Figure 1d are 0.1, 10 and 100 μm, respectively. The average pore size of membranes in Figure 1d are 0.1, 10 and 100 μm, respectively. The average pore size of membranes in Figures 3.2 and 3.3 are 0.03 μm.

The flow in porous media is governed by a combination of the continuity equation and the momentum equation, which together form the *Brinkman Equations*[23]*:*

$$\nabla\cdot[-pI+K]-\left(\mu k^{-1}+\beta\rho|u|+\frac{Q_m}{\varepsilon_p^2}\right)u+F+\rho g=0 \qquad \text{Equation 3.8}$$

$$\rho\nabla\cdot u=Q_m \qquad \text{Equation 3.9}$$

where μ is the dynamic viscosity of the fluid ($kg\cdot m^{-1}\cdot s^{-1}$), u is the velocity vector ($m\cdot s^{-1}$), ρ is the density of the fluid ($kg\cdot m^{-3}$), p is the pressure (Pa), ε_p is the porosity of the porous medium, k (m^2) is the permeability of the porous medium, and Q_m is a mass source or sink ($kg\cdot m^{-3}\cdot s^{-1}$)[20,21,26].

For solute transport, we used the *Transport of Diluted Species* module, which accounted for the diffusion of solutes through the porous medium. The transport equation applied was:

$$\frac{\partial C}{\partial t}=\nabla\cdot(D\nabla C) \qquad \text{Equation 3.10}$$

where C is the solute concentration ($g\cdot L^{-1}$) and D is the diffusion coefficient ($m^2\cdot s^{-1}$).

The *Kozeny–Carman* equation was used to estimate the permeability of the membrane:

$$k=\frac{d_p^2}{180}\frac{\varepsilon_p^3}{(1-\varepsilon_p)^2} \qquad \text{Equation 3.11}$$

where d_p is the average pore size of the membrane (m).

Due to reduced solution phase volume and increased diffusion length, the effective diffusion coefficient of species i in the membrane is expressed as:

$$D_i^e = \frac{\varepsilon}{\tau} D_i \qquad \text{Equation 3.12}$$

Where D_i is the diffusive coefficient i in the bulk solution ($m^2 \cdot s^{-1}$), ε is the porosity of the membrane and τ is the tortuosity of the membrane.

As for the boundary conditions of Figure 3.1d, a fixed concentration was applied (150 $g \cdot L^{-1}$ NaCl and 150 $g \cdot L^{-1}$ KCl) at the top surface of the membrane to represent the saturation condition, which is typical for simulations of salt crystallization processes. Meanwhile, the bottom of the membrane was in contact with pure water, establishing a stable concentration gradient that drives salt transport via diffusion and convection. The temperature was maintained at 25°C. For the configurations in Figures 3.2 and 3.3, the membrane bottom was in contact with salt solutions of varying mass ratios while maintaining a constant total salinity of 40 $g \cdot L^{-1}$. The salt concentration was stabilized throughout evaporation.

7. Environmental factors affecting ion diffusion

Ion diffusion coefficients are influenced not only by intrinsic properties, such as ion size and charge, but also by various environmental factors[27-29], including temperature, solvent viscosity, and electrostatic interactions. As temperature increases, ion diffusion generally follows the Arrhenius equation,

with diffusion coefficients increasing accordingly[30]. Conversely, as solvent viscosity increases, the diffusion coefficient decreases[31]. To obtain more accurate diffusion coefficients for Na^+ and K^+ under varying environmental conditions, molecular dynamics (MD) simulations were employed. These simulations utilized the mean square displacement (MSD) method (Supplementary Figure 3.1). Under the experimental conditions shown in Figure 2d, the diffusion coefficients for Na^+ and K^+ in solution were calculated to be 0.87×10^{-9} and 2.17×10^{-9} $m^2 \cdot s^{-1}$, respectively.

8. Effect of anions on the selective crystallization:

To explore the effect of different anions on selective crystallization, we conducted evaporation experiments using a 7 mm-thick membrane in the NaCl and K_2SO_4 solution with a 1:1 mass ratio. At an evaporation rate of 0.53 $kg \cdot m^{-2} \cdot h^{-1}$ (Supplementary Figure 3.23a), XRD analysis (Supplementary Figure 27b) revealed that the formed salt crystals on the membrane surface were mainly composed of NaCl and K_2SO_4 (Supplementary Figure 3.23b). Meanwhile, the proportion of K_2SO_4 in the salt crystals increased from 50% to 65% (Supplementary Figure 3.23c), indicating the selective crystallization of K_2SO_4. In salt solution, ions diffuse as part of salt rather than individually, due to the necessity of maintaining electroneutrality. As a result, the diffusion coefficient of an individual ion can be influenced by its counterion.[3-5] Thus, the mutual

diffusion coefficient of the salt was used to consider the effect of different anions on selective crystallization. During the evaporation of a mixed NaCl and K_2SO_4 solution, four salts—NaCl, KCl, Na_2SO_4, and K_2SO_4—may crystallize on the membrane surface. The mutual diffusion coefficients of these salts are as follows: 1.68×10^{-9} $m^2 \cdot s^{-1}$ for NaCl, 1.99×10^{-9} $m^2 \cdot s^{-1}$ for KCl, 1.23×10^{-9} $m^2 \cdot s^{-1}$ for Na_2SO_4, and 1.53×10^{-9} $m^2 \cdot s^{-1}$ for K_2SO_4. While Na_2SO_4 has a lower diffusion coefficient than K_2SO_4, its higher solubility (28 g/100 g H_2O at 25°C) than K_2SO_4 (12 g/100 g H_2O at 25°C) would lead to a higher back transport flux, leading to selective crystallization of K_2SO_4. Similarly, although NaCl has a slightly higher diffusion coefficient than Na_2SO_4, the high concentration of NaCl in the bulk solution suppresses its diffusion, reducing its diffusion flux and promoting NaCl crystallization.

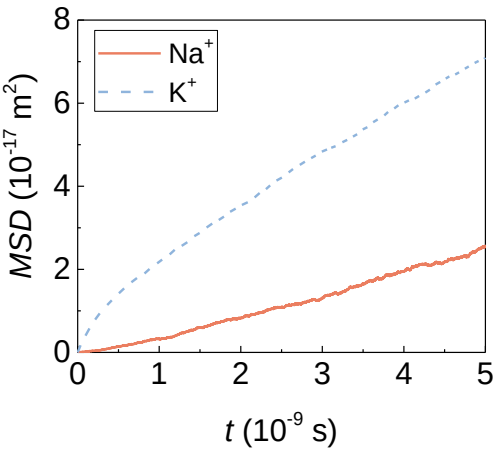

Supplementary Figure 3.1. Mean square displacement (MSD) of Na^+ and K^+ from Molecular dynamic (MD) simulation.

Mean square displacement (MSD) of Na^+ and K^+ from Molecular dynamic (MD) simulation refers to a quantitative measure of the average squared distance that Na^+ and K^+ travel over time, with the diffusion coefficients of 0.87 × 10^{-9} and 2.17 × 10^{-9} $m^2 \cdot s^{-1}$, respectively.

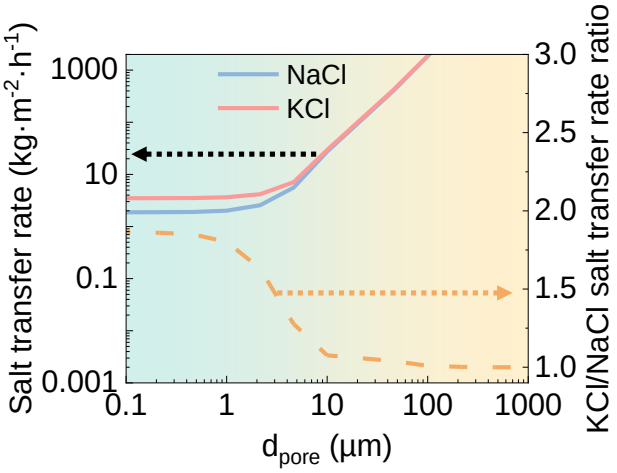

Supplementary Figure 3.2. COMSOL simulated salt transfer rate and KCl/NaCl transfer rate ratio under a stable concentration gradient as a function of membrane pore size.

As shown in Supplementary Figure 2, diffusion dominates ion transfer when the pore size is below 0.1 μm, resulting in different ion transfer rates due to the distinct diffusion coefficients of Na^+ (0.87×10^{-9} m·s^{-1}) and K^+ (2.17×10^{-9} m·s^{-1}). As the pore size decreased from 10 to 0.1 μm, the ratio of the downward transfer rates of KCl to NaCl increased from 1 to 1.86, after which the ratio remained stable.

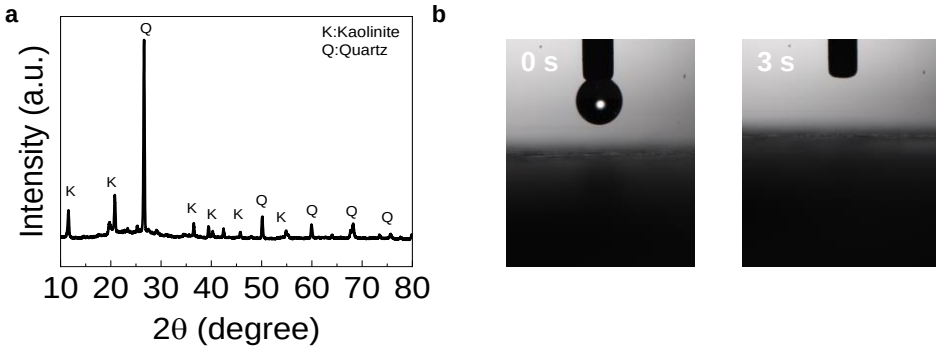

Supplementary Figure 3.3. (a) X-ray diffraction (XRD) diagram of the ceramic membrane, showing the major component of kaolinite. (b) Image of the water drop hanging above the ceramic membrane and the moment it touches the membrane surface. The ceramic membrane can absorb a water droplet upon touching it within 3 s, indicating its high hydrophilicity.

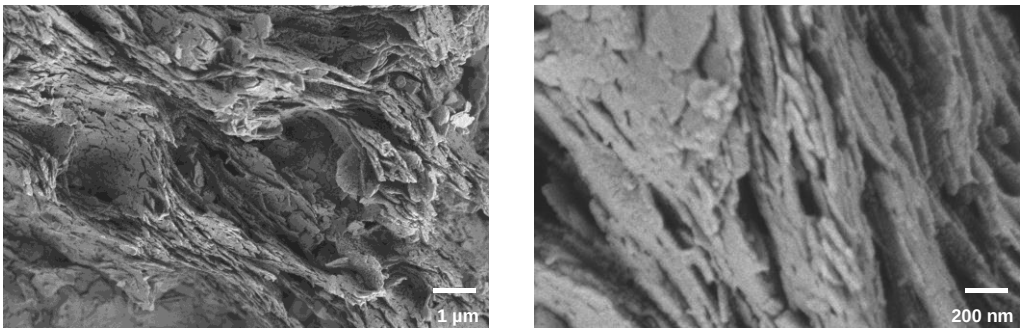

Supplementary Figure 3.4. SEM images of the ceramic membrane, showing the porous structure that enables efficient ion transfer during evaporation.

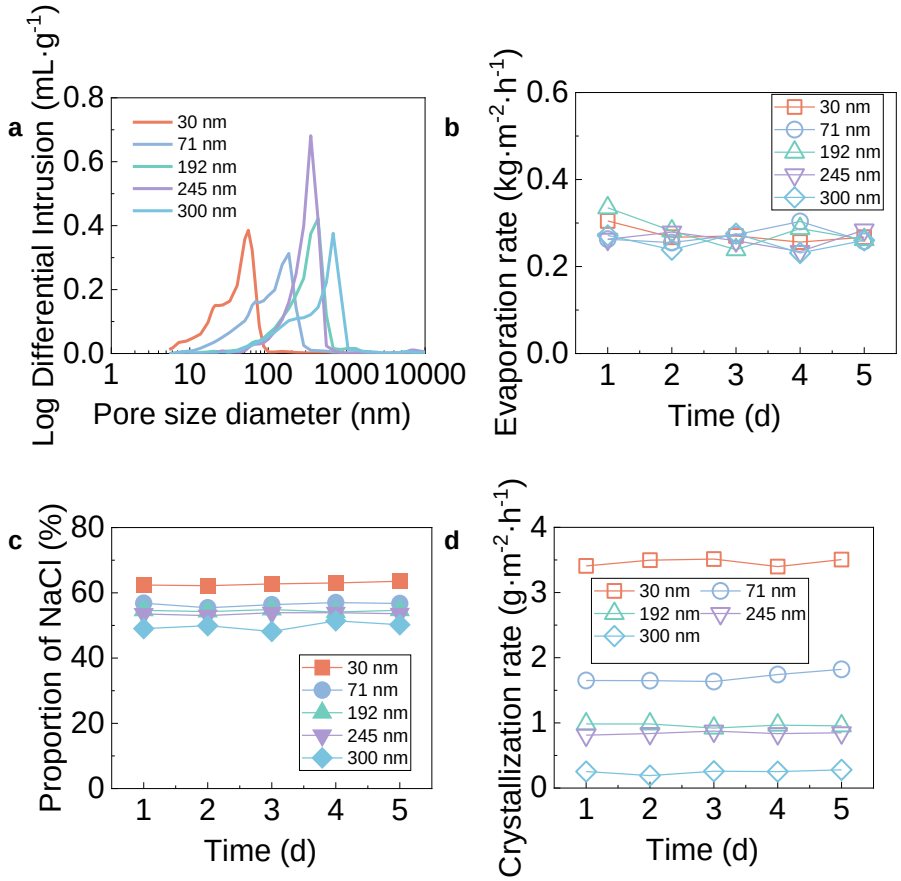

Supplementary Figure 3.5. Salt crystallization rate and the proportion of NaCl in the crystallized salts when evaporating the mixed NaCl/KCl source solution with a mass ratio of 1:1 using ceramic membrane with different pore sizes. (a) Pore size distribution of the ceramic membranes. (b) Evaporation rate of membrane with different pore sizes. (c) NaCl proportion in the crystallized salts on the surface of membrane with different pore sizes. (d) Crystallization rate of the membrane with different pore sizes. The total salt concentration was maintained at 40 g·L^{-1} and the evaporation was driven by wind at 25ºC. The same color and shape of the date dots in the Figures a, b and c represent the corresponding relationship between them.

As shown in Supplementary Figure 5d, the salt crystallization rate increased from 0.25 to 3.46 $g \cdot m^{-2} \cdot h^{-1}$ through five-day continuous measurements as the average pore size decreased from 300 to 30 nm. Notably, the purity of NaCl in the crystallized salt increased from 50% to 63% as the average pore size was decreased from 300 to 30 nm, demonstrating enhanced selectivity for Na^+ crystallization.

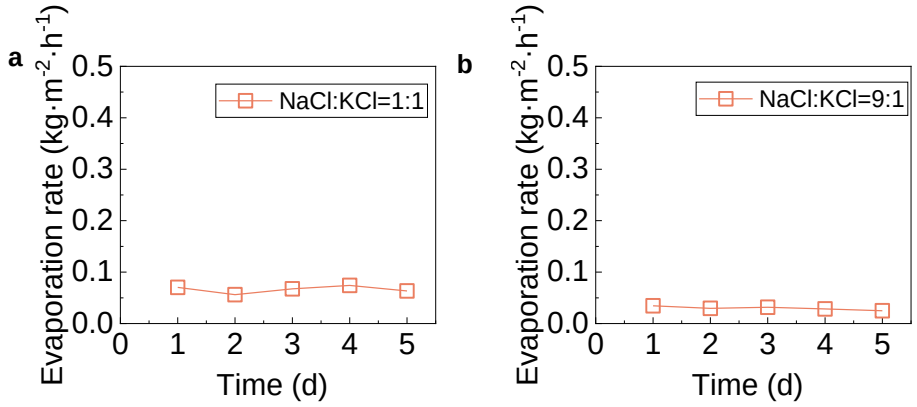

Supplementary Figure 3.6. The evaporation rates of the 7 mm-thick ceramic membrane when evaporating mixed NaCl/KCl source solution with a mass ratio of (a) 1:1 and (b) 9:1, showing an evaporation rate of 0.07 and 0.03 $kg \cdot m^{-2} \cdot h^{-1}$, respectively. The low evaporation rate resulted in both U_{K^+} and U_{Na^+} smaller than their respective $R_{max,}$ thereby preventing salt crystallization. The total salt concentration was maintained at 40 $g \cdot L^{-1}$, and the evaporation was driven by wind at 25°C.

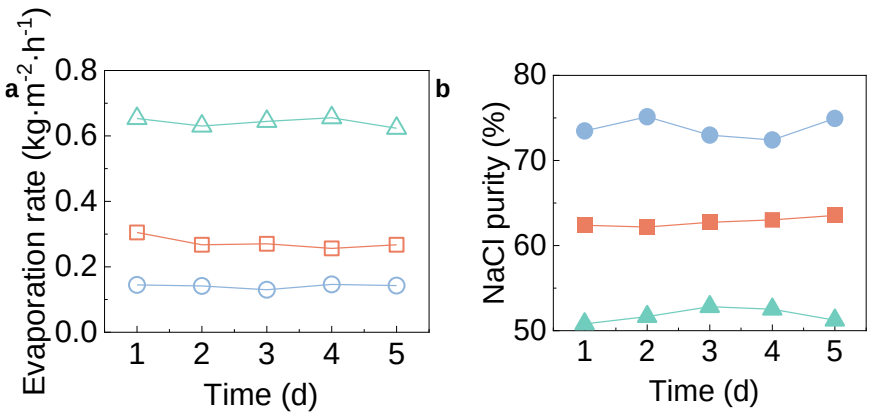

Supplementary Figure 3.7. The evaporation rate (a) and NaCl purity (b) of the 7 mm-thick ceramic membrane with a mixed NaCl/KCl source solution at a mass ratio of 1:1. The total salt concentration was maintained at 40 g·L^{-1}, and the evaporation was driven by wind at 25°C. The same color and shape of the date dots in the Figures a and b represent the corresponding relationship between them.

COMSOL simulated salt crystallization states were verified by a 7 mm-thick ceramic membrane when evaporating the mixed source solution with a mass ratio of 1:1 (Supplementary Figure 7). At an evaporation rate of 0.14 kg·m^{-2}·h^{-1}, NaCl was selectively crystallized and its purity in crystallized salts reached 74%, which corresponded to pure NaCl crystallization. The lower NaCl purity compared to the COMSOL simulation was attributed to fluctuations within the narrow range required for selective crystallization (0.13~0.16 kg·m^{-2}·h^{-1}). Upon further increasing the evaporation rate to 0.25 and 0.64 kg·m^{-2}·h^{-1}, the NaCl

purity in crystallized salts was decreased to 61% and 52%, indicating a transition from pure NaCl crystallization to mixed NaCl/KCl crystallization.

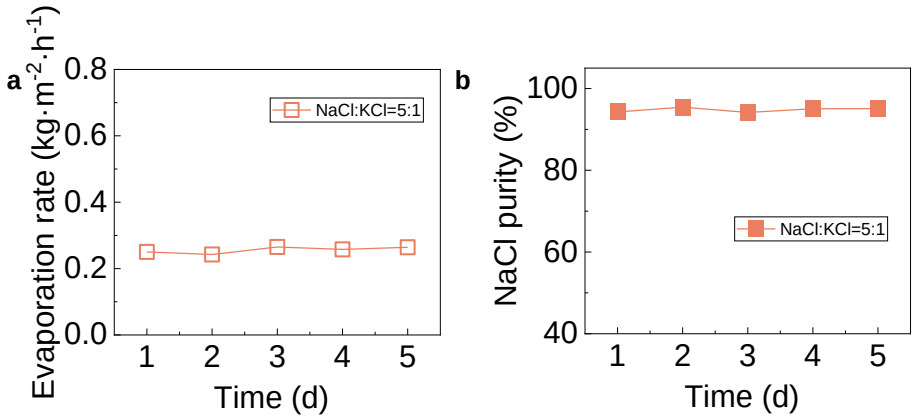

Supplementary Figure 3.8. The evaporation rate (a) and NaCl purity (b) of the 7 mm-thick ceramic membrane with a mixed NaCl/KCl source solution at a mass ratio of 5:1. The total salt concentration was maintained at 40 g·L^{-1}, and the evaporation was driven by wind at 25°C. The same color and shape of the date dots in the Figures a and b represent the corresponding relationship between them.

As shown in Supplementary Figure 3.8, COMSOL simulated salt crystallization states were verified by a 7 mm-thick ceramic membrane when evaporating the mixed source solution with a mass ratio of 5:1. 95.32% NaCl were crystallized at evaporation rates of 0.25 kg·m^{-2}·h^{-1}, corresponding to pure NaCl crystallization, as predicted by the COMSOL simulation.

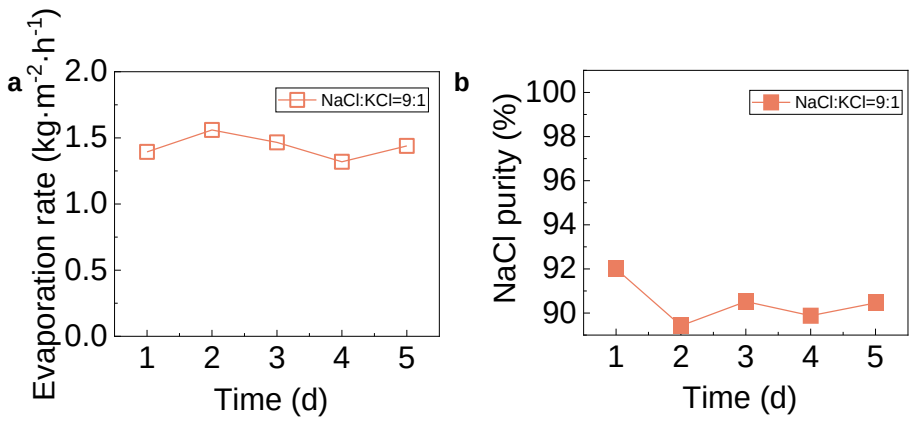

Supplementary Figure 3.9. The evaporation rate (a) and NaCl purity (b) of the 7 mm-thick ceramic membrane with a mixed NaCl/KCl source solution at a mass ratio of 9:1. The total salt concentration was maintained at 40 g·L^{-1}, and the evaporation was driven by wind at 25°C. The same color and shape of the date dots in the Figures a and b represent the corresponding relationship between them.

As shown in Supplementary Figure 3.9, COMSOL simulated salt crystallization states were verified by a 7 mm-thick ceramic membrane when evaporating the mixed source solution with a mass ratio of 9:1. Under this condition, NaCl purity in crystallized salts was 90% at an evaporation rate of 1.44 kg·m^{-2}·h^{-1}, indicating the mixed NaCl and KCl crystallization as predicted by the COMSOL simulation.

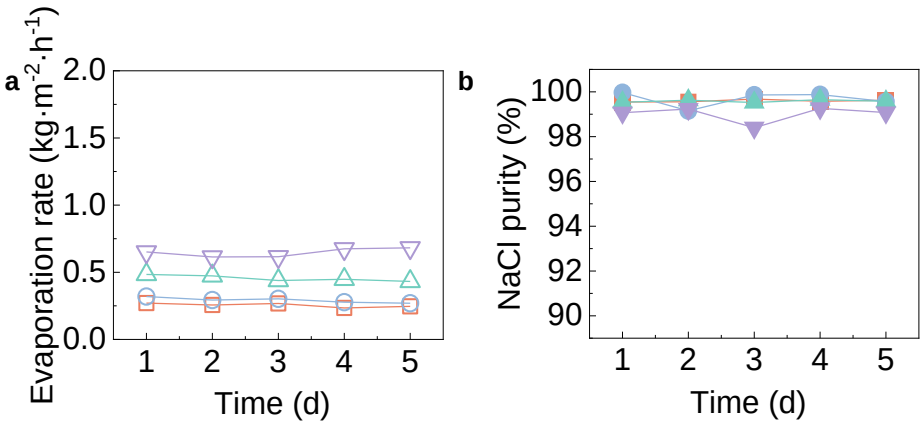

Supplementary Figure 3.10. The evaporation rate (a) and NaCl purity (b) of the 7 mm-thick ceramic membrane with a mixed NaCl/KCl source solution at a mass ratio of 9:1. The total salt concentration was maintained at 40 g·L^{-1}, and the evaporation was driven by wind at 25^{o}C. The same color and shape of the date dots in the Figures a and b represent the corresponding relationship between them.

As shown in Supplementary Figure 3.10, COMSOL simulated salt crystallization states were verified by a 7 mm-thick ceramic membrane when evaporating the mixed source solution with a mass ratio of 9:1. At an evaporation rate of 0.25 to 0.65 kg·m^{-2}·h^{-1}, NaCl purity in crystallized salts exceeded 99%, which corresponded to pure NaCl crystallization.

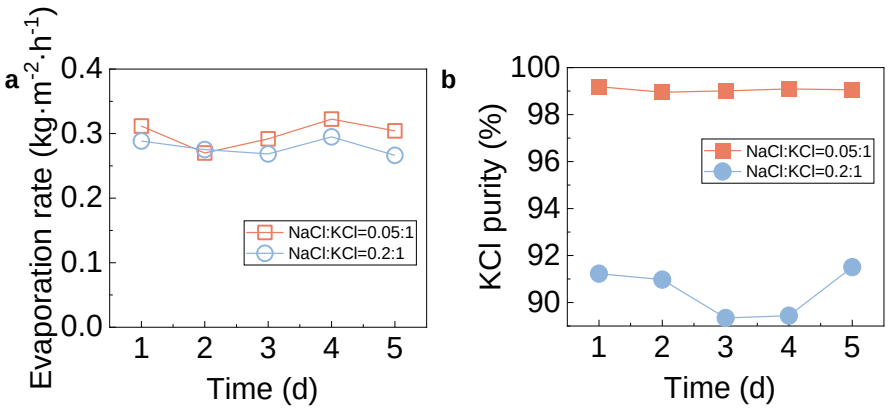

Supplementary Figure 3.11. The evaporation rate **(a)** and KCl purity **(b)** of the 7 mm-thick ceramic membrane during evaporation of mixed NaCl/KCl source solution with a mass ratio of 0.05:1 and 0.2:1. The total salt concentration was maintained at 40 g·L^{-1}, and the evaporation was driven by wind at 25°C. The same color and shape of the date dots in the Figures a and b represent the corresponding relationship between them.

As shown in Supplementary Figure 3.11, COMSOL simulated salt crystallization states were verified by a 7 mm-thick ceramic membrane when evaporating the mixed source solution with a mass ratio of 0.05:1 and 0.2:1. At an evaporation rate of 0.30 kg·m^{-2}·h^{-1}, KCl was selectively crystallized when evaporating mixed source solution with a mass ratio of 0.05:1 and its purity in crystallized salts reached 99.06%, which corresponded to pure KCl crystallization. For the mixed source solution with a NaCl/KCl mass ratio of 0.2:1, 90.50% KCl was selectively crystallized at an evaporation rate of 0.26

$kg \cdot m^{-2} \cdot h^{-1}$.

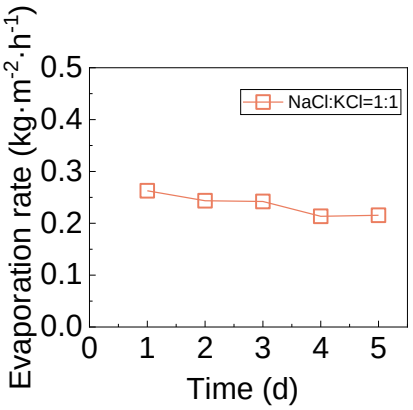

Supplementary Figure 3.12. The evaporation rate of the 3 mm-thick ceramic membrane in no salt crystallization state when evaporating mixed NaCl/KCl source solution with a mass ratio of 1:1, showing an evaporation rate of 0.24 $kg \cdot m^{-2} \cdot h^{-1}$, respectively. The low evaporation rate resulted in both U_{K^+} and U_{Na^+} smaller than their respective $R_{max,}$ thereby preventing salt crystallization. The total salt concentration was maintained at 40 $g \cdot L^{-1}$, and the evaporation was driven by wind at 25°C.

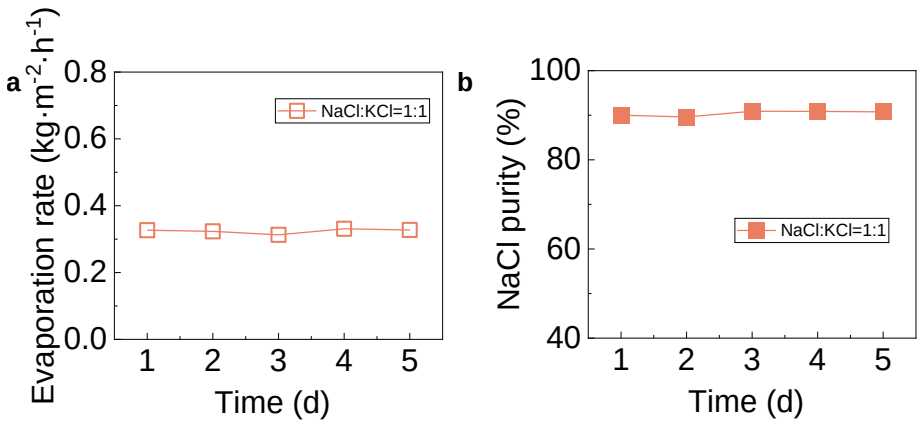

Supplementary Figure 3.13. The evaporation rate (a) and NaCl purity (b) of the 3 mm-thick ceramic membrane with a mixed NaCl/KCl source solution at a mass ratio of 1:1. The total salt concentration was maintained at 40 g·L^{-1}, and the evaporation was driven by wind at 25°C. The same color and shape of the date dots in the Figures a and b represent the corresponding relationship between them.

As shown in Supplementary Figure 3.13, COMSOL simulated salt crystallization states were verified by a 3 mm-thick ceramic membrane when evaporating the mixed source solution with a mass ratio of 1:1. 90.77% NaCl was crystallized at evaporation rates of 0.32 kg·m^{-2}·h^{-1}, corresponding to pure NaCl crystallization, as predicted by the COMSOL simulation.

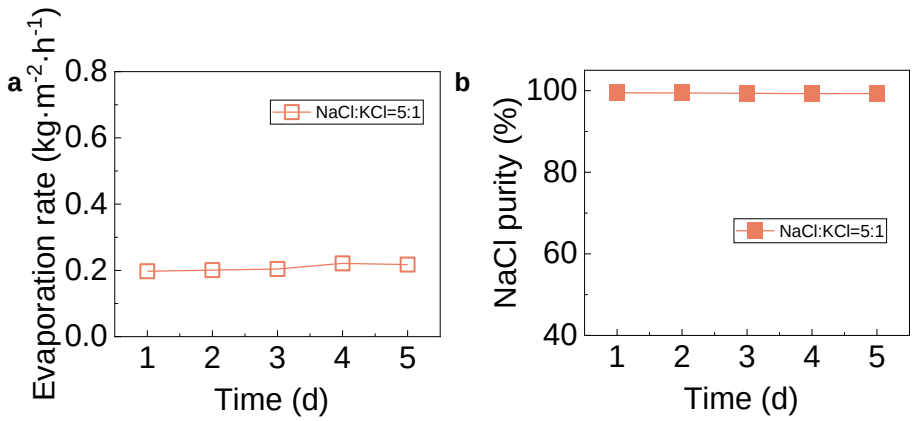

Supplementary Figure 3.14. The evaporation rate (a) and NaCl purity (b) of the 3 mm-thick ceramic membrane with a mixed NaCl/KCl source solution at a mass ratio of 5:1. The total salt concentration is maintained at 40 g·L^{-1}, and wind-driven evaporation of at 25^{o}C. The same color and shape of the date dots in the Figures a and b represent the corresponding relationship between them.

As shown in Supplementary Figure 3.14, COMSOL simulated salt crystallization states were verified by a 3 mm-thick ceramic membrane when evaporating the mixed source solution with a mass ratio of 5:1. 99.28% NaCl was crystallized at evaporation rates of 0.20 kg·m^{-2}·h^{-1}, corresponding to pure NaCl crystallization, as predicted by the COMSOL simulation.

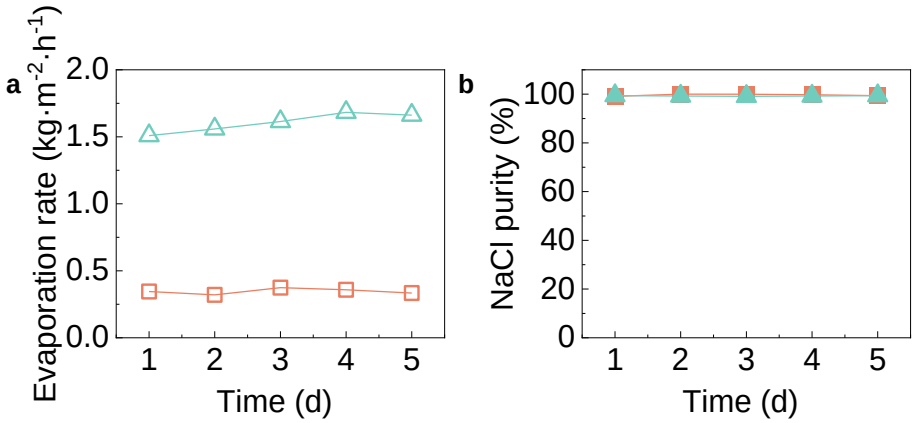

Supplementary Figure 3.15. The evaporation rate (a) and NaCl purity (b) of the 3 mm-thick ceramic membrane with a mixed NaCl/KCl source solution at a mass ratio of 9:1. The total salt concentration was maintained at 40 g·L^{-1}, and the evaporation was driven by wind at 25^{o}C. The same color and shape of the date dots in the Figures a and b represent the corresponding relationship between them.

As shown in Supplementary Figure 3.15, COMSOL simulated salt crystallization states were verified by a 3 mm-thick ceramic membrane when evaporating the mixed source solution with a mass ratio of 9:1. 99.65% and 99.28% NaCl were crystallized at evaporation rates of 0.35 and 1.61 kg·m^{-2}·h^{-1}, respectively, corresponding to pure NaCl crystallization, as predicted by the COMSOL simulation.

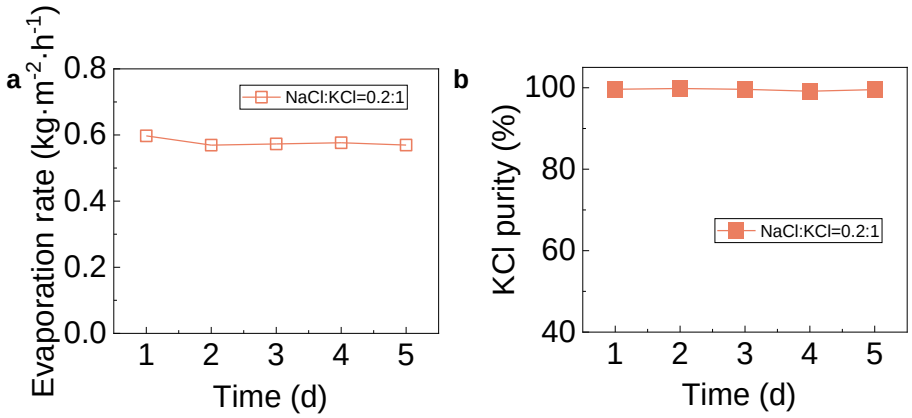

Supplementary Figure 3.16. The evaporation rate (a) and KCl purity (b) of the 3 mm-thick ceramic membrane with a mixed NaCl/KCl source solution at a mass ratio of 0.2:1. The total salt concentration was maintained at 40 g·L^{-1}, and the evaporation was driven by wind at 25°C. The same color and shape of the date dots in the Figures a and b represent the corresponding relationship between them.

As shown in Supplementary Figure 3.16, COMSOL simulated salt crystallization states were verified by a 3 mm-thick ceramic membrane when evaporating the mixed source solution with a mass ratio of 0.2:1. 99.49% KCl was crystallized at evaporation rates of 0.57 kg·m^{-2}·h^{-1}, respectively, corresponding to pure KCl crystallization, as predicted by the COMSOL simulation.

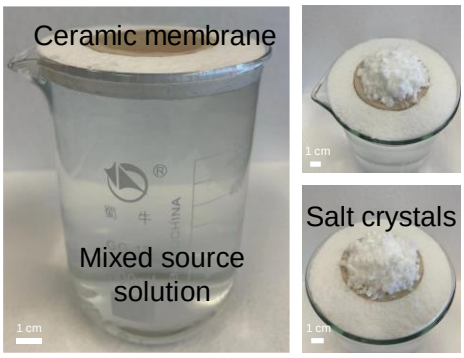

Supplementary Figure 3.17. Crystallized salt collected on the 3 mm-thick ceramic membrane through the evaporation of simulated seawater.

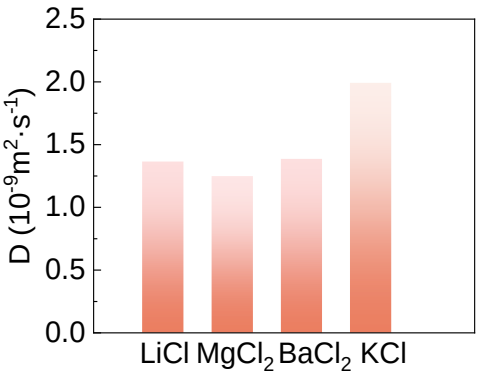

Supplementary Figure 3.18. Diffusion coefficients of Li^+, Mg^{2+}, K^+, Ba^{2+} in water (25°C).

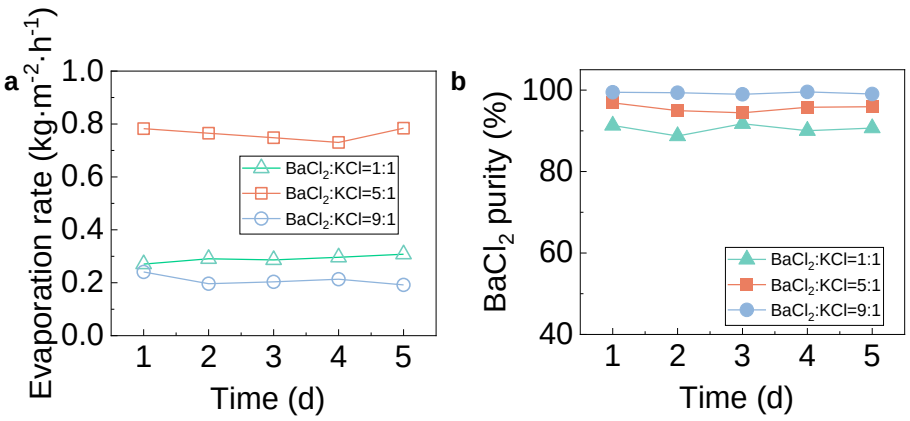

Supplementary Figure 3.19. Crystallization states of 7 mm-thick ceramic membrane during evaporation of mixed $BaCl_2$/KCl source solution with different mass ratios. (a) Evaporation rate. (b) $BaCl_2$ purity. The total salt concentration was maintained at 40 $g \cdot L^{-1}$, and the evaporation was driven by wind at 25°C. The same color and shape of the date dots in the Figures a and b represent the corresponding relationship between them.

As shown in Supplementary Figure 3.19, COMSOL simulated salt crystallization states were verified by a 7 mm-thick ceramic membrane when evaporating the mixed $BaCl_2$/LiCl source solution. The crystallized salt exhibited a $BaCl_2$ purity of 91.32% at a $BaCl_2$/KCl mass ratio of 1:1 when the evaporation rate was controlled at 0.27 $kg \cdot m^{-2} \cdot h^{-1}$. When the $BaCl_2$/KCl mass ratios were increased to 5:1 and 9:1, $BaCl_2$ crystals with purities of 95.51% and 99.20% were obtained at evaporation rates of 0.77 and 0.21 $kg \cdot m^{-2} \cdot h^{-1}$, respectively.

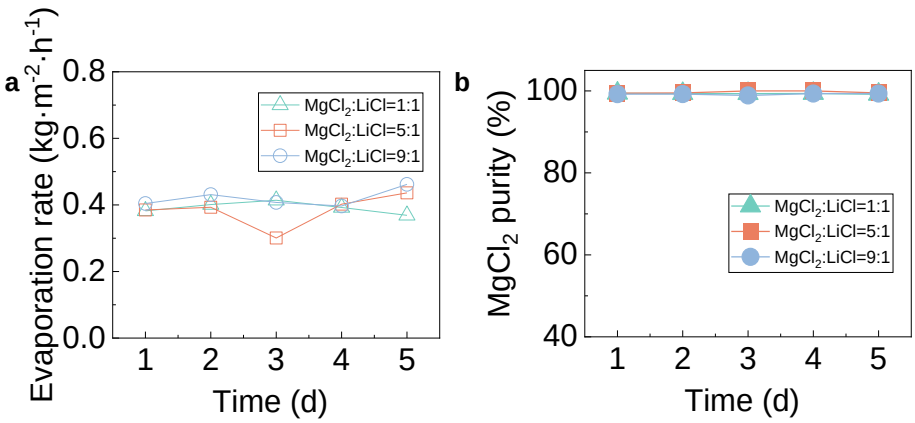

Supplementary Figure 3.20. Crystallization states of 7 mm-thick ceramic membrane during evaporation of mixed $MgCl_2$/LiCl source solution with different mass ratios. (a) Evaporation rate. (b) $MgCl_2$ purity. The total salt concentration was maintained at 80 g·L^{-1}, and the evaporation was driven by wind at 40°C. The same color and shape of the date dots in the Figures a and b represent the corresponding relationship between them.

As shown in Supplementary Figure 3.20, COMSOL simulated salt crystallization states were verified by a 7 mm-thick ceramic membrane when evaporating the mixed $MgCl_2$/LiCl source solution. When the evaporation rates were controlled at 0.40, 0.38, and 0.43 kg·m^{-2}·h^{-1}, the crystallized salts exhibited purities exceeding 99.10% for mixed source solution with $MgCl_2$/LiCl mass ratios of 1:1, 5:1, and 9:1.

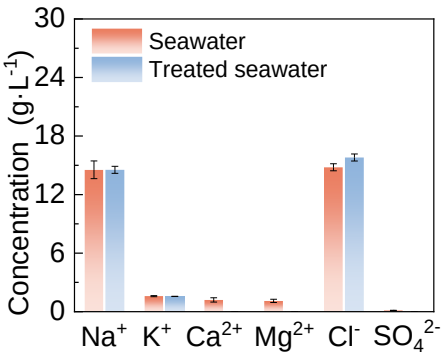

Supplementary Figure 3.21. Ion composition of the real seawater.

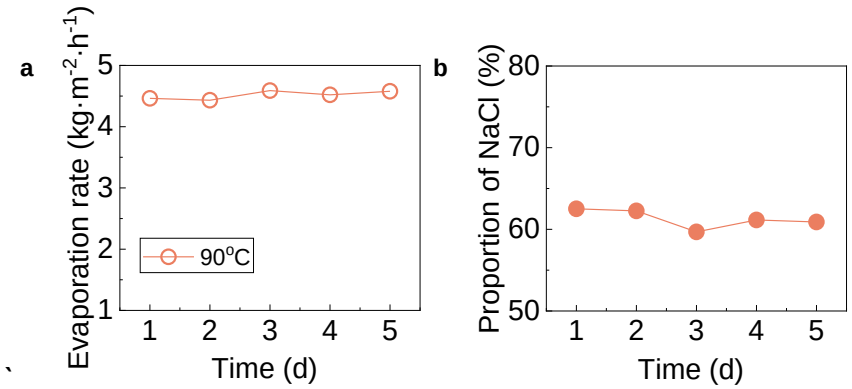

Supplementary Figure 3.22. The evaporation rate (a) and NaCl purity (b) of the 7 mm-thick ceramic membrane with a mixed NaCl/KCl source solution at a mass ratio of 1:1 at 90°C. The total salt concentration was maintained at 40 $g \cdot L^{-1}$, and the evaporation was driven by electric heating at 90°C.

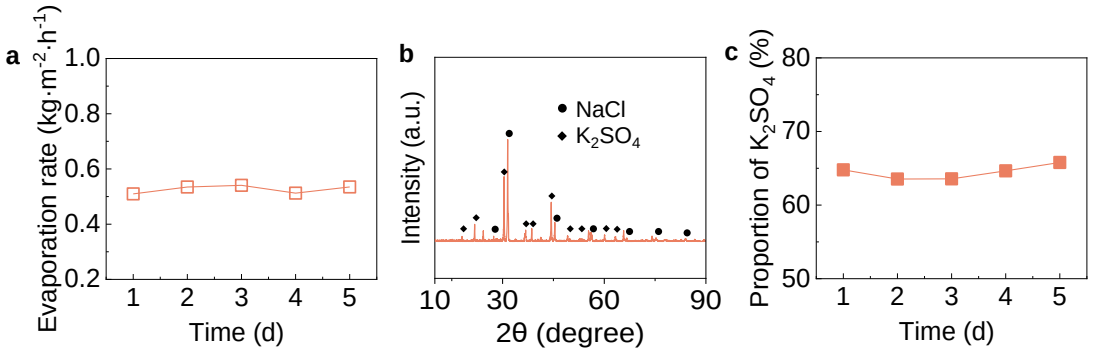

Supplementary Figure 3.23. The evaporation rate (a), salt crystal XRD pattern (b) and K_2SO_4 proportion (c) of the 7 mm-thick ceramic membrane using a mixed NaCl/K_2SO_4 source solution at a mass ratio of 1:1. The total salt concentration was maintained at 40 g·L^{-1}, and the evaporation was driven by wind at 25ºC.

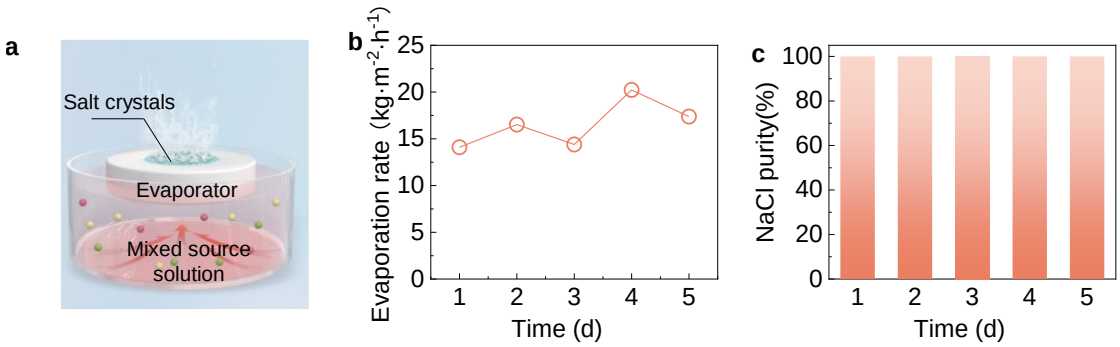

Supplementary Figure 3.24. Selective crystallization from real seawater driven by electric heating. (a) Schematic illustration of the evaporation system. (b) Evaporation rate (d) NaCl purity in the salt crystals.

Supplementary Table 3.1. The parameters of nonbonding interactions for ions used in the MD simulations.

Ions	ε (kcal·mol^{-1})	σ (nm)	q (e)
Na^+	0.02639	0.25907	1.0
K^+	0.12693	0.2999	1.0
Cl^-	0.41141	0.6437	-1.0

Supplementary Table 3.2. The concentration of NaCl and KCl in the composite system. (Unit: g·L^{-1})

Type	NaCl	KCl
Part I	0	0
Part II	150	150

Reference

1 Heiranian, M., Fan, H., Wang, L., Lu, X. & Elimelech, M. Mechanisms and models for water transport in reverse osmosis membranes: history, critical assessment, and recent developments. *Chem. Soc. Rev.* **52**, 8455–8480 (2023).

2 Nield, D. A. & Bejan, A. *Convection in Porous Media*. 5th edn, (Springer, 2017).

3 Pavluchkov, V., Shefer, I., Peer-Haim, O., Blotevogel, J. & Epsztein, R. Indications of ion dehydration in diffusion-only and pressure-driven nanofiltration. *J. Membr. Sci.* **648**, 120358 (2022).

4 Xu, R., Kang, Y., Zhang, W., Pan, B. & Zhang, X. Two-dimensional MXene membranes with biomimetic sub-nanochannels for enhanced cation sieving. *Nat. Commun.* **14**, 4907 (2023).

5 Cao, L. *et al.* Switchable Na^+ and K^+ selectivity in an amino acid functionalized 2D covalent organic framework membrane. *Nat. Commun.* **13**, 7894 (2022).

6 Cussler, E. L. *Diffusion : mass transfer in fluid systems*. 2nd edn, (Cambridge Univ. Press, 2000).

7 Epsztein, R., DuChanois, R. M., Ritt, C. L., Noy, A. & Elimelech, M. Towards single-species selectivity of membranes with subnanometre pores. *Nat. Nanotechnol.* **15**, 426–436 (2020).

8 Wang, R. & Lin, S. Pore model for nanofiltration: History, theoretical framework, key predictions, limitations, and prospects. *J. Membr. Sci.* **620** (2021).

9 Hubadillah, S. K. *et al.* Fabrications and applications of low cost ceramic membrane from kaolin: A comprehensive review. *Ceram. Int.* **44**, 4538–4560 (2018).

10 Chen, X. *et al.* Spatially separated crystallization for selective lithium extraction from saline water. *Nat. Water* **1**, 808–817 (2023).

11 Violet, C. *et al.* Designing membranes with specific binding sites for selective ion separations. *Nat. Water* **2**, 706–718 (2024).

12 Uliana, A. A. *et al.* Ion-capture electrodialysis using multifunctional adsorptive membranes. *Science* **372**, 296–299 (2021).

13 Wu, X. *et al.* Sustainable lithium extraction enabled by responsive metal-organic frameworks with ion-sieving adsorption effects. *Proc. Natl. Acad. Sci. U. S. A.* **121**, e2309852121 (2024).

14 Xia, Q. *et al.* Solar-enhanced lithium extraction with self-sustaining water recycling from salt-lake brines. *Proc. Natl. Acad. Sci. U. S. A.* **121**, e2400159121 (2024).

15 Yang, S., Wang, Y., Pan, H., He, P. & Zhou, H. Lithium extraction from low-quality brines. *Nature* **636**, 309–321 (2024).

16 Xu, X. *et al.* Extraction of lithium with functionalized lithium ion-sieves. *Prog. Mater. Sci.* **84**, 276–313 (2016).

17 Yang, S., Zhang, F., Ding, H., He, P. & Zhou, H. Lithium Metal Extraction from Seawater. *Joule* **2**, 1648–1651 (2018).

18 Violet, C. *et al.* Designing membranes with specific binding sites for selective ion separations. *Nat. Water* **2**, 706–718 (2024).

19 Zhang, C. *et al.* Designing a next generation solar crystallizer for real seawater brine treatment with zero liquid discharge. *Nat. Commun.* **12**, 998 (2021).

20 Zhang, L. *et al.* Highly efficient and salt rejecting solar evaporation via a wick-free confined water layer. *Nat. Commun.* **13**, 849 (2022).

21 Yang, H. *et al.* Tailoring the salt transport flux of solar evaporators for a highly effective salt-resistant desalination with high productivity. *ACS Nano* **16**, 2511–2520 (2022).

22 Pisani, L. Simple Expression for the Tortuosity of Porous Media. *Transp. Porous Media* **88**, 193–203 (2011).

23 Mukherjee, R., Bhunia, P. & De, S. Long term filtration modelling and scaling up of mixed matrix ultrafiltration hollow fiber membrane: a case study of chromium(VI) removal. *J. Membr. Sci.* **570-571**, 204–214 (2019).

24 Wang, R., Alghanayem, R. & Lin, S. Multipass Nanofiltration for Lithium Separation with High Selectivity and Recovery. *Environ. Sci. Technol.* (2023).

25 *Computing Porosity and Permeability in Porous Media with a Submodel*, <https://www.comsol.com/blogs/computing-porosity-and-permeability-in-porous-media-with-a-submodel>.

26 Tu, J., Yeoh, G.-H. & Liu, C. *Computational Fluid Dynamics (Third Edition)*. (Butterworth-Heinemann, 2018).

27 Koneshan, S., Rasaiah, J. C., Lynden-Bell, R. M. & Lee, S. H. Solvent Structure, Dynamics, and Ion Mobility in Aqueous Solutions at 25 °C. *J. Phys. Chem. B* **102**, 4193–4204 (1998).

28 Lee, S. H. & Rasaiah, J. C. Molecular dynamics simulation of ionic mobility. I. Alkali metal cations in water at 25 °C. *J. Phys. Chem* **101**, 6964–6974 (1994).

29 Ohtaki, H. & Radnai, T. Structure and dynamics of hydrated ions. *Chem. Rev.* **93**, 1157 – 1204 (2002).

30 Arrhenius, S. Über die Dissociationswärme und den Einfluss der Temperatur auf den Dissociationsgrad der Elektrolyte. *Zeitschrift für Physikalische Chemie* **4U**, 96–116 (1889).

31 Einstein, A. Über die von der molekularkinetischen Theorie der Wärme geforderte Bewegung von in ruhenden Flüssigkeiten suspendierten Teilchen. *Annalen der physik* **4** (1905).

4 Diffusion-driven High-Purity NaCl Production from Real Seawater via One-step Solar-Driven Crystallization

Abstract:

Solar-driven one-step high-purity NaCl production from seawater presents a persistent separation challenge due to the nearly identical physicochemical properties of NaCl and KCl. Building on DiSC strategy in Chapter 1, we developed a solar crystallizer with tailored pore size and diffusion path length to suppress non-selective ion transport. By exploiting the differences in ion diffusion, this floating evaporator enables effective separation of NaCl and KCl. Under regular solar irradiation, the crystallizer successfully achieved one-step production of NaCl with 99% purity from simulated seawater containing a NaCl/KCl mass ratio of 9:1. Beyond NaCl/KCl separation, the broad applicability of this solar crystallizer was further demonstrated by achieving 99% $BaCl_2$ and 99% $MgCl_2$ production from mixed $BaCl_2$/KCl and $MgCl_2$/LiCl system. Finally, practical application potential was proven by direct production of 99.38% NaCl with a rate of 28 $g \cdot m^{-2} \cdot d^{-1}$ without any pre- or post- treatment in just one-step. These findings underline the transformative potential of this solar-driven selective crystallization technology based on diffusion difference, which is not only simple and efficient but also economically viable for large-scale

sustainable high-purity salt production.

4.1 Introduction

Sodium is essential in biological systems and industrial applications[1-5], playing a key role in chemical manufacturing[6,7], energy storage[8,9], and medical healthcare[10,11]. As a primary source of sodium, seawater is rich in NaCl (1.4×10^{16} t), but it also contains various other salts like KCl, $MgCl_2$, and $CaSO_4$ that must be removed to obtain high-purity NaCl[12-14]. While conventional separation methods, such as chemical precipitation and membrane-based processes, effectively eliminate most impurities, NaCl/KCl separation remains a major challenge due to their highly similar physicochemical properties[2,15]. These include their similar high solubility (NaCl: 357 g·L^{-1} at 25°C, KCl: 344 g·L^{-1} at 25°C) and comparable ionic radii (Na^+: 1.02 Å, K^+: 1.38 Å in water)[2,16]. Consequently, there is a critical need for efficient NaCl/KCl separation methods that can enable the large-scale, high-purity extraction of NaCl from seawater.

Given its sustainability and simplified configuration, solar-driven interfacial evaporation crystallization technology has gained increasing prominence for the extraction of salt resources from water. However, existing salt separation processes often rely on membrane separation or solubility differences, leading to significant limitations in their ability to separate NaCl and KCl[17-19]. Notably, *Chapter 3* have highlighted that the difference in ion diffusion can drive the

selective crystallization of high-purity salts from mixed ion solutions during the interfacial evaporation process, opening up a new avenue for one-step high-purity salt production. At this point, if this strategy can be harnessed to realize a solar-driven selective crystallization process, it would not only ensure efficient resource extraction but also align with principles of sustainability—an aspect that is critically important for addressing the growing global demand for high-purity salts while minimizing environmental impact.

In this Chapter, we developed a solar crystallizer with tailored pore size and diffusion length which can effectively mitigate ion convection to utilize the difference in ion diffusion for solar-driven selective crystallization. Under regular solar radiation, this crystallizer achieved the production of NaCl crystals with a purity of 99% from simulated seawater with a NaCl/KCl mass ratio of 9:1 in one-step. Beyond NaCl/KCl, the broad applicability of the solar crystallizer was demonstrated by the successful one-step production of 99% $BaCl_2$ and 99% $MgCl_2$ from mixed $BaCl_2$/KCl and $MgCl_2$/LiCl system, respectively. To guide future application, a theoretical model was further developed to predict the salt separation capability of the solar crystallizer, with simulations showing excellent agreement with experimental results. Finally, practical application potential was showcased by the one-step production of 99.38% NaCl with a rate of 28 $g \cdot m^{-2} \cdot d^{-1}$ from real seawater under regular solar radiation without any pre- or post-treatment. These results highlight the profound economic and energy-saving

potential of this solar selective crystallization technology, positioning it as a game-changing solution for sustainable and scalable high-purity NaCl production from seawater.

4.2 Results

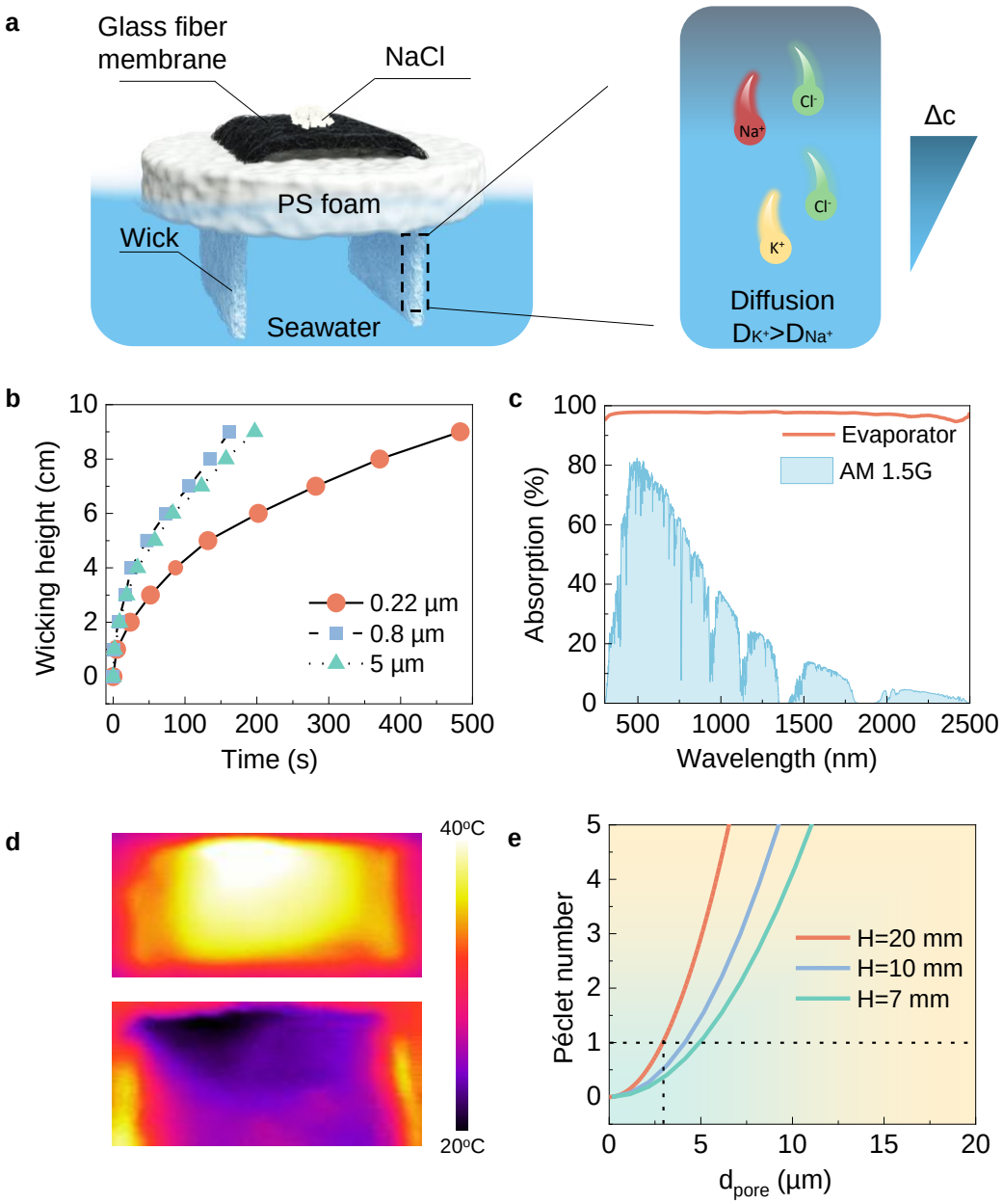

Figure 4.1 Design and fabrication of the solar crystallizer. (a) Schematic illustration of the solar crystallizer, showing a detailed view of ions diffusing back

into the bulk seawater from the evaporation interface due to the concentration gradient. (b) Anti-gravity wicking height over time of the glass fiber membrane (GFM) with different pore sizes. (c) UV-Vis-NIR spectra of the GFM coated with carbon black. (d) Infrared thermal images of the solar crystallizer floating on water both with and without one sun illumination. (e) Péclet (Pe) number of the solar crystallizer with varying GFM pore sizes and heights.

4.2.1 Design and fabrication of the solar crystallizer

To efficiently harness solar energy and drive selective salt crystallization, a solar crystallizer was specifically designed, as shown in Figure 4.1a. This system consists of a rectangular glass fiber membrane (GFM) placed on polystyrene (PS) foam, with the membrane's sides submerged in water through holes in the foam. The surface above the foam is coated with carbon black to achieve efficient sunlight-to-heat conversion. During evaporation and crystallization, ion transfer primarily occurs via capillary flow and diffusion[20,21]. When the solar crystallizer floats on the seawater, the GFM’s hydrophilic microchannels pump water with ions to the evaporation surface through capillary action. As water evaporates from the evaporation surface, ions concentrate and reach saturation. This creates a stable concentration gradient between the bulk water and the evaporation interface. Under this gradient, ions diffuse independently according to their respective diffusion coefficients.

Therefore, K^+, with a higher diffusion coefficient, diffuses back into the seawater, while Na^+, with a lower diffusion coefficient, accumulates selectively at the evaporation interface, leading to selective NaCl crystallization

To provide sufficient capillary force for water and salt transfer, a highly hydrophilic porous GFM was used. As shown in Figure 4.1b, the GFM rapidly adsorbs water droplets upon contact due to its high hydrophilicity (Supplementary Figure 4.1). The microchannels within the GFM also ensure efficient mass transfer (Supplementary Figure 4.2), with water being pumped up to 9 cm within 500 s (Figure 4.1b). To ensure solar evaporation efficiency, the GFM coated with carbon black to achieve approximately 92% solar absorption (Figure 4.1c). This allows the evaporation surface temperature to rise to 35°C under regular solar radiation (Figure 4.1d), enabling high water evaporation rate of 1.68 $kg \cdot m^{-2} \cdot h^{-1}$. In terms of ion transfer, besides diffusion, the concentration difference between the evaporation interface and the bulk solution leads to a density difference, which may in turn induces convection[20,21]. However, convection is non-selective, as it transfers ions through bulk fluid motion of the solution. To achieve selective NaCl crystallization, it is necessary to suppress this non-ion-selective transfer process, which can be guided by Péclet number (*Pe*):

$$Pe = \frac{uL}{D} \qquad \text{Equation 4.1}$$

where, u is the convection rate, L is the diffusion length and D is the ion diffusion coefficient

When Pe is below 1, ion transfer is primarily dominated by diffusion[20]. In contrast, convection would dominate ion transfer, leading to reduced selectivity. Based on Equation 4.1, either reducing the convective rate or decreasing the diffusion length can mitigate the convection effect. As shown in Figure 4.1e, narrowing the GFM pore size from 10 μm to 1 μm reduces the convective flux by increasing hydraulic resistance, which in turn lowers the Pe from 4 to below 1. This results in the suppression of convection within the crystallizer. Similarly, reducing the diffusion length can also mitigate the convection effect. For instance, when the GFM pore size is 4 μm, decreasing the diffusion length from 20 mm to 7 mm reduced Pe from 2.3 to 0.7 (Figure. 4.1e). Therefore, this designed solar crystallizer can effectively suppress non-ion-selective convection.

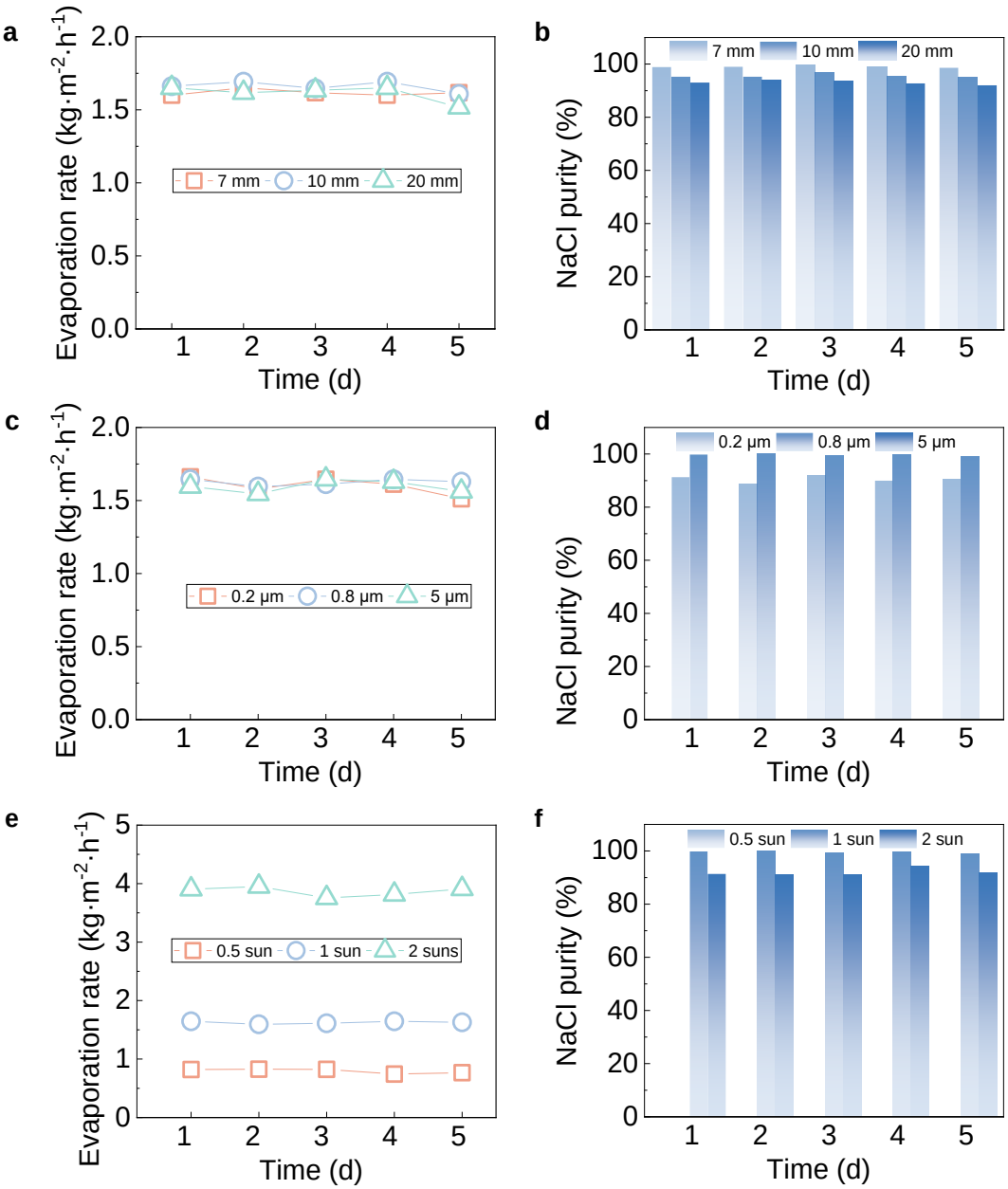

Figure 4.2. Solar-driven high-purity NaCl selective crystallization performance. Evaporation rate (a), NaCl purity (b) of simulated seawater evaporation using the solar crystallizer with 7-mm thick PS foam and different GFM pore sizes under regular solar radiation. Evaporation rate (c), NaCl purity (d) of simulated seawater evaporation using the solar crystallizer with 0.8 μm GFM and different PS foam thickness under regular solar radiation. Evaporation

rate (e), NaCl purity (f) of simulated seawater evaporation using solar crystallizer with 0.8 μm GFM and 7-mm thick PS foam under different solar intensities. The simulated seawater is prepared by mixed NaCl and KCl solution with a mass ratio 9:1 and a total salt concentration of 40 $g \cdot L^{-1}$.

4.2.2 Solar-driven high-purity NaCl crystallization performance

To evaluate NaCl/KCl separation performance, the solar crystallizer was floated on a simulated seawater (40 $g \cdot L^{-1}$ total salt, 9:1 NaCl/KCl mass ratio) under regular solar radiation (Supplementary Figure 4.3). As previously mentioned, a smaller GFM pore size can reduce convection effect and facilitate selective crystallization. When the diffusion length was fixed at 7 mm, the solar crystallizer with different GFM pore sizes showed stable evaporation of simulated seawater at an evaporation rate of 1.60 $kg \cdot m^{-2} \cdot h^{-1}$ (Figure 4.2a). However, when the GFM pore size was 5 μm, enabling convection-dominated ion transfer (Pe > 1), no salt crystallization occurred during five days of continuous testing. This is due to the strong salt rejection effect caused by the high convective rate, as previously discussed in *Chapter 3.* In contrast, when diffusion-dominated ion transfer was achieved with GFM pore sizes of 0.22 and 0.80 μm (Pe < 1), NaCl purity increased to 94.26% and 99.36%, respectively. This indicates successful solar-driven selective NaCl crystallization (Figure

4.2b).

Then the GFM with an average pore size of 0.80 μm, which produces NaCl with higher purity, was used to explore the impact of diffusion length on selective crystallization. For the solar crystallizer, reducing the pore size to 0.80 μm ensures ion transfer occurs primarily through capillary flow and diffusion. The diffusion length of the solar crystallizer can be considered to be equivalent to the PS foam thickness. Based on Fick's law, decreasing the diffusion length by reducing the PS foam thickness (*T*) amplifies the diffusion flux difference between Na^+ and K^+, increasing selectivity and NaCl purity. Under regular solar radiation, the solar crystallizer with varying PS foam thicknesses showed stable evaporation of simulated seawater at 1.61 $kg \cdot m^{-2} \cdot h^{-1}$ (Figure 4.2c). However, reducing the PS foam thickness from 20 mm to 7 mm increased NaCl purity from 93.10% to 99.05% (Figure 4.2d). Under practical operating conditions, fluctuating solar intensity affects the evaporation rate[17,22], thereby altering the capillary flow rate. As upward ion transfer is non-selective, higher evaporation rates can reduce selectivity, while lower rates may prevent crystallization[21,23]. To investigate the impact of solar intensity on the salt separation performance, different solar intensities were applied to the floating solar crystallizer. When the solar intensity was reduced from 1.0 sun to 0.5 sun, the evaporation rate decreased from 1.6 to 0.8 $kg \cdot m^{-2} \cdot h^{-1}$, resulting in no salt crystallization. In contrast, when the solar intensity was increased from 1.0 sun to 2.0 suns, the

evaporation rate rose from 1.6 to 3.9 kg·m^{-2}·h^{-1} (Figure 4.2e), but the NaCl purity decreased from 99.62% to 91.92% (Figure 4.2f). Based on these findings, a more detailed analysis of the evaporation rate's impacts on selective crystallization performance is required to ensure one-step, high-purity salt production.

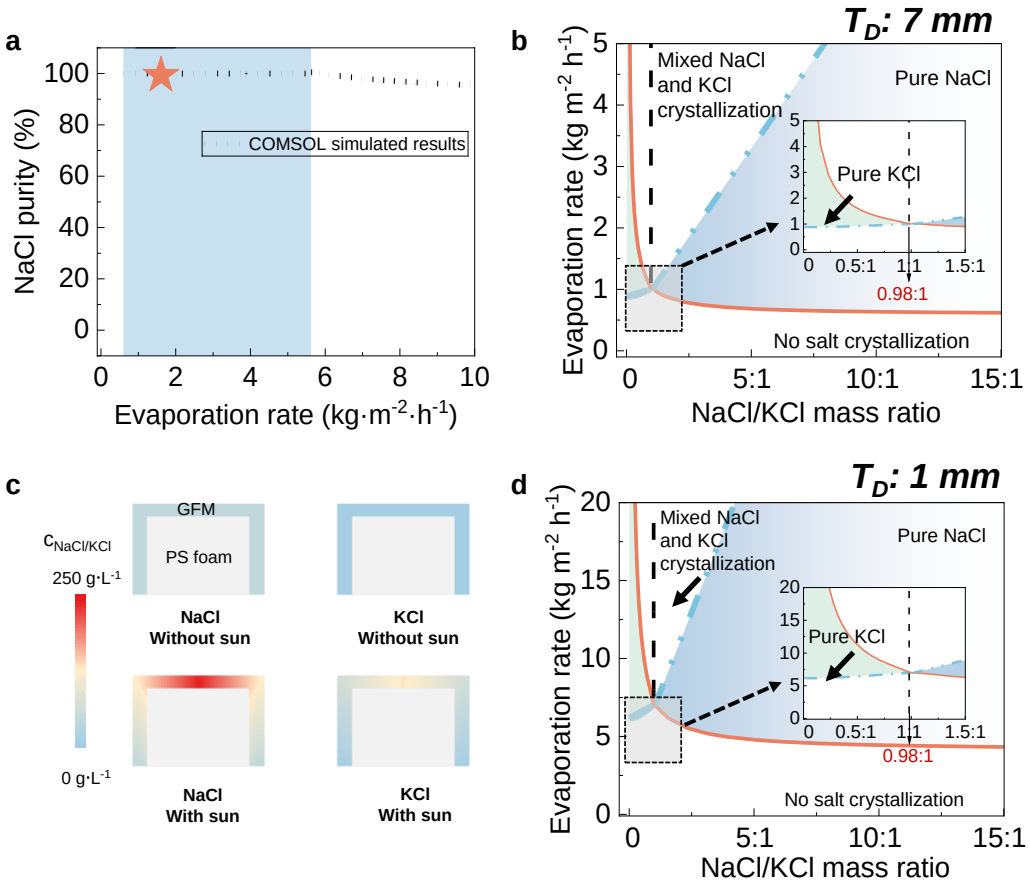

Figure 4.3. Simulated selective NaCl/KCl separation performance. (a) Evaporation range for high-purity NaCl crystallization from simulated seawater evaporation through the solar crystallizer with 7-mm-thick PS foam. The blue shaded region represents the COMSOL simulated evaporation rate for pure NaCl crystallization and the star points represent experimental evaporation rate

for pure NaCl crystallization from five-day continuous measurements. The dashed line represents simulated NaCl purity under different evaporation rates. (b) NaCl/KCl separation performance of the solar crystallizer with a 7-mm-thick PS foam during evaporation of NaCl/KCl solutions at different ratios. The four regions divided by the solid curve and dot dash curve represent COMSOL simulated different crystallization states: pure KCl, no salt crystallization, mixed salt crystallization, and pure NaCl. The inset highlights the boundary between different single salt crystallization regions. The total concentration of mixed salt source solution is maintained at 40 $g \cdot L^{-1}$. (c) Simulated concentration distribution of the solar crystallizer with a 7-mm-thick PS foam during evaporation of simulated seawater under regular radiation. (d) NaCl/KCl separation performance of the solar crystallizer with a 1-mm PS foam during evaporation of NaCl/KCl solutions at different ratios. The total salt concentration of 40 $g \cdot L^{-1}$.

4.2.3 COMOSL simulation of NaCl/KCl separation performance

In this solar crystallizer, selective crystallization is primarily governed by the competition between the capillary flow rate (U, $kg \cdot m^{-2} \cdot h^{-1}$) and the downward diffusion rate (R, $kg \cdot m^{-2} \cdot h^{-1}$) of NaCl and KCl. During solar evaporation, R reaches its maximum value (R_{max}) when the salt concentration

at the evaporation interface approaches saturation. Since salt crystal forms only when its capillary flow rate exceeds the maximum diffusion rate, salt crystallization can be categorized into four states based on the disparity of U and R_{max} of NaCl/KCl:

U can be governed by Equation 3.1[20,24]:

$$U_i = \frac{w_i}{w_{H_2O}} E_V \qquad \text{Equation 3.1}$$

where w_i and w_{H_2O} represent the mass proportion of salt i and water in the mixed source solution, and E_v is the evaporation rate (kg·m^{-2}·h^{-1}).

R can be modulated according to Fick's first law (Equation 3.2)[24,25]:

$$R_i = D_i \frac{\Delta c}{T_D} \qquad \text{Equation 3.2}$$

where D_i is the mutual diffusion coefficient (m^2·s^{-1}) of salt, Δc is the salt concentration difference (g·L^{-1}), and HH_D is the diffusion length (m).

To achieve one-step high-purity salt production, COMSOL simulations were performed to couple capillary flow and diffusion rates, guiding the selective crystallization performance of the solar crystallizer. As shown in Figure 4.3a, when evaporating simulated seawater prepared by mixing NaCl and KCl at 9:1, no salt crystallization occurs when the evaporation rate is below 0.64 kg·m^{-2}·h^{-1} (Figure 4.3a). As the evaporation rate increased to between 0.6 kg·m^{-2}·h^{-1} and 5.6 kg·m^{-2}·h^{-1}, pure NaCl is continuously crystallized due to the lower

diffusion coefficient of Na^+, which was consistent with the experimental observation of 99% NaCl crystallization at an evaporation rate of 1.6 $kg \cdot m^{-2} \cdot h^{-1}$. However, when the evaporation rate exceeded 5.6 $kg \cdot m^{-2} \cdot h^{-1}$, NaCl purity declined due to the co-crystallization of KCl.

In addition to Na^+/K^+ separation in seawater, Na^+ and K^+ are also commonly found in salt lakes and waste brines. To further assess its potential for resource extraction from these diverse water sources, we simulated the selective crystallization process using mixed NaCl/KCl solutions with varying mass ratios. The results of the COMSOL simulation are presented in Figure 4.3b, where distinct crystallization behaviors are observed in different regions. At a diffusion length of 7 mm, no salt crystallization occurred at low evaporation rates. However, when the evaporation rate slightly increased, crystallization occurred, selectively yielding either pure NaCl or pure KCl crystals, depending on the NaCl/KCl mass ratio in the source solution (Figure 4.3b). Specifically, when the NaCl/KCl mass ratio exceeded 0.98:1, pure NaCl was selectively crystallized. Conversely, when the ratio was below 0.98:1, pure KCl crystallized due to the higher concentration of K^+ in the solution. As the evaporation rate was further increased, both NaCl and KCl reached saturation at the evaporation surface (Figure 4.3c), leading to the co-crystallization of both salts (Figure 4.3d). Through simulations, selective crystallization of pure NaCl and KCl can be achieved by controlling the evaporation rate for mixed NaCl/KCl solutions.

Additionally, reducing the diffusion length enhances selective crystallization performance by enabling high-purity salt crystallization across a broader evaporation rate range and at a higher crystallization rate. As shown in Figure 4.3d, the 1 mm-thick solar crystallizer enables selective crystallization over a wider evaporation rate range (4.5~39.3 kg·m^{-2}·h^{-1}) compared to the 7 mm-thick solar crystallizer in Figure 4.3b.

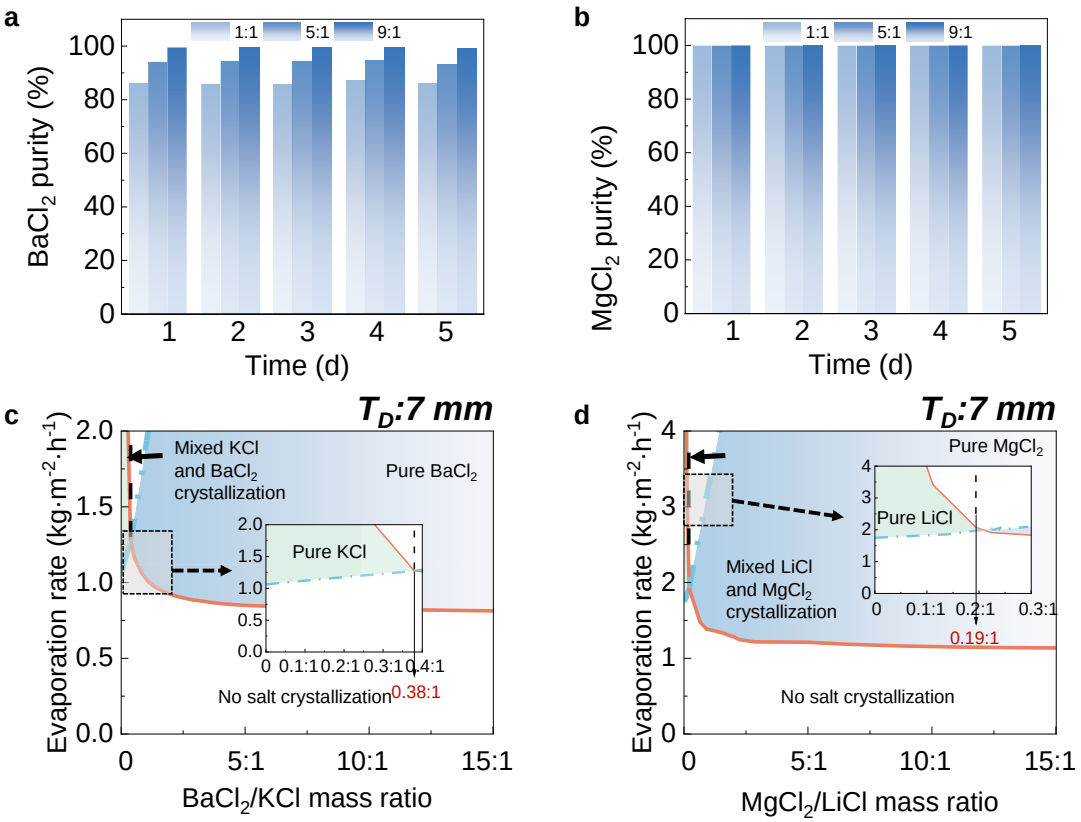

Figure 4.4. Versality of one-step high-purity salt crystallization. Crystallized $BaCl_2$ purity **(a)** of the solar crystallizer with a 7-mm-thick PS foam during evaporation of mixed KCl/$BaCl_2$ solutions at different ratios under regular solar radiation. Crystallized $MgCl_2$ purity **(b)** of the solar crystallizer with a 7-mm-thick

PS foam during evaporation of mixed LiCl/$MgCl_2$ solutions at different ratios under four-sun radiation. (**c**) KCl/$BaCl_2$ separation performance of the solar crystallizer with a 7-mm-thick PS foam during evaporation of KCl/$BaCl_2$ solutions at different ratios. The four regions divided by the solid curve and dot dash curve represent COMSOL simulated different crystallization states: pure KCl, no salt crystallization, mixed salt crystallization, and pure $BaCl_2$. The inset highlights the boundary between different single salt crystallization regions. The total concentration of mixed salt source solution is maintained at 40 $g \cdot L^{-1}$. (**d**) LiCl/$MgCl_2$ separation performance of the solar crystallizer with a 7-mm-thick PS foam during evaporation of LiCl/$MgCl_2$ solutions at different ratios. The four regions divided by the solid curve and dot dash curve represent COMSOL simulated different crystallization states: pure LiCl, no salt crystallization, mixed salt crystallization, and pure $MgCl_2$. The inset highlights the boundary between different single salt crystallization regions. The total concentration of mixed salt source solution is maintained at 40 $g \cdot L^{-1}$.

4.2.4 Broad applicability of high-purity salt crystallization

In addition to NaCl/KCl separation, the solar crystallizer can also be applied to separate other mixed salts based on differences in their ion diffusion coefficients. To demonstrate its versatility, the 7-mm-thick solar crystallizer with a GFM averaging 0.8 μm pore size was used for $BaCl_2$/KCl and $MgCl_2$/LiCl

separations, where these salts have similar solubility but different diffusion coefficients[26,27]. During the solar evaporation of $BaCl_2$/KCl mixed solutions, Ba^{2+}, with a lower diffusion coefficient (0.85×10^{-9} $m^2 \cdot s^{-1}$) compared to K^+ (2.17×10^{-9} $m^2 \cdot s^{-1}$), selectively crystallized as high-purity $BaCl_2$. Experimental results showed that 86.31%, 94.13%, and 99.48% $BaCl_2$ selectively crystallized from mixed $BaCl_2$/KCl with a mass ration of 1:1, 5:1, and 9:1, respectively. Similarly, due to the lower diffusion coefficient of Mg^{2+} (0.71×10^{-9} $m^2 \cdot s^{-1}$ for Mg^{2+} versus 1.03×10^{-9} $m^2 \cdot s^{-1}$ for Li^+), high-purity $MgCl_2$ was selectively crystallized during the solar evaporation of $MgCl_2$/LiCl mixed solutions. Due to the higher solubility of $MgCl_2$/LiCl, the solar intensity was increased to four suns to enable salt crystallization from mixed $MgCl_2$/LiCl solution. As shown in Figure 4.4b, pure $MgCl_2$ salt continuously crystallized from the surface of the solar crystallizer under a high evaporation rate of 4.0 $kg \cdot m^{-2} \cdot h^{-1}$ for the mixed $MgCl_2$/LiCl solution with a mass ratio of 1:1, 5:1 and 9:1 (Supplementary Figure 4.4). Meanwhile, COMSOL simulations were also conducted to achieve precise selective crystallization. For $BaCl_2$/KCl mixed solutions, high-purity $BaCl_2$ is selectively crystallized when the $BaCl_2$/KCl mass ratio exceeds 0.38:1 and the evaporation rate surpass approximately 0.8 $kg \cdot m^{-2} \cdot h^{-1}$ (Pure $BaCl_2$ region in Figure 4.4c). Similarly, high-purity $MgCl_2$ is selectively crystallized when the $MgCl_2$/LiCl mass ratio exceeds 0.19:1 and the evaporation rate exceed approximately 1.0 $kg \cdot m^{-2} \cdot h^{-1}$ (Pure $MgCl_2$ region in Figure 4.4d).

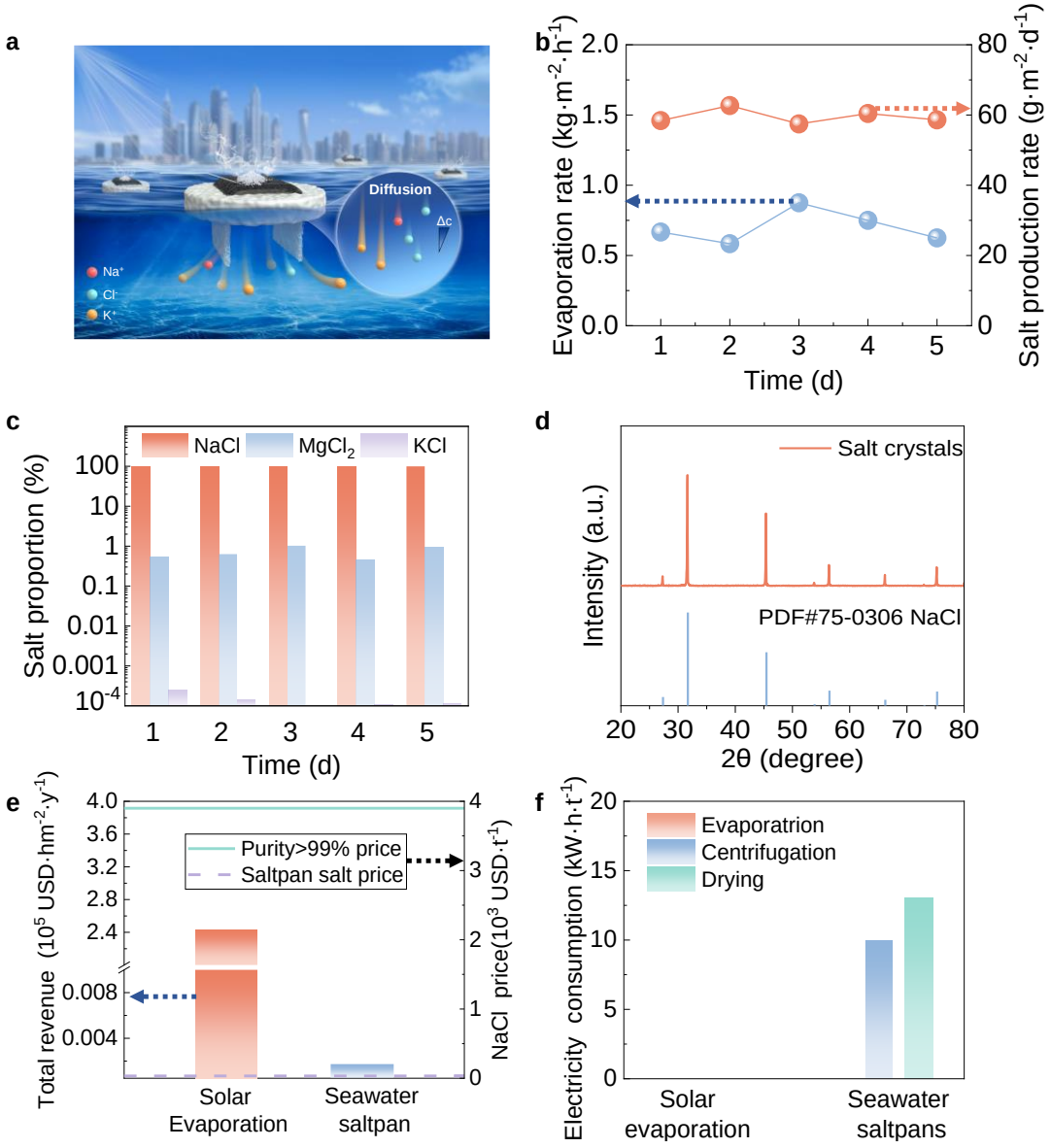

Figure 4.5. High-purity NaCl selective crystallization from real seawater. (a) Schematic illustration of high-purity NaCl selective crystallization from real seawater. (b) Evaporation rate and salt production rate of the solar crystallizer with 7-mm-thick PS foam for real seawater evaporation under regular solar radiation. (c) Proportion of the crystallized salts on the evaporator. (d) XRD patterns of the crystallized salt. (e) Total revenues and NaCl price of the crystallized NaCl from the solar crystallizer and from seawater saltpans. (f)

Electricity consumption for 99% NaCl production by the solar crystallizer and by the seawater saltpans.

4.2.5 One-step high-purity NaCl production from real seawater

To demonstrate the practical application potential, the solar crystallizer is floated on real seawater for solar-driven one-step high-purity NaCl production (Figure 4.5a and Supplementary Figures 4.5 and 4.6). Under regular solar radiation, a stable evaporation rate at 1.5 $kg \cdot m^{-2} \cdot h^{-1}$ was maintained throughout the five-day measurements (Figure 4.5b). More importantly, NaCl with a purity of 99.38% was obtained at a stable production rate of 28.0 $g \cdot m^{-2} \cdot d^{-1}$ (Figures 4.5b and 4.5c), which is two times higher than conventional seawater saltpans. These results demonstrate that high-purity salt can be directly obtained from real seawater by the solar crystallizer without any pre- or post-treatment in just one-step.

Since the market value of NaCl increases significantly with purity, the solar evaporator generates revenues of 2.49×10^5 $USD \cdot hm^{-2} \cdot y^{-1}$ by achieving higher purity NaCl, which is nearly 120 times higher than the 1.97×10^3 $USD \cdot hm^{-2} \cdot y^{-1}$ of traditional seawater saltpans (Figure 4.5e). Meanwhile, the solar crystallizer significantly reduces energy consumption compared to traditional seawater saltpans, saving a total of 23 kWh per ton of NaCl by eliminating both salt

washing and drying steps (Figure 4.5f). These improvements in both economic returns and energy consumption highlight the promising application prospects of the solar crystallizer.

4.3 Discussion

4.3.1 Constraining pore size to reduce convection rate in the GFM

The small pore size of the membrane limits convection flow by increasing the resistance to fluid movement. This resistance is quantified by the Carman–Kozeny (*C*–*K*) equation, which expresses permeability (k) as a measure of how easily fluid flows through the membrane[28]:

$$k = \frac{\varepsilon^3 d_p^2}{150(1-\epsilon)^2} \qquad \text{Equation 4.2}$$

Where ε is the porosity of the membrane, d_p is the pore diameter of the membrane.

As the pore size and porosity decrease, the membrane permeability reduces, indicating a corresponding increase in resistance to convection flow. During solar evaporation, convection in the solar crystallizer is driven by the density difference between the evaporation surface and bulk water[20,21]. The convection rate (u) can thus be described by Darcy's law[28]:

$$u = \frac{kg\Delta\rho}{\mu} \qquad \text{Equation 4.3}$$

Where ε is the porosity of the membrane, d_p is the pore diameter of the membrane.

As the pore size decreases, the resistance to convection increases significantly, resulting in a reduced convection rate.

4.3.2 High energy efficiency of the solar crystallizer during solar evaporation

In the solar crystallizer, the carbon black is used as photothermal conversion material to enable 90% sunlight adsorption. Meanwhile, the PS foam, with a low thermal conductivity[20,29] (<0.03 $W \cdot m^{-1} \cdot K^{-1}$), minimizes thermal conduction loss from the evaporation surface to the mixed source solution, thereby enhancing solar energy utilization efficiency. As a result, the evaporation rate of solar crystallizer reached 1.63 $kg \cdot m^{-2} \cdot h^{-1}$ during solar evaporation of pure water, corresponding to a solar-to-vapor conversion efficiency of approximately 91.27% under one sun irradiation (1 $kW \cdot m^{-2}$) (Supplementary Text 4.2). This high energy efficiency enables a higher salt production rate compared to conventional seawater saltpans.

4.3.3 Strategies to further increase salt purity of selective crystallization

Although the purity of the selectively crystallized salt exceeded 99% in our tests, the theoretical maximum purity of this selective crystallization strategy is 100%, according to simulation results. The non-ideal purity can be attributed to the wetting of the crystallized salt by the mixed salt source solution, caused by capillary forces generated by the accumulated pores between the crystallized

salt particles[30]. To achieve ideal purity, future research should focus on controlling the morphology of salt crystals, such as through the addition of modifiers to reduce the formation of accumulated pores[31,32]. Additionally, variations in evaporation rate can reduce salt purity due to the narrow evaporation rate range required for pure NaCl crystallization (0.7~0.9 $kg \cdot m^{-2} \cdot h^{-1}$ for mixed NaCl/KCl solutions with a mass ratio of 1:1 using a 7-mm thick solar crystallizer). However, when the mass ratio increases to 9:1, the evaporation rate range becomes broader (0.4~4.9 $kg \cdot m^{-2} \cdot h^{-1}$). Therefore, multistep evaporation can be employed to produce high-purity NaCl.

4.3.4 Simultaneous removal of other ions during solar evaporation of real seawater

In addition to Na^+/K^+, real seawater contains other ions, such as Mg^{2+} and SO_4^{2-}. During solar evaporation, the purity of NaCl exceeded 99%, indicating the effective removal of other ions. The diffusion coefficient of SO_4^{2-} is lower than that of Cl^- (1.07×10^{-9} $m^2 \cdot s^{-1}$ for SO_4^{2-} versus 2.03×10^{-9} $m^2 \cdot s^{-1}$ for Cl^-), and the diffusion coefficient of Mg^{2+} is lower than that of Na^+ (0.69×10^{-9} $m^2 \cdot s^{-1}$ for Mg^{2+} versus 1.33×10^{-9} $m^2 \cdot s^{-1}$ for Na^+). However, due to their lower concentrations, these ions do not reach saturation, preventing the formation of their respective salts (e.g., $MgSO_4$)[23]. As a result, NaCl crystallizes preferentially, achieving high purity, while the other ions remain in solution. This selective crystallization mechanism demonstrates the efficiency of solar

evaporation in separating NaCl from complex seawater mixtures.

4.3.5 Potential application scenarios of the solar crystallizer

The solar crystallizer system is designed to float directly on the seawater surface, eliminating the need for additional land area to harvest high-purity NaCl crystals. This innovative approach not only minimizes the spatial footprint but also maximizes resource utilization by harnessing natural solar energy for evaporation and crystallization. In addition to seawater, this system can also be applied to salt lakes[18,33], enabling efficient resource recovery from various saline water sources. By leveraging the solar crystallizer's selective crystallization properties, the system provides a sustainable and scalable solution for salt production and resource extraction, making it highly versatile for both coastal and inland applications.

4.4 Conclusion

This Chapter presents an innovative solar-driven one-step selective crystallization of high-purity NaCl from seawater by exploiting the intrinsic disparity in ion diffusion coefficients between Na^+ and K^+. The development of the solar crystallizer, with its ion separation efficiency and scalable design, marks a significant advancement in sustainable resource extraction. This work paves the way for energy-efficient, economically viable, and environmentally sustainable technologies for high-purity mineral extraction, offering a transformative solution to global resource challenges.

4.5 Methods

4.5.1 Mechanistic mode development for solar crystallizer

To design the selective crystallization system and simulate salt crystallization states, we developed a mechanistic model by coupling fluid flow and ion transfer within the solar crystallizer. The numerical simulation was performed using the finite element method in COMSOL Multiphysics 6.1, which integrates laminar flow and ion transport into a time-dependent solver[20,34]. Due to the symmetry of the evaporator in Figure 4.1a, a two-dimensional axisymmetric mode was built for simulation analysis. Ion transfer in the evaporator is governed by a combination of the continuity equation and the momentum equation, which are described by the Brinkman equations[28]. More detailed descriptions of simulation setup, parameter selection, and underlying assumptions can be seen in Supplementary Texts 3.1.

4.5.2 Evaporator setup for selective crystallization demonstration

For the solar crystallizer in Figure 4, a GFM was cut into a rectangular shape with its size of 9 × 3 cm^2. Two narrow slots, each 3 × 0.5 cm^2 in size and separated by a 2 cm gap, were cut in the PS foam, and the glass fiber membrane was threaded through them to ensure both membrane ends aligned. To measure selective crystallization, crystallized salts were collected from the evaporator and dissolved in DI water. Then the water samples were diluted properly and measured by ICP-OES (720 ICP-OES, Agilent) and ion

chromatography (CIC-D100, SHINE) to determine ion composition.

4.5.3 Real seawater for high-purity NaCl production

Seawater was collected from Baisha Bay, Shenzhen (114°30’ E, 22°39’ N) on May 2, 2023. The detailed ion compositions of the seawater samples are provided (Supplementary Figure 4.5). To achieve high-purity NaCl production, the solar evaporator was directly floated on the surface of the seawater sample and a solar simulator (LED AAA, Lisign Technology) equipped with an AM 1.5G filter was used to provide solar radiation with a constant intensity of 1000 $W \cdot m^{-2}$.

4.5.4 Characterizations

The surface morphology of membranes was characterized by field-emission scanning electron microscopy (SEM, TESCAN VEGA 3). The porosity and pore size distribution of membranes were measured by a mercury porosimeter (AutoPore V, Micromeritics). The WCA of membranes was determined by the CA meter (OCA20, DataPhysics). The UV-Vis-NIR diffuse reflectance spectra were recorded by an Agilent Cary 5000 spectrometer.

Reference

1 Abraham, J. *et al.* Tunable sieving of ions using graphene oxide membranes. *Nat. Nanotechnol.* **12**, 546–550 (2017).

2 Cao, L. *et al.* Switchable Na^+ and K^+ selectivity in an amino acid functionalized 2D covalent organic framework membrane. *Nat. Commun.* **13**, 7894 (2022).

3 Su, S. *et al.* Multifunctional graphene heterogeneous nanochannel with voltage-tunable ion selectivity. *Nat Commun* **13**, 4894 (2022).

4 Xin, W. *et al.* Biomimetic KcsA channels with ultra-selective K^+ transport for monovalent ion sieving. *Nat. Commun.* **13**, 1701 (2022).

5 Xu, R., Kang, Y., Zhang, W., Pan, B. & Zhang, X. Two-dimensional MXene membranes with biomimetic sub-nanochannels for enhanced cation sieving. *Nat. Commun.* **14**, 4907 (2023).

6 Tong, W. *et al.* Electrolysis of low-grade and saline surface water. *Nat. Energy* **5**, 367–377 (2020).

7 Liu, T. *et al.* In-situ direct seawater electrolysis using floating platform in ocean with uncontrollable wave motion. *Nat. Commun.* **15**, 5305 (2024).

8 Lu, Y., Li, L., Zhang, Q., Niu, Z. & Chen, J. Electrolyte and Interface Engineering for Solid-State Sodium Batteries. *Joule* **2**, 1747–1770 (2018).

9 Yao, A., Benson, S. M. & Chueh, W. C. Critically assessing sodium-ion technology roadmaps and scenarios for techno-economic competitiveness against lithium-ion batteries. *Nat. Energy* (2025).

10 Kellum, J. A. Abnormal saline and the history of intravenous fluids. *Nat. Rev. Nephrol.* **14**, 358–360 (2018).

11 Awad, S., Allison, S. P. & Lobo, D. N. The history of 0.9% saline. *Clin. Nutr.* **27**, 179–188 (2008).

12 Wu, L. *et al.* Highly efficient three-dimensional solar evaporator for high

salinity desalination by localized crystallization. *Nat. Commun.* **11**, 521 (2020).

13 Li, L. *et al.* Gradient engineering in interfacial evaporation for water, energy, and mineral harvesting. *Energy Environ. Sci.* (2025).

14 Xia, Y. *et al.* Spatially isolating salt crystallisation from water evaporation for continuous solar steam generation and salt harvesting. *Energy Environ. Sci.* **12**, 1840–1847 (2019).

15 Zhao, W. *et al.* Two-dimensional monolayer salt nanostructures can spontaneously aggregate rather than dissolve in dilute aqueous solutions. *Nat. Commun.* **12** (2021).

16 Epsztein, R., DuChanois, R. M., Ritt, C. L., Noy, A. & Elimelech, M. Towards single-species selectivity of membranes with subnanometre pores. *Nat. Nanotechnol.* **15**, 426–436 (2020).

17 Zhang, S. *et al.* Solar-driven membrane separation for direct lithium extraction from artificial salt-lake brine. *Nat. Commun.* **15**, 238 (2024).

18 Song, Y. *et al.* Solar transpiration–powered lithium extraction and storage. *Science* **385**, 1444–1449 (2024).

19 Zhang, G. *et al.* Spontaneous lithium extraction and enrichment from brine with net energy output driven by counter-ion gradients. *Nat. Water* **2**, 1091–1101 (2024).

20 Zhang, L. *et al.* Highly efficient and salt rejecting solar evaporation via a wick-free confined water layer. *Nat. Commun.* **13**, 849 (2022).

21 Zhang, L. *et al.* Passive, high-efficiency thermally-localized solar desalination. *Energy Environ. Sci.* **14**, 1771–1793 (2021).

22 Xu, K., Wang, C., Li, Z., Wu, S. & Wang, J. Salt Mitigation Strategies of Solar‐Driven Interfacial Desalination. *Adv. Funct. Mater.* **31** (2020).

23 Shi, Y. *et al.* Solar Evaporator with Controlled Salt Precipitation for Zero Liquid Discharge Desalination. *Environ. Sci. Technol.* **52**, 11822–11830 (2018).

24 Ni, G. *et al.* A salt-rejecting floating solar still for low-cost desalination.

Energy Environ. Sci. **11**, 1510–1519 (2018).

25 Cussler, E. L. *Diffusion : mass transfer in fluid systems*. 2nd edn, (Cambridge Univ. Press, 2000).

26 Koneshan, S., Rasaiah, J. C., Lynden-Bell, R. M. & Lee, S. H. Solvent Structure, Dynamics, and Ion Mobility in Aqueous Solutions at 25 °C. *J. Phys. Chem. B* **102**, 4193–4204 (1998).

27 Ohtaki, H. & Radnai, T. Structure and dynamics of hydrated ions. *Chem. Rev.* **93**, 1157–1204 (2002).

28 Nield, D. A. & Bejan, A. *Convection in Porous Media*. 5th edn, (Springer, 2017).

29 Xu, K., Wang, C., Li, Z., Wu, S. & Wang, J. Salt Mitigation Strategies of Solar-Driven Interfacial Desalination. *Adv. Funct. Mater.* **31** (2020).

30 Qazi, M. J., Salim, H., Doorman, C. A. W., Jambon-Puillet, E. & Shahidzadeh, N. Salt creeping as a self-amplifying crystallization process. *Sci. Adv.* **5**, eaax1853 (2019).

31 Zhang, H., Wu, Z. & Francis, L. F. Formation of salt crystal whiskers on porous nanoparticle coatings. *Langmuir* **26**, 2847–2856 (2010).

32 Townsend, E. R. *et al.* Additive Induced Formation of Ultrathin Sodium Chloride Needle Crystals. *Cryst Growth Des* **18**, 755–762 (2018).

33 Yang, S., Zhang, F., Ding, H., He, P. & Zhou, H. Lithium Metal Extraction from Seawater. *Joule* **2**, 1648–1651 (2018).

34 Zhang, C. *et al.* Designing a next generation solar crystallizer for real seawater brine treatment with zero liquid discharge. *Nat. Commun.* **12**, 998 (2021).

Supporting Information for Chapter 4

1. COMSOL modeling

To better demonstrate the impacts of convection minimization through pore size reduction on selective crystallization, we developed a mechanistic model by coupling fluidic flow and mass transfer in the evaporator from Figure 4.1. The numerical simulation was conducted using the finite element method in COMSOL Multiphysics 6.1. Due to the symmetry of the evaporator in Figure 4.1, a two-dimensional axisymmetric model was built for simulation analysis. The GFM was modeled as a homogenized porous medium for simplicity, computational efficiency, and consistency with experimental conditions. The flow in porous media is governed by a combination of the continuity equation and the momentum equation, which together form the *Brinkman Equations*[1]*:*

$$\nabla\cdot[-pI+K]-\left(\mu k^{-1}+\beta\rho|u|+\frac{Q_m}{\varepsilon_p^2}\right)u+F+\rho g=0 \qquad \text{Equation 4.4}$$

$$\rho\nabla\cdot u=Q_m \qquad \text{Equation 4.5}$$

where μ is the dynamic viscosity of the fluid ($kg\cdot m^{-1}\cdot s^{-1}$), u is the velocity vector ($m\cdot s^{-1}$), ρ is the density of the fluid ($kg\cdot m^{-3}$), p is the pressure (Pa), ε_p is the porosity of the porous medium, k (m^2) is the permeability of the porous medium, and Q_m is a mass source or sink ($kg\cdot m^{-3}\cdot s^{-1}$)[2-4].

For solute transport, we used the *Transport of Diluted Species* module, which accounted for the diffusion of solutes through the porous medium. The

transport equation applied was:

$$\frac{\partial C}{\partial t} = \nabla \cdot (D \nabla C) \qquad \text{Equation 4.6}$$

where C is the solute concentration ($g \cdot L^{-1}$) and D is the diffusion coefficient ($m^2 \cdot s^{-1}$).

The *Kozeny–Carman* equation was used to estimate the permeability of the membrane:

$$k = \frac{d_p^2}{180} \frac{\varepsilon_p^3}{(1-\varepsilon_p)^2} \qquad \text{Equation 4.7}$$

where d_p is the average pore size of the membrane (m).

Due to reduced solution phase volume and increased diffusion length, the effective diffusion coefficient of species i in the membrane is expressed as:

$$D_i^e = \frac{\varepsilon}{\tau} D_i \qquad \text{Equation 4.8}$$

Where D_i is the diffusive coefficient i in the bulk solution ($m^2 \cdot s^{-1}$), ε is the porosity of the membrane and τ is the tortuosity of the membrane.

2. Evaporation efficiency

Solar evaporation selective crystallization experiments were conducted in the laboratory at a controlled temperature of 25°C and a relative humidity of 60%. The solar-to-vapor conversion efficiency is a key performance indicator used to evaluate a solar crystallizer's ability to effectively utilize solar energy for water evaporation and salt crystallization. A higher efficiency indicates better photothermal conversion and evaporation performance, which is critical for

achieving energy-efficient salt crystallization. Accordingly, the solar-to-vapor conversion efficiency (η, %) of the solar crystallizer was calculated using the following equation[5]:

$$\eta = \frac{mH_{LV}}{q_{solar}} \quad \text{Equation 4.9}$$

where η is the solar–to–vapor photothermal conversion efficiency, m is the net evaporation rate after subtracting the evaporation rate in the dark from the evaporation rate under light conditions, and H_{LV} is the total enthalpy change from water to vapor (including latent heat and sensible heat), and q_{solar} is the simulated solar energy intensity. Under standard solar irradiation (1 kW·m^{-2}), the evaporation rate of pure water was measured at 1.63 kg·m^{-2}·h^{-1}, while the baseline evaporation rate in the dark was 0.28 kg·m^{-2}·h^{-1}. Based on these values, the calculated solar photothermal conversion efficiency reached as high as 91.27% under regular solar radiation. This indicates that the solar crystallizer can effectively utilize solar energy for both water evaporation and salt crystallization.

3. Economic evaluation and comparative analysis of the solar evaporator for NaCl extraction from seawater

The solar evaporator in Figure 4.1 consists of three main components: glass fiber filtration membrane, PS foam, and carbon black coating. To construct 1 m^2 solar evaporator, the required material quantities are [Glass fiber filtration membrane: 1 m^2], [PS foam: 1 m^2], and [Carbon black: 1 g]. Based on

their respective unit prices (Supplementary Table 4.1), the total cost of solar evaporator is calculated to be 0.35 USD·m^{-2}. The salt production rate of traditional seawater saltpans is approximately 14 g·m^{-2}·d^{-1}, with NaCl purity ranging from 85% to 90% due to the lack of Na^+/K^+ separation[6]. Since the market value of NaCl increases significantly with higher purity, effective Na^+/K^+ separation technology for high-purity NaCl production can greatly enhance the product's desirability and economic value. By producing high-purity NaCl at higher rate of 28 g·m^{-2}·d^{-1}, this solar evaporator generates annual revenues of 2.90 × 10^6 USD·km^{-2}·y^{-1}, which fully covers the initial investment costs. At the same time, the profitability is nearly 20 times higher than that of traditional seawater saltpans, which generates 0.15 × 10^6 USD·km^{-2}·y^{-1}, demonstrating that our approach is highly scalable and commercially viable for high-purity salt production on a large scale. Moreover, we believe that the cost of this system can be further reduced through various optimization strategies. Firstly, by identifying more affordable alternatives for the filtration membrane, PS foam, or carbon black coating, we can reduce material costs without compromising the system's performance. Additionally, we believe that optimizing the manufacturing process and scaling up production will lead to economies of scale, thereby further reducing the cost of this system. As these improvements are realized, we are confident that this technology will become increasingly competitive, cost-effective, and well-suited for large-scale, real-world

applications.

Meanwhile, to further expand the application scenarios of the existing technology, we are exploring the integration of selective crystallization with MVR and heat pump low temperature evaporation technologies to broaden its application in industrial wastewater treatment. By optimizing the evaporation material parameters according to our theory, our preliminary results indicate that high-purity NaCl was successfully obtained from real seawater at a higher crystallization rate of 300 $g \cdot m^{-2} \cdot h^{-1}$ and an evaporation rate of 16 $kg \cdot m^{-2} \cdot h^{-1}$ using electric-heating-driven evaporation. Meanwhile, to meet practical application needs, we also propose a comprehensive approach to minimizing costs while maintaining high performance. Initially, to address the investment costs, we will focus on the optimal selection of materials and the design of equipment. By choosing cost-effective materials that meet performance requirements and developing energy-efficient equipment, we aim to reduce the initial expenditure required for implementation. This strategy will help lower the barrier to entry and promote the adoption of the technology in early-stage applications. For long-term operation, we will implement additional measures to further reduce costs. These include optimizing system design to improve energy efficiency, enhancing material durability to extend equipment lifespan, and increasing operational efficiency to lower ongoing maintenance and energy costs. Through these integrated strategies, we aim to make the technology

economically viable and sustainable for large-scale industrial use, ensuring long-term cost savings and continued high performance.

4. Effect of Na_2SO_4 and K_2SO_4 on NaCl selective crystallization of solar evaporator

In the case of NaCl and KCl, the overall diffusion rate of the salt is primarily controlled by the cation with the lower diffusion coefficients. Since K^+ diffuses faster than Na^+, NaCl exhibits a lower diffusion rate than KCl, leading to selective crystallization of NaCl. However, the low diffusion coefficient of SO_4^{2-} in seawater may alter this selective performance. Due to the lower diffusion coefficient of SO_4^{2-}, the mutual diffusion coefficient of Na_2SO_4 and K_2SO_4 are 1.23×10^{-9} $m^2 \cdot s^{-1}$ and 1.53×10^{-9} $m^2 \cdot s^{-1}$, respectively, which are both lower than NaCl (1.61×10^{-9} $m^2 \cdot s^{-1}$). Given the low concentration of SO_4^{2-} in seawater, the maximum diffusion rates of Na_2SO_4 and K_2SO_4 are calculated as 3.92×10^{-2} $kg \cdot m^{-2} \cdot h^{-1}$ and 6.94×10^{-2} $kg \cdot m^{-2} \cdot h^{-1}$, which are both higher than their upward transfer rates (Na_2SO_4: 2.85×10^{-2} $kg \cdot m^{-2} \cdot h^{-1}$ and K_2SO_4: 2.10×10^{-3} $kg \cdot m^{-2} \cdot h^{-1}$). Thus, no Na_2SO_4 and K_2SO_4 crystallization occurs under these conditions, as their diffusion rates exceed their upward transfer rates, preventing their effective crystallization during the process.

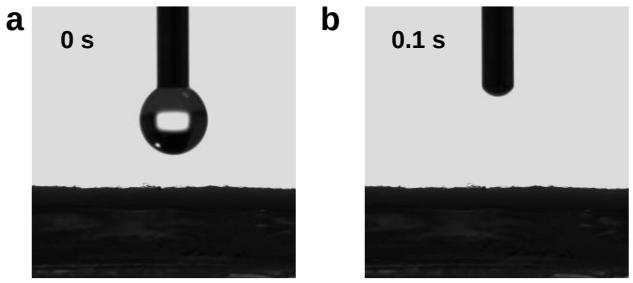

Supplementary Figure 4.1. **(a-b)** Image of the water drop hanging above the glass fiber membrane and the moment it touches the glass fiber membrane surface. The glass fiber membrane coated with carbon black can absorb a water droplet upon touching it within 0.1 s, indicating its high hydrophilicity.

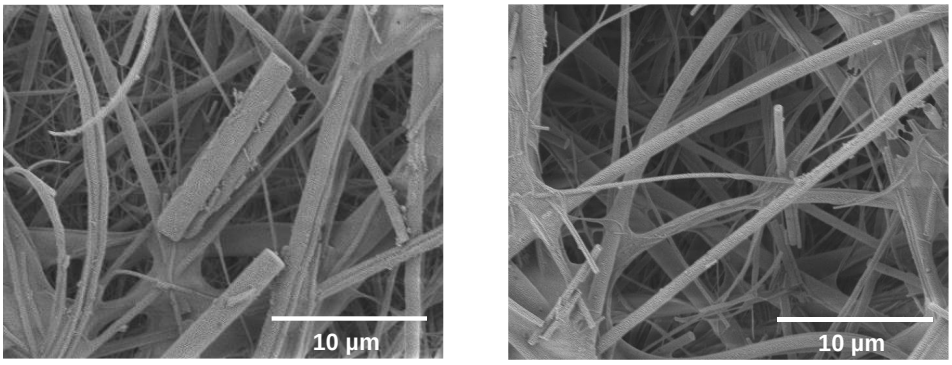

Supplementary Figure 4.2. SEM image of the glass fiber membrane coated with carbon black, displaying hydrophilic microchannels that enable efficient ion transfer during solar evaporation.

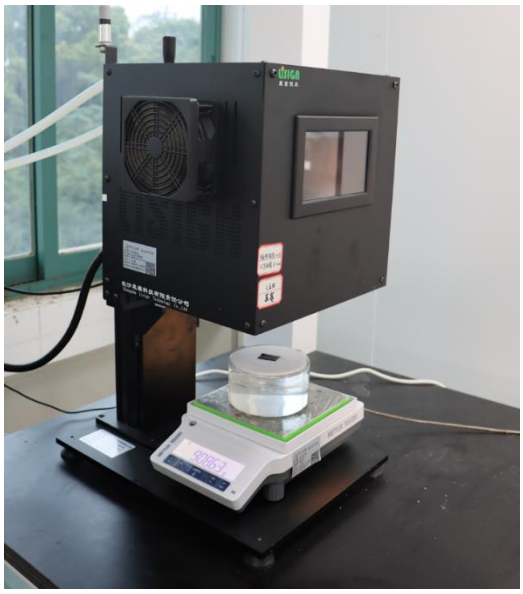

Supplementary Figure 4.3. Lab-made experimental setup for the solar evaporator evaluation.

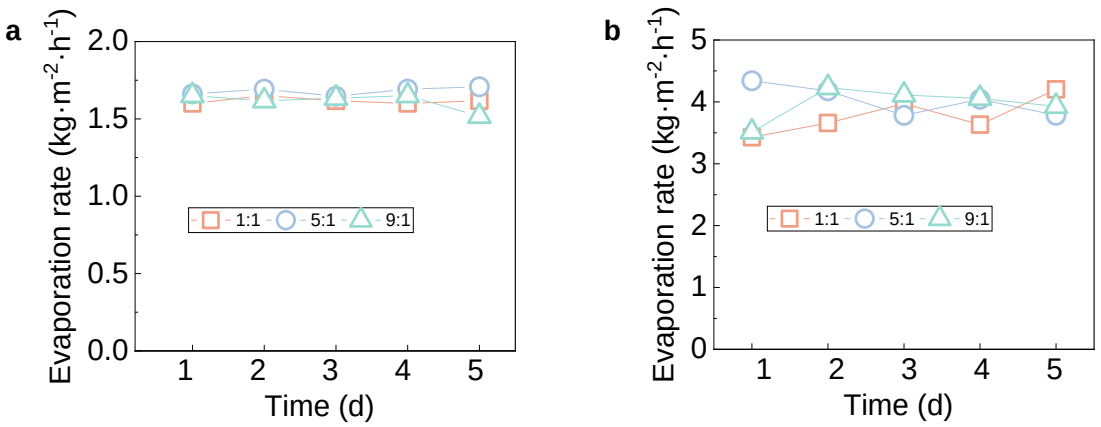

Supplementary Figure 4.4. Evaporation rate of the solar crystallizer with a 7-mm-thick PS foam during evaporation of mixed KCl/$BaCl_2$ solutions (a) or mixed LiCl/$MgCl_2$ solutions (b) at different ratios under regular solar radiation.

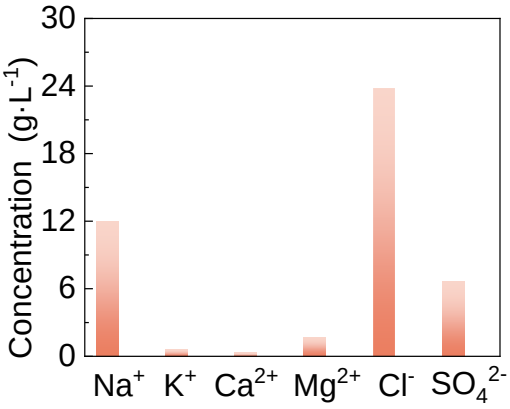

Supplementary Figure 4.5. Ion composition of the real seawater.

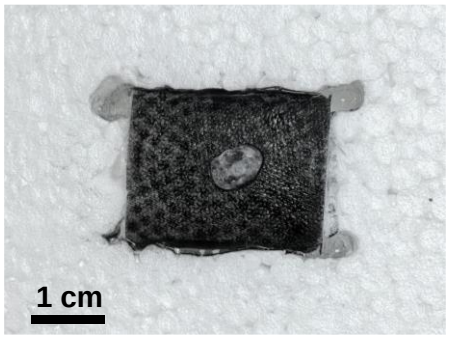

Supplementary Figure 4.6. Photos of the high-purity NaCl on the 7-mm-thick solar crystallizer.

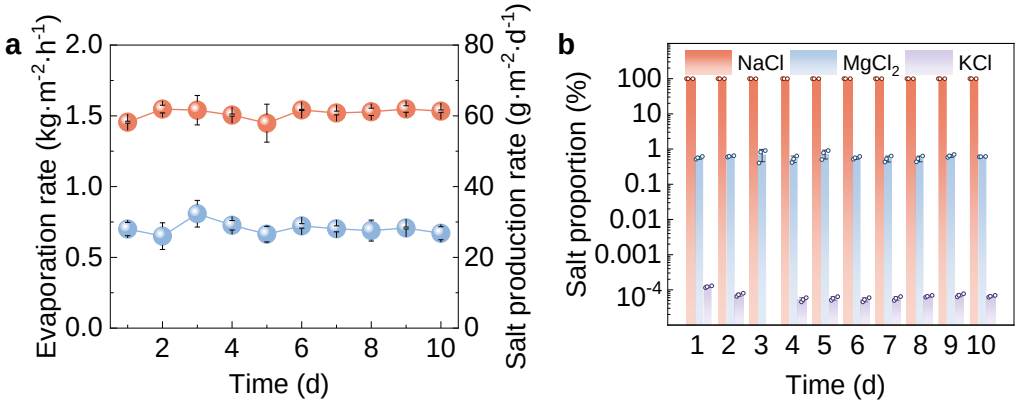

Supplementary Figure 4.7. Long-term high-purity NaCl production from real seawater. (a) Evaporation rate and salt production rate of the 7-mm-thick solar evaporator for real seawater evaporation under one-sun illumination. The data

points represent the evaporation rate and salt production rate, respectively. Visual guidance is provided by the arrows pointing to the corresponding y axes. (b) The proportion of the crystallized salts on the evaporator (error bars in c and d represent the standard deviation from three replicates).

To validate the long-term stability of the designed selective crystallization system, we conducted a ten-day experiment, during which the selective crystallization performance showed no significant changes. However, for the successful application of this technology in real-world scenarios, the use of high-performance materials and advanced anti-fouling designs is essential to ensure stable selective crystallization performance and improve cost-effectiveness. To achieve this, advanced technologies, such as 3D printing[7], could be utilized to develop more efficient, stable, cost-effective evaporators for large-scale application.

Supplementary Table 4.1. Unit price of different items of the solar evaporator

Items	Unit price
99% NaCl (USD·t^{-1})	273
Crude seawater salt (USD·t^{-1})	28
Glass fiber filter membrane (USD·m^{-2})	0.3
PS foam (USD·m^{-2})	0.05
Carbon black (USD·g^{-1})	2.5×10^{-4}

Reference

1 Mukherjee, R., Bhunia, P. & De, S. Long term filtration modelling and scaling up of mixed matrix ultrafiltration hollow fiber membrane: a case study of chromium(VI) removal. *J. Membr. Sci.* **570-571**, 204–214 (2019).

2 Yang, H. *et al.* Tailoring the salt transport flux of solar evaporators for a highly effective salt-resistant desalination with high productivity. *ACS Nano* **16**, 2511–2520 (2022).

3 Zhang, L. *et al.* Highly efficient and salt rejecting solar evaporation via a wick-free confined water layer. *Nat. Commun.* **13**, 849 (2022).

4 Tu, J., Yeoh, G.-H. & Liu, C. *Computational Fluid Dynamics (Third Edition)*. (Butterworth-Heinemann, 2018).

5 Ma, J. *et al.* Achieving Solar-Thermal-Electro Integration Evaporator Nine-Grid Array with Asymmetric Strategy for Simultaneous Harvesting Clean Water and Electricity. *Adv. Sci.* **10**, 2303815 (2023).

6 Meng, Q.-W. *et al.* Optimizing selectivity via membrane molecular packing manipulation for simultaneous cation and anion screening. *Sci. Adv.* **10**, eado8658 (2024).

7 Pu, Y. *et al.* Large-scale 3D printed fouling-resistant self-floating evaporator. *Nat. Commun.* **16**, 3677 (2025).

5 Dissolution-driven selective crystallization of high-purity salt through simple and sustainable one-step evaporation

Abstract

High-purity salt production from water is crucial for resource recovery and environmental sustainability, yet selective crystallization has seen limited application due to a poor understanding of its fundamental mechanisms. Here, we introduce a dissolution-driven selective crystallization strategy designed for high-purity salt production directly from water. Our strategy centers on precisely regulating hydrated ion transfer driven by convection from crystal surfaces to the solution, leveraging differences in salt dissolution rates to ensure the complete dissolution of unwanted salt into the source solution and retain targeted salt in the crystals. To demonstrate this concept, we developed a bridge-like solar evaporator that can control the ion convection rate by regulating the mass transfer distance. Using NaCl/KCl separation as an example, this strategy achieved one-step selective crystallization of KCl crystals with a purity of 99.91% from a 1:1 mixed NaCl/KCl solution under simulated day-night cycles. Beyond its success in extracting resources from water, this strategy also enabled the production of KCl crystals with a purity of 99.50% from mixed NaCl/KCl solid salts through a single-step dissolution

process. This strategy further demonstrates broad applicability, extending to other mixed salt systems like LiCl/KCl and $CaCl_2$/KCl, consistently yielding high-purity salt. The practical potential was further demonstrated by the direct production of KCl with a purity greater than 99% at a rate of 36.60 $g \cdot m^{-2} \cdot d^{-1}$ from fly ash leachate during outdoor tests. This work underscores the untapped potential of dissolution kinetics for high-purity salt production, offering a promising new pathway for sustainable resource extraction.

5.1 Introduction

In previous chapters, we detailed the development of a diffusion-driven selective salt crystallization method. This achievement underscored the potential of precisely controlled crystallization processes in addressing complex salt separation challenges. Beyond crystallization, dissolution is a fundamental process in salt separation, often used to release salt ions from the solid salt into solution for subsequent separation process[1-4]. Salt dissolution is initiated by the hydration of surface ions in the salt crystal, which disrupts the crystal lattice and releases hydrated ions into water[5-7]. Due to the accumulation of hydrated ions at the crystal–solution interface, a concentration gradient is established between the crystal surface and the source solution, driving the hydrated ions to subsequently migrate into bulk solution via diffusion and convection[8-10]. In this process, the variations in ion hydration reactions generally lead to markedly distinct dissolution rates among salts[11-13].

While different salts exhibit variations in dissolution rates, leveraging these disparities for selective salt separation remains challenging due to its unpredictability and stochastic nature. Once the salt dissolves into solution, the hydrated ions undergo diffusion and convection governed by thermal motion and bulk fluid dynamics[8-10], rendering both processes essentially uncontrollable under normal conditions. This stochastic transport leads to fluctuations in the local concentration of hydrated ions at the crystal–solution interface, which in turn induces significant variability in the hydration dynamics. As a result, salt dissolution rate becomes highly unstable and intrinsically unpredictable, falling short of the controllability and reproducibility required for effective separation.

Thus, if ion transport during the dissolution process can be effectively controlled, the differences in salt dissolution rates may offer a potential opportunity for selective separation. During solar interfacial evaporation and crystallization, as salt crystallizes on the evaporating surface, a localized, saturated salt solution forms at the crystal-liquid interface. This saturation creates a critical concentration gradient with the bulk solution, driving the redissolution of salt crystals via both diffusion and convection[11,14]. Meanwhile, by constraining these transport processes within the pores of the evaporator, their rates can be precisely controlled via the pore structure[9,10,15]. This allows for the modulation of ion transport and the regulation of salt dissolution, ensuring that salts with higher dissolution rates dissolve completely, while salts

with lower dissolution rates remain within the solid crystal.

In this chapter, we propose a dissolution-driven selective crystallization strategy for directly producing high-purity salts from mixed solutions. This approach fundamentally relies on purposefully regulating the transfer of hydrated ions driven convection from the crystal surface to the source solution, enabling a regulated dissolution to ensure complete dissolution of unwanted salt with a lower dissolution rate. As a proof of concept, we designed a bridge-like evaporator that enabled the precise control of ion convection rate by adjusting the transfer distance. Using NaCl/KCl as a model system—chosen for their similar physicochemical properties—we achieved selective crystallization of KCl with a purity of 99.91% from a 1:1 mixed NaCl/KCl solution during simulated day-night cycles. Extending this principle, we successfully harnessed a direct dissolution process to separate mixed NaCl and KCl crystals, achieving direct production of KCl with a purity of 99.50%. The versatility of our approach was further demonstrated by achieving >99% pure solid salt production from other mixed salt systems (LiCl/KCl, $CaCl_2$/KCl). Practical application was demonstrated by achieving 99% pure KCl production at a rate of 36.60 $g \cdot m^{-2} \cdot d^{-1}$ from real fly ash leachate in outdoor field tests.

5.2 Results

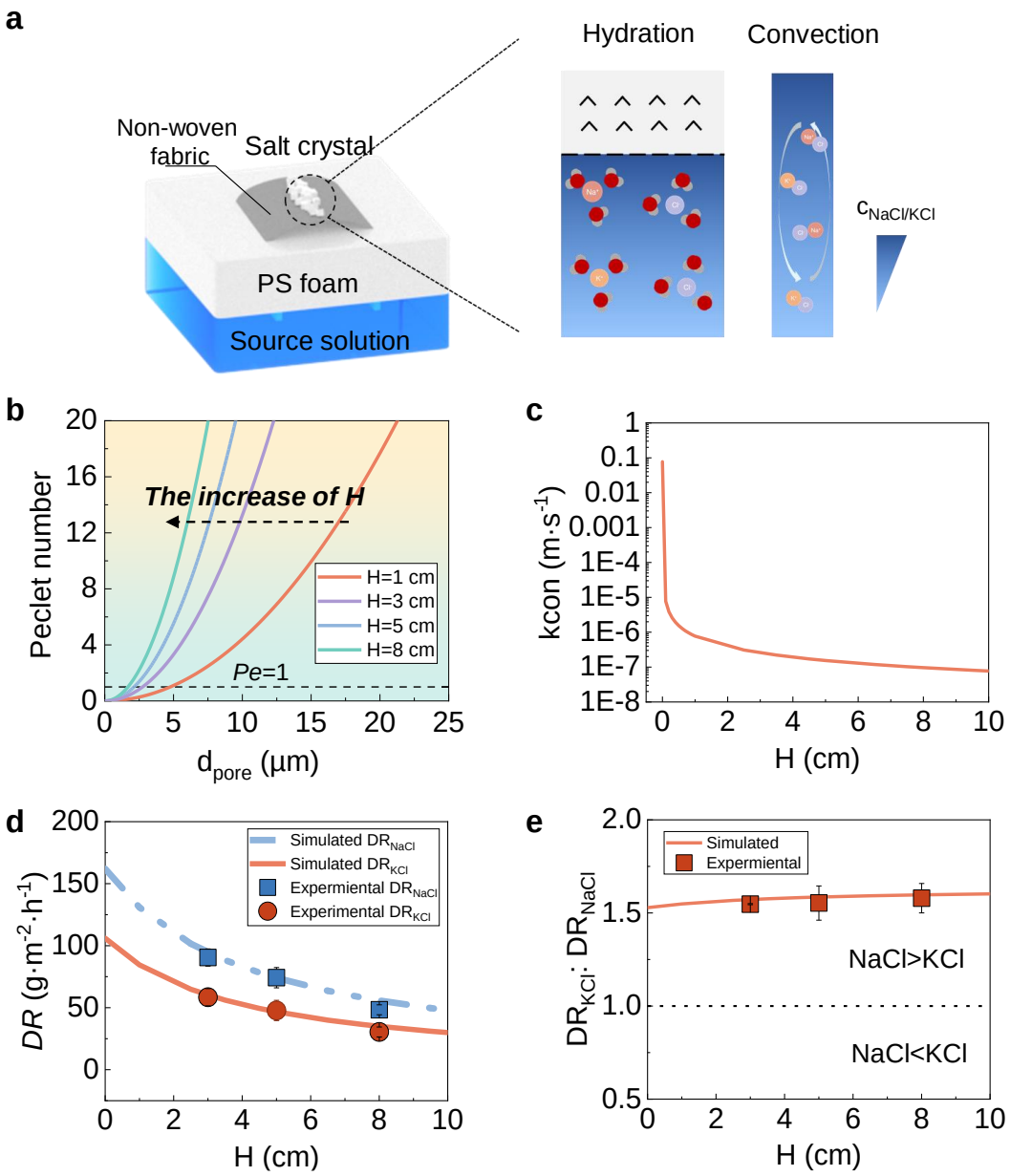

Figure 5.1. Precise control of salt dissolution rate via evaporator's height. (a) Schematic illustration of the salt dissolution process in the designed bridge-like evaporator. (b) The Péclet number (*Pe*) of the designed bridge-like evaporator as a function of the pore size of non-woven fabric and evaporator's height. (c) Convective mass transfer coefficient of the evaporator as a function

of its height. (d) COMSOL simulated and experimental NaCl/KCl dissolution rate of the evaporator as a function of its height. Mixed crystals of NaCl/KCl with a 1:1 mass ratio was compressed into a circular tablet and placed at the center of the evaporator's surface floating on water to conduct salt dissolution at 25^{o}C. Mixed crystals are obtained by drying mixed NaCl/KCl solution with a mass ratio of 1:1. The dissolution rate was determined as the average value derived from five independent experimental replicates. (e) COMSOL simulated and experimental ratio of NaCl and KCl dissolution rate as a function of its height.

5.2.1 Design of a bridge-like evaporator for controlled dissolution processes

During solar interfacial evaporation and crystallization, the solar evaporator typically consists of a porous structure that floats on water while localizing heat at the evaporation interface[9,14,16,17]. As water evaporates, salt crystallizes at the evaporation surface. Due to the concentration gradient between the evaporation interface and the source solution, the salt crystals would be continuously dissolved, releasing hydrated ions, which are transported into the source solution through the porous channels of the evaporator[14,18,19]. Due to the confinement of ion movement within the pores of the evaporator, ion transport can be regulated by the pore structure[9,10].

To demonstrate this, we designed a novel bridge-like solar evaporator. This evaporator's structure comprises a rectangular porous non-woven fabric positioned atop a PS foam, which allows it to float stably on the water surface (Figure 5.1a). Recognizing that ion transfer in water is often governed by convection during salt separation processes[20,21], the evaporator was specifically engineered to enable convection-dominated ion transfer (*Pe* > 1). This is achieved by increasing the convection rate through an enlarged pore size of the non-woven fabric and an increased ion transfer distance. The ion transfer distance within the evaporator corresponds to the height of the PS foam (*H*). As demonstrated in Figure 5.1a, with a constant height of 1 cm, increasing the non-woven fabric pore size from 2.5 μm to 21 μm elevated the Pe from 0.3 to 20 (Figure 5.1b). Similarly, for a non-woven fabric pore size of 21 μm, the Pe consistently remained greater than 1 as the height decreased from 8 cm to 1 cm (Figure 5.1b). Thus, non-woven fabric with an average pore size of 21 μm and a porosity of 83% was used to fabricate the evaporator[9,22] (Supplementary Figure 5.5). In this evaporator, the salt dissolution rate can be expressed as follows[15]:

$$DR_i = \frac{k_{con} k_{di}^i}{k_{con} + k_{di}^i} \left(c_s^i - c_0^i\right) \qquad \text{Equation 5.1}$$

where DR_i is the dissolution rate of salt i (g·m^{-2}·h^{-1}), $c_{saturated}$ and c_0 are the saturated salt solution concentration (g·L^{-1}) and the source solution salt concentration (g·L^{-1}), respectively, and k_{di}^i is the salt i dissolution rate

constant ($m \cdot s^{-1}$), k_{con} is the convective mass transfer coefficient ($m \cdot s^{-1}$).

The evaporator's ability to control ion convection is demonstrated by the regulation of its convective mass transfer coefficient. This coefficient is determined by, and inversely proportional to, the evaporator's height (Supplementary Text 5.1). Specifically, decreasing the height from 10 cm to 1 cm resulted in an increase of the convective mass transfer coefficient from 7.71×10^{-8} $m \cdot s^{-1}$ to 7.71×10^{-7} $m \cdot s^{-1}$ (Figure 5.1c). Consequently, within this evaporator, salt dissolution rate can be accurately controlled by simply adjusting the height of the evaporator. The NaCl/KCl system serves as a model for challenging separations due to its highly similar physicochemical properties[23], yet it possesses distinct dissolution rates. This difference can be quantified by their dissolution rate constants: KCl was experimentally determined to be 1.84×10^{-7} $m \cdot s^{-1}$ while NaCl was 1.97×10^{-7} $m \cdot s^{-1}$. Based on COMSOL simulation rates, reducing the height from 8 cm to 3 cm precisely increases NaCl's dissolution rate from 55.79 $g \cdot m^{-2} \cdot h^{-1}$ to 94.58 $g \cdot m^{-2} \cdot h^{-1}$ and KCl's from 34.98 $g \cdot m^{-2} \cdot h^{-1}$ to 60.30 $g \cdot m^{-2} \cdot h^{-1}$ (Figure 5.1d). These simulated rates matched well with experimental observation. Meanwhile, both COMSOL simulation and experimental results demonstrated that, while achieving precise regulation of dissolution rates, NaCl's dissolution rate consistently remained approximately 1.5 times faster than KCl's (Figure 5.1e). Therefore, in this regulated dissolution process, we can ensure the complete dissolution of salts with higher dissolution

rates into source solution, while retaining salts with lower dissolution rates in the crystals. Based on the dissolution rate difference between the two salts, we simulated the selective dissolution behavior of mixed salt crystals and identified the critical point for obtaining high-purity KCl. Using a 1:1 (mass ratio) mixed NaCl/KCl solid as a model, the simulation showed that when the total crystal mass drops to approximately 18% of its original value during dissolution, a solid phase consisting of pure KCl can be recovered (Supplementary Figure 5.1).

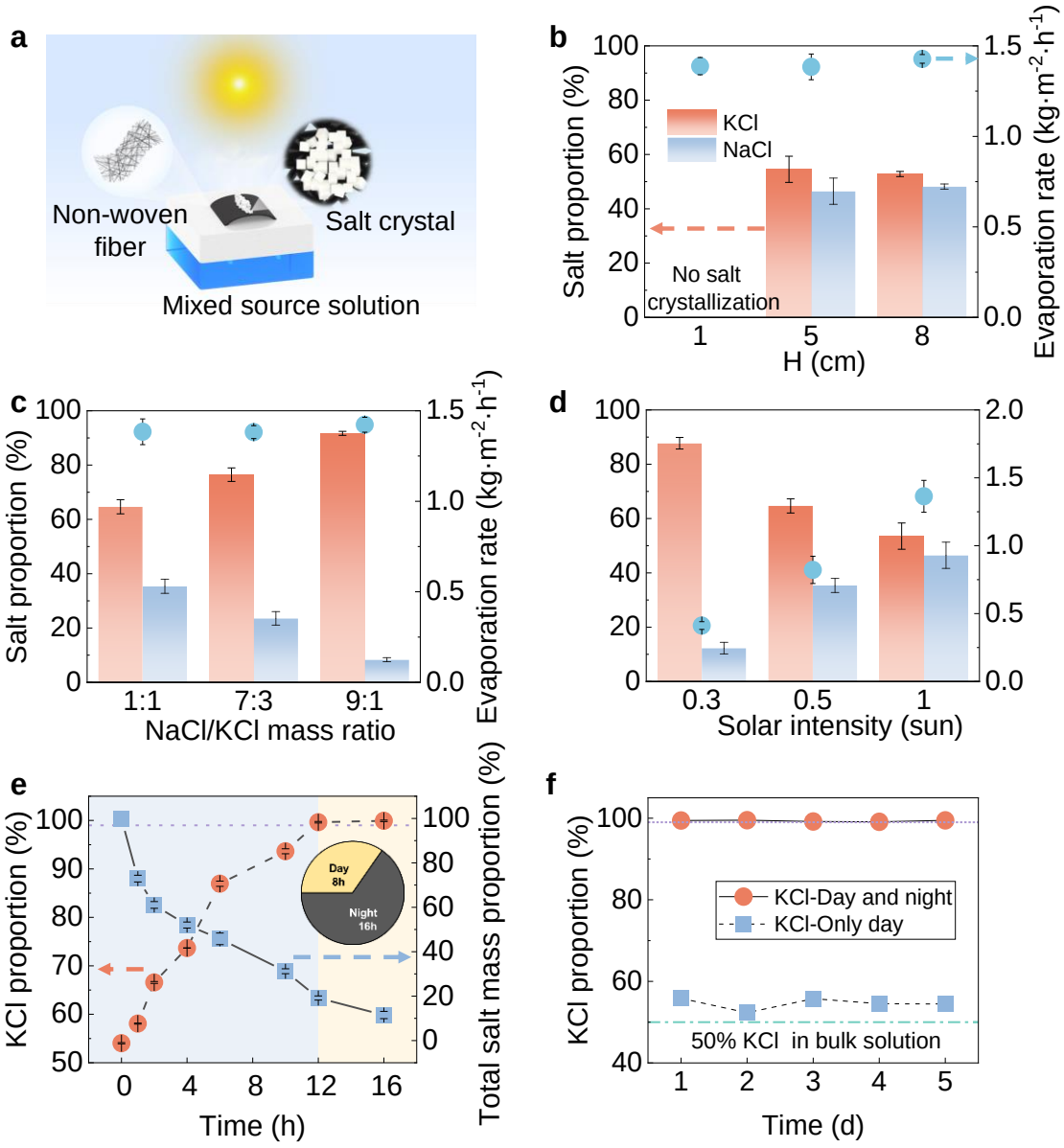

Figure 5.2. Selective KCl crystallization performance of the solar evaporator. (a) Schematic illustration of the selective crystallization system. (b-d) Evaporation rate and NaCl/KCl proportion in the crystallized salt of the solar evaporators with different heights under regular solar radiation as a function of the evaporator height (b), solar intensity (c) and NaCl/KCl mass ratios of the mixed source solution (d). NaCl and KCl concentrations remain stable at 20 $g \cdot L^{-1}$ each in (a), the evaporator height is maintained at 5 cm in (c), and the total

salt concentration is kept at 40 $g \cdot L^{-1}$ in (d). (e) KCl proportion in the crystallized salt as a function of the total crystallized salt mass (normalized to the initial value) during the simulated nighttime period (16 hours). The total salt mass proportion in (e) refers to the mass of crystallized salt normalized to the initial total salt mass. The salt crystals were first formed under simulated daytime solar irradiation, followed by a nighttime stage in which only solar exposure was removed while all other conditions were kept constant, thereby simulating a day–night alternation cycle (16 hours daytime, 8 hours nighttime). The total salt concentration is kept at 40 $g \cdot L^{-1}$ and the ambient temperature was 25°C. Visual guidance is provided by arrows pointing to the corresponding y axes. (f) Stability of selective KCl crystallization during simulated day-night alternation. The total salt concentration is kept at 40 $g \cdot L^{-1}$ and the ambient temperature was 25°C.

5.2.2 Solar interfacial evaporation selective KCl crystallization via dissolution rate difference

To demonstrate selective crystallization, we applied our designed evaporator to the solar evaporation crystallization process of mixed NaCl/KCl solutions (Figure 5.2a). To achieve efficient solar evaporation, the non-woven fabric was coated with carbon black (Supplementary Figures 5.2 and 5.3). This coating achieved 91% solar absorption (Supplementary Figure 5.3), while preserving the intrinsic pore structure of the non-woven fabric (Supplementary

Figures 5.4 and 5.5). When sunlight illuminates the evaporator floating on the mixed NaCl/KCl solution, the salt solution is transported to the evaporation surface by capillary force, where the concentration reaches saturation and crystallization occurs as water evaporates[24,25]. Meanwhile, due to concentration differences, salt crystals on the evaporation surface dissolve and backflow into the source solution via convection[9,15]. As the capillary flow is non-selective towards different salts, but NaCl has a higher dissolution rate than KCl, selective KCl crystallization occurs during solar evaporation.

To evaluate selective KCl crystallization performance, evaporators with different heights were floated on a mixed NaCl and KCl solution (20 $g \cdot L^{-1}$ each) under regular solar radiation (Supplementary Figure 5.7). The evaporation rate for all evaporators reached 1.4 $kg \cdot m^{-2} \cdot h^{-1}$ (Figure 5.2b). Meanwhile, the 5-cm-high and 8-cm-high evaporators yielded a higher KCl proportion of 57% and 52%, respectively, in contrast to the source solution. This indicates the achievement of selective crystallization. However, no crystallization occurred at a height of 1 cm due to the excessively high convection rate[9]. Consequently, a height of 5 cm was selected for further evaluating selective crystallization performance (Figure 5.2b). To assess its robustness, selective crystallization performance was evaluated when the bottom solution's NaCl to KCl mass ratio changed from 1:1 to 1:9. Figure 5.2c demonstrates that a consistently higher KCl proportion was achieved in all crystallized salt under these varied

conditions. These results reveal that Due elective crystallization can be achieved by exploiting differences in salt dissolution rates.

Under practical operating conditions, fluctuating solar intensity directly impacts the evaporation rate[24,26,27]. Since the upward capillary flow of salt is non-selective and primarily driven by the evaporation rate, reducing the evaporation rate can effectively suppress this process. This, in turn, enhances crystallization selectivity based on the differences in salt dissolution rates. As demonstrated in Figure 5.2d, reducing the solar intensity to 0.3 sun increased the KCl proportion in salt crystals to 80% at a lower evaporation rate of 0.4 $kg \cdot m^{-2} \cdot h^{-1}$. At night, salt crystallization ceases due to the negligible evaporation rate, while salt dissolution continues, driven by existing concentration gradients, which can further enhance crystallization selectivity. To investigate this effect, we evaluated the selective crystallization performance under simulated day–night alternation (8 h daytime + 16 h nighttime). As shown in Figure 5.2e, the KCl proportion in salt crystals increased to 54% by the end of the daytime. When simulated sunlight was turned off for the nighttime phase, the KCl proportion in salt crystals remarkably increased to 99.63% after 14 hours of dissolution, at which point the total mass proportion of salt crystals had decreased to 20% of its initial value (Figure 5.2e). This value is in close agreement with our simulation predictions, demonstrating that efficient salt separation can be achieved through the controlled dissolution process

(Supplementary Figure 5.1). By the end of the nighttime period, the KCl proportion in the salt crystal further significantly increased to 99.91% (Figure 5.2e). The stability of this selective crystallization performance was further verified over multiple day-night alternations. During a 5-day tests, the KCl proportion in salt crystals consistently reached over 99% (Figure 5.2f).

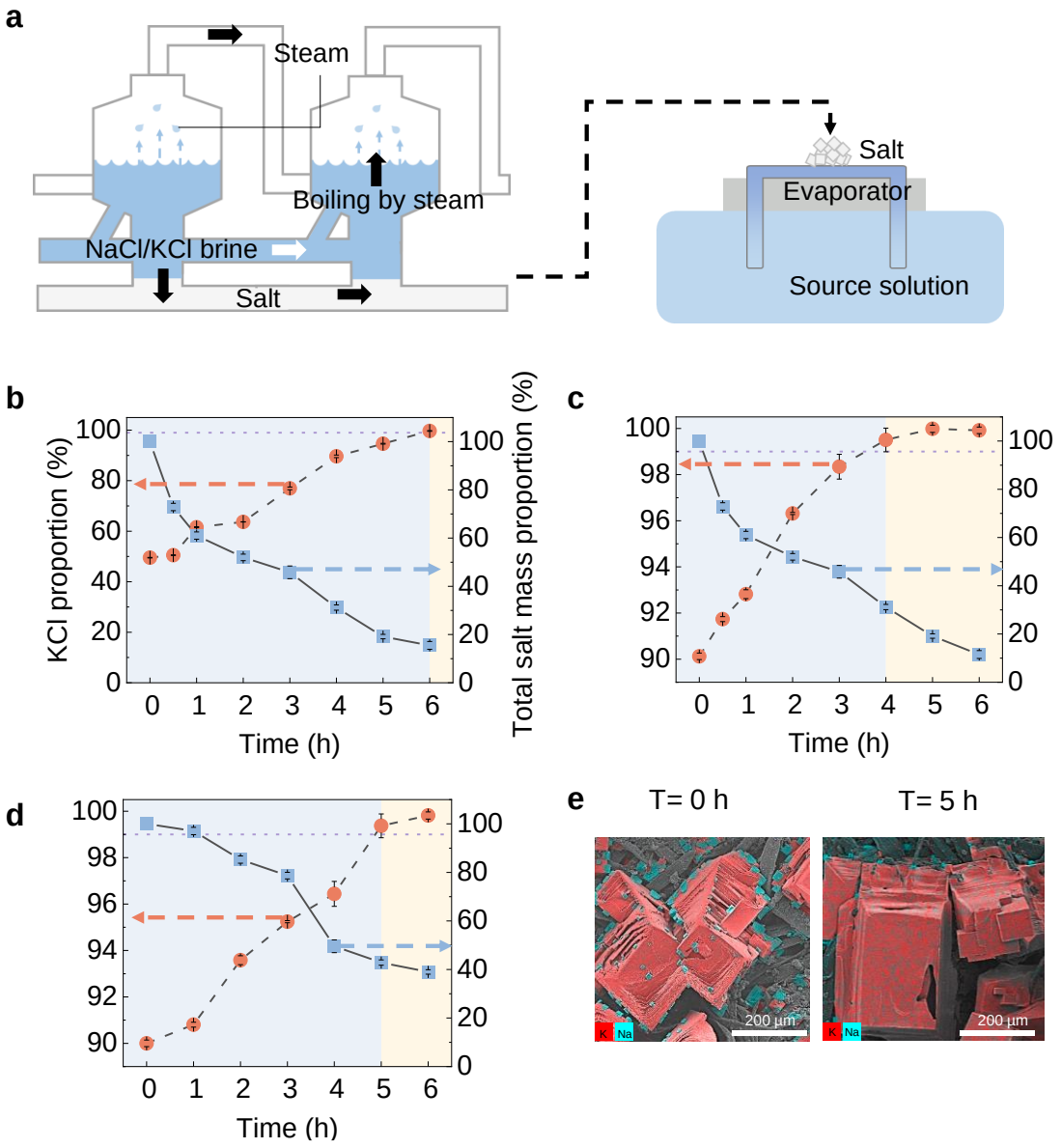

Figure 5.3. Selective dissolution of industrial waste salt produced by

electrical heating. (a) Schematic illustration of the selective dissolution process. (b-c) KCl proportion in the mixed NaCl/KCl crystallized salt with an initial NaCl/KCl mass ratios of 1:1 (b) or 9:1 (c) as a function of the total crystallized salt mass (normalized to the initial value) on the evaporator floating on water during the dissolution process. Mixed crystals were obtained by drying a mixed NaCl/KCl solution with a mass ratio of 1:1 at 80^{o}C. (d) KCl proportion as a function of the total crystallized salt mass (normalized to the initial value) (e) and Energy-dispersive X-ray spectroscopy (EDS) images (d) of the crystallized salt at different dissolution times on the evaporator floating on the simulated fly ash leachate during the dissolution process. The simulated fly ash leachate was prepared by dissolving NaCl and KCl in water at a mass ratio of 9:1, with a total salt concentration of 40 g·L^{-1}. The mixed crystals were obtained by drying a simulated fly ash leachate prepared mixed NaCl/KCl solution with a mass ratio of 9:1 at 80^{o}C. During salt dissolution, the ambient temperature was 25^{o}C. The total salt mass proportion in (b-d) refers to the mass of crystallized salt normalized to the initial total salt mass. Visual guidance in (b-d) is provided by arrows pointing to the corresponding y axes.

5.2.3 High purity salt production from mixed salt crystals by direct dissolution process

In contemporary industrial processes, electrical heating is commonly

utilized to promote salt crystallization of brine[28-30]. However, mixed salt crystals are generally produced due to a lack of selectivity and are considered waste without a subsequent separation process[28-30]. The evaporator was integrated with electric-driven evaporation to separate NaCl/KCl, to validate its coupling capability with current industrial processes (Figure 5.3). Firstly, mixed salt crystals crystallized during evaporation of mixed KCl and NaCl solution with a mass ratio of 1:1 through electric heating (80^{o}C). Then mixed salt crystals were then placed on the evaporator floating on water for a selective dissolution process. As shown in Figure 5.3b, the KCl proportion in the salt crystals increased to 99.67% when the mass of the salt crystal decreased to 15.5% of its original value after 6 hours of dissolution. This demonstrates that high-purity KCl can be directly produced from mixed solids in a single-step selective dissolution process.

Efficient NaCl/KCl separation plays a critical role in enabling the effective extraction of high-purity salts to meet growing resource demands. A representative example is municipal solid waste (MSW) fly ash leachate[31], which is generated through the washing and leaching of incineration fly ash and typically contains high concentrations of NaCl and KCl. Effective separation of these two salts is essential to produce high-purity KCl fertilizers. To further demonstrate the potential for practical application, we investigated the direct dissolution of mixed salt crystals obtained from the evaporation of simulated K-

rich fly ash leachate, which contained KCl and NaCl at a 9:1 mass ratio. These mixed crystals, produced via electric heating at 80 °C, were then placed on the evaporator floating on water for a selective dissolution process. As shown in Figure 5.3c, the KCl proportion in the salt crystals increased to 99.50% when the crystal mass decreased to 30% of its original mass after 4 hours of dissolution. Besides pure water, the original source solution is generally far from saturated[28-30], allowing it to continue dissolving salts. Thus, leveraging this unsaturated original solution for the purification of mixed solids can significantly reduce water consumption. When the source solution was subsequently replaced with the simulated K-rich fly ash leachate, a 99.47% KCl purity was achieved, with the salt crystal mass decreasing to 43% of its original after 5 hours of dissolution (Figure 5.3d). Through Energy-dispersive X-ray spectroscopy (EDS) analysis, we also observed that NaCl was effectively removed via the selective dissolution process, leaving behind high-purity KCl crystals (Figure 5.3e). These results indicate that this selective dissolution process holds significant potential for high-purity salt production in practical applications.

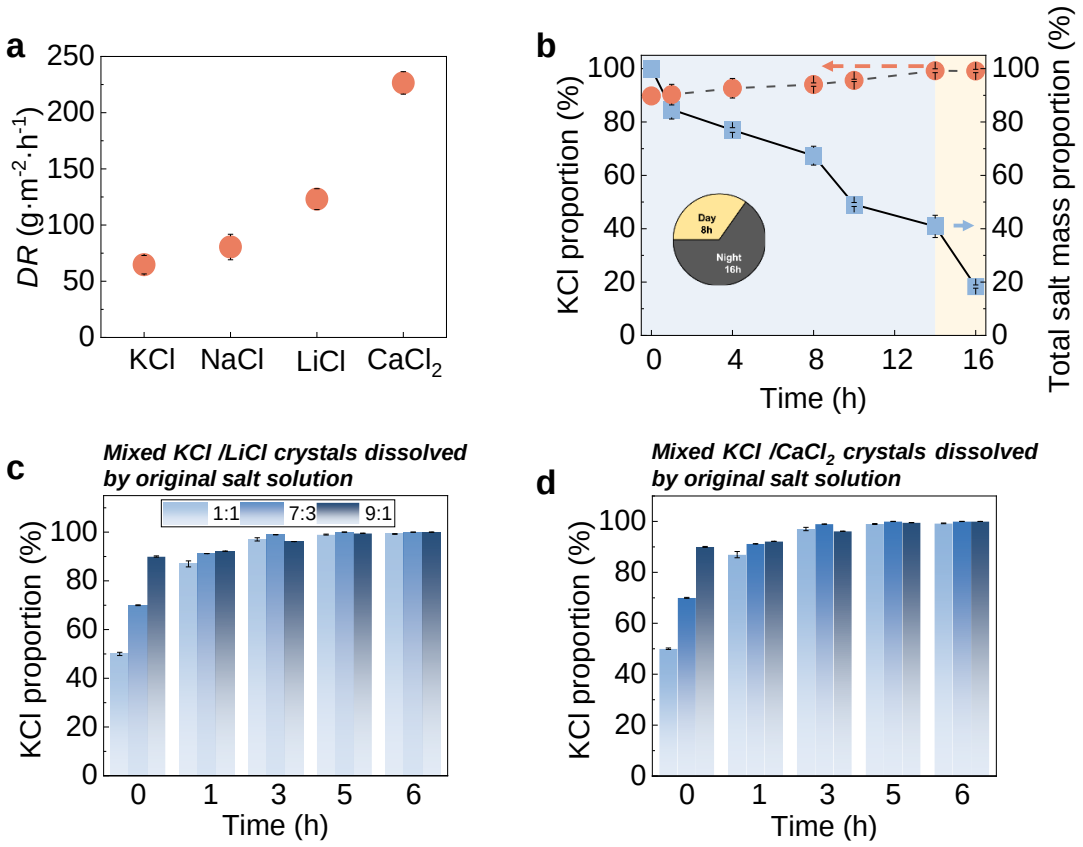

Figure 5.4. Universality of high-purity salt production based on dissolution rate difference. (a) Dissolution rate of various salts in water. The dissolution rate was measured by placing circular salt tablets, pressed from single salt crystals, on a 5-cm-high evaporator floating on water at 25°C. (b) Selective KCl crystallization from a mixed KCl/LiCl source solution with an equal mass ratio via solar evaporation day-night alternation (16 hours daytime, 8 hours nighttime). The total salt concentration was maintained at 60 $g \cdot L^{-1}$. (c-d) Separation of mixed KCl/LiCl salt crystals (c) and KCl/$CaCl_2$ crystals (d) through dissolution by their original salt concentration. Mixed salt crystals were obtained by drying mixed salt solutions with equal mass ratios. The total salt concentration was maintained at 40 $g \cdot L^{-1}$ during the dissolution process, which

was conducted at 25ºC.

5.2.4 Universality of salt separation based on dissolution rate difference

Dissolution rate differences are not limited to NaCl/KCl systems but are also prevalent in various mixed salt systems[32]. For example, the dissolution rates of NaCl, KCl, LiCl, and $CaCl_2$ were determined to be 64, 80, 123, and 227 $g \cdot m^{-2} \cdot h^{-1}$ (Figure 5.4a), respectively. To demonstrate our strategy's universality, we performed solar evaporation for selective KCl crystallization from a 1:1 mixed LiCl/KCl solution. As Figure 5.4b shows, after 8 hours of one-sun illumination, the KCl proportion in the crystallized product reached 90%. This proportion further increased to 99.21% when the salt crystal mass decreased to 40% of its original mass after 14 hours of nighttime dissolution, showcasing high separation efficiency.

Furthermore, mixed LiCl/KCl and KCl/$CaCl_2$ crystals were placed on the evaporator floating on their original mixed salt solution to explore the production of high-purity salts via a direct dissolution process. For LiCl/KCl mixtures with 1:1, 7:3, and 9:1 mass ratios, KCl with a purity over 99% was obtained within 3 hours of dissolution (Figure 5.4c and Supplementary Figure 5.9). A similar trend was observed for KCl/$CaCl_2$ crystals, where the faster dissolution of $CaCl_2$ facilitated the direct extraction of KCl with a purity over 99% (Figure 5.4d and Supplementary Figure 5.10). Therefore, for other mixed salt systems, whether

in solution phase or solid-state, high-purity salt crystals can be effectively produced based on dissolution rate differences.

5.2.5 Outdoor high-purity KCl fertilizer extraction from practical fly ash leachate

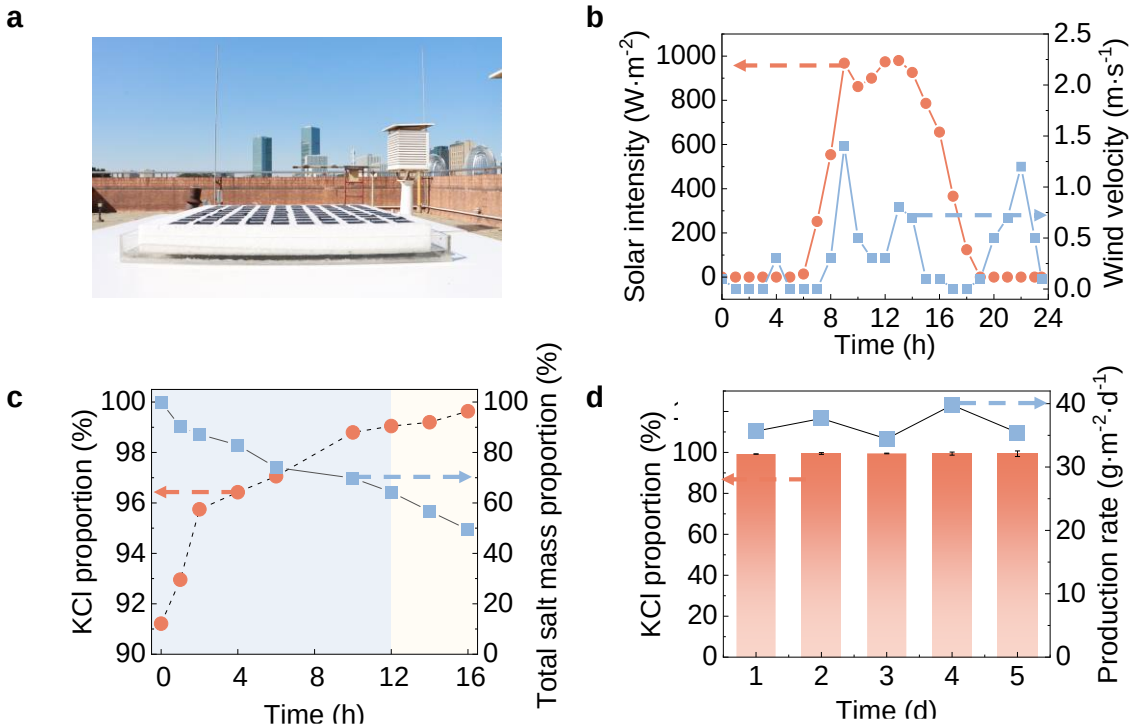

Figure 5.5. Outdoor high-purity KCl fertilizer extraction from fly ash leachate. (a) Photographs of the high-purity KCl fertilizer production system under natural sunlight. (b) Solar intensity and wind velocity during outdoor KCl production. (c) KCl proportion in the crystallized salt as a function of the total crystallized salt mass (normalized to the initial value) during the nighttime period (16 hours). The total salt mass proportion in (c) refers to the mass of crystallized salt normalized to the initial total salt mass. (d) Proportion of KCl in

salt crystals and the crystallization rate during KCl fertilizer production from fly ash leachate during five-day continuous outdoor test.

To evaluate the practical application prospects of our salt separation strategy, we applied it to the high-purity KCl production from real-world K-rich fly ash leachate (Supplementary Figure 5.11), with experiments conducted at Sun Yat-Sen University (Guangzhou, China) (Figure 5a). Meanwhile, the 5-cm-high evaporators were arranged on a 0.5 m × 0.5 m PS foam in a ten-by-ten array to verify the replicability (Figure 5a). Under natural conditions (Figure 5b), 99.43% KCl was extracted from the simulated K-rich fly ash leachate (Figure 5c). Meanwhile, the production of high-purity KCl (>99%) at a salt production rate (36.60 $g \cdot m^{-2} \cdot d^{-1}$) was maintained stable for 5 days (Figure 5d), demonstrating promising application prospects.

5.3 Discussion

5.3.1 Exclusion of the incorporation of K^+ into the NaCl crystal

For mixed NaCl/KCl crystals, the incorporation of K^+ into the NaCl crystal lattice could undermine selective separation based on differences in salt dissolution rates. However, such incorporation incorporation of K^+ into the NaCl crystal lattice is highly unlikely due to the significant mismatch in ionic radii (Na^+: 102 pm, K^+: 138 pm) and the difference in lattice energies (NaCl: -787 $kJ \cdot mol^-$

^{1}, KCl: -715 kJ·mol^{-1})[33]. As a result, during mixed NaCl-KCl crystallization, the two salts tend to form separate crystalline phases rather than a solid solution. Experimental observations confirm that K^{+} does not significantly incorporate into NaCl crystals under normal crystallization conditions. Thus, due to the higher dissolution rate, NaCl can completely dissolve into the source solution during selective dissolution process, leaving only the KCl crystals behind.

5.3.2 Impact of common-ion effect on salt dissolution behavior in mixed systems

The measured dissolution rates of individual salts can differ significantly from those observed when salts are dissolved together in a mixed system (Figures 5.1 and 5.3). This discrepancy arises primarily from the common-ion effect[34], which alters the solubility of each salt in the presence of other salts sharing the same ions. Taking NaCl and KCl as an example, their solubilities at 25 ^{o}C in pure water are approximately 359 g·L^{-1} and 344 g·L^{-1}, respectively. However, when both salts are simultaneously present, the increased concentration of common Cl^{-} ions suppresses the solubility of each salt to different extents (245 g·L^{-1} NaCl and 150 g·L^{-1} KCl). As a result, the solubility gap between NaCl and KCl becomes more pronounced under mixed conditions. Consequently, while the dissolution rate of KCl is about 1.3 times that of NaCl when measured individually, it increases to nearly 1.5 times in the mixed-salt

system.

5.3.3 Effect of the distribution of NaCl/KCl in mixed crystals on dissolution process

The spatial distribution of NaCl and KCl within mixed crystals can significantly influence the dissolution behavior and separation efficiency. If NaCl crystals are encapsulated by an outer layer of KCl, the dissolution process will initially be dominated by KCl, despite NaCl having a higher dissolution rate. In this scenario, NaCl remains inaccessible to the source solution until a sufficient portion of the KCl layer dissolves, exposing the underlying NaCl. As a result, the overall dissolution process is governed by the dissolution kinetics of KCl, and the selective separation of NaCl via dissolution rate differences becomes less effective. Conversely, if NaCl and KCl form separate crystalline domains or an interconnected but exposed structure, their dissolution will proceed more independently, allowing for more effective selective dissolution-driven separation. To achieve such favorable distributions, strategies such as controlling the particle size of the mixed crystals can be employed to ensure uniform dispersion and exposure of both salt phases during dissolution.

5.3.4 Multiple salts can be simultaneously removed through a single-step dissolution process

Real fly ash leachates typically contain not only NaCl and KCl, but also minor amounts of $CaCl_2$. However, in outdoor experiments, no detectable $CaCl_2$ was found in the final crystallized salt, indicating that the dissolution-rate-based separation method is applicable not only to the binary systems but also to more complex, real-world multicomponent salt mixtures. In such mixed crystals, both NaCl and $CaCl_2$ exhibit higher dissolution rates compared to KCl. As a result, following the nighttime dissolution process, only KCl remains in the solid phase, confirming the effectiveness of this strategy for selective removal of multiple highly soluble salts in a single step.

5.3.5 Potential application scenarios of this salt separation strategy

Compared to traditional salt extraction methods that rely on complex equipment, this evaporator features a simple design and can produce high-purity salt from mixed salt solutions within a single day-night cycle, using only solar energy as the primary power source. For future practical applications, the evaporator can be deployed to float on existing saltpans, greatly enhancing the scalability of KCl fertilizer recovery. In addition, this chapter demonstrates the system's potential for direct processing of industrial waste salts, offering a promising new approach for optimizing current salt separation technologies.

5.3.6 Industrial application of this salt separation strategy

In industrial applications, MVR is often used for salt crystallization due to its advantages, such as energy efficiency. However, since the evaporation process lacks selectivity, this typically results in the production of waste salt. To extract high-purity salt from this process, a dissolution system can be designed to selectively extract high-purity salt crystals from the mixed salt solids by controlling the dissolution process. A simple design could involve an inlet and outlet system, along with a mixing dissolution reaction chamber. After a certain period, the dissolution process is terminated, yielding high-purity salt solids.

5.4 Conclusion

This chapter pioneers a novel selective crystallization strategy by leveraging salt dissolution rate differences. We also achieved the direct production of high-purity salt from mixed solid salts solely through a single-step dissolution process. This strategy offers a scalable, energy-efficient, and environmentally friendly method for high-purity salt production, with significant implications for resource recovery and industrial processes.

5.5 Methods

5.5.1 Mechanistic mode development for selective salt crystallization

To design the selective crystallization system and simulate salt

crystallization states, we developed a mechanistic model by coupling fluid flow and ion transfer within the evaporator. The numerical simulation was performed using the finite element method in COMSOL Multiphysics 6.1, which integrates laminar flow and ion transport into a time-dependent solver[9,24]. Ion transfer in the non-woven fabric is governed by a combination of the continuity equation and the momentum equation, which are described by the Darcy's law[18]. More detailed descriptions of simulation setup, parameter selection, and underlying assumptions can be seen in Supplementary Text 5.1.

5.5.2 Solar-driven selective KCl crystallization from mixed NaCl/KCl solution

To fabricate the solar evaporator, a rectangular non-woven fabric was threaded through two narrow slots (3 × 0.5 cm^2, 3 cm apart) cut into the PS foam, ensuring proper alignment and structural stability. The assembled SSC was floated on the mixed source solution under one-sun illumination to facilitate solar-driven selective crystallization. To measure selective crystallization performance, crystallized salts were collected from the evaporator and dissolved in DI water. Then the water samples were diluted properly and measured by ICP-OES (720 ICP-OES, Agilent) and ion chromatography (CIC-D100, SHINE) to determine salt composition.

5.5.3 Direct high-purity salt production from mixed salt

Mixed salt crystals were prepared by evaporating a mixed salt solution to

dryness, followed by grinding to achieve a uniform particle size distribution. A measured amount of the ground mixed salt was then placed on the surface of the evaporator, and the structure was floated on the solution surface to facilitate selective dissolution. At regular time intervals, salt samples were collected and dissolved in DI water and diluted properly and measured by ICP-OES (720 ICP-OES, Agilent) and ion chromatography (CIC-D100, SHINE) to determine salt composition.

5.5.4 Practical fly ash leachate preparation

Municipal solid waste (MSW) fly ash was obtained from the Likeng waste incineration plant in Guangzhou (113°34’ E, 23°27’ N), China. The fly ash was mixed with deionized water at a 5:1 mass ratio, followed by static settling. The supernatant was collected as the fly ash leachate and subsequently filtered through a 0.22 μm membrane to remove suspended particles. The filtered leachate was then used as the source solution for outdoor high-purity KCl fertilizer production.

5.5.5 Characterizations

The surface morphology of non-woven fabric and salt crystals was characterized by SEM (TESCAN VEGA 3). The elemental distribution of the crystallized salts was analyzed using EDS equipped in the same instrument. The porosity and pore size distribution of non-woven fabric were measured by capillary flow porometer. The WCA of membranes was determined by the CA

meter (OCA20, DataPhysics). The UV-Vis-NIR diffuse reflectance spectra were recorded by an Agilent Cary 5000 spectrometer.

Reference

1 Chen, X. & Hu, W. Direct and efficient in situ rubidium extraction from potassium chloride salts. *Nat. Sustain.* (2024).

2 Yuan, J., Ma, H., Guo, R., Ma, X. & Komarneni, S. A case study targeting K fertilizer chemical synthesis with complete valorization of extraction by-products as an option. *Green Chem.* **22**, 6954–6966 (2020).

3 Huang, X. *et al.* A novel combined process for enhancing soluble salt recovery and reducing pollutant diffusion in municipal solid waste incineration fly ash. *J. Clean Prod.* **450**, 141892 (2024).

4 Li, J. *et al.* NaCl recovery from organic pollutants-containing salt waste via dual effects of aqueous two-phase systems (ATPS) and crystal regulation with acetone. *J. Clean Prod.* **260**, 121044 (2020).

5 Lanaro, G. & Patey, G. N. Molecular Dynamics Simulation of NaCl Dissolution. *J. Phys. Chem* **119**, 4275–4283 (2015).

6 Kline, W. E. & Fogler, H. S. Dissolution kinetics: Catalysis by salts. *J. Colloid Interface Sci.* **82**, 103–115 (1981).

7 Rezaei, M. *et al.* Reactive transport modeling of calcite dissolution in the fresh-salt water mixing zone. *J. Hydrol.* **311**, 282–298 (2005).

8 Wagner, C. The Dissolution Rate of Sodium Chloride with Diffusion and Natural Convection as Rate-Determining Factors. *J. Phys. Colloid Chem.* **53**, 1030–1033 (1949).

9 Zhang, L. *et al.* Highly efficient and salt rejecting solar evaporation via a wick-free confined water layer. *Nat. Commun.* **13**, 849 (2022).

10 Ni, G. *et al.* A salt-rejecting floating solar still for low-cost desalination. *Energy Environ. Sci.* **11**, 1510–1519 (2018).

11 Han, H., Park, Y., Kim, Y., Ding, F. & Shin, H.-J. Controlled dissolution of a single ion from a salt interface. *Nat. Commun.* **15**, 2401 (2024).

12 Klimes, J., Bowler, D. R. & Michaelides, A. Understanding the role of ions and water molecules in the NaCl dissolution process. *J Chem Phys* **139**, 234702 (2013).

13 Zhang, C., Yue, S., Panagiotopoulos, A. Z., Klein, M. L. & Wu, X. Dissolving salt is not equivalent to applying a pressure on water. *Nat. Commun.* **13**, 822 (2022).

14 Xu, K., Wang, C., Li, Z., Wu, S. & Wang, J. Salt Mitigation Strategies of Solar‐Driven Interfacial Desalination. *Adv. Funct. Mater.* **31** (2020).

15 Yang, K., Pan, T., Dang, S., Gan, Q. & Han, Y. Three-dimensional open architecture enabling salt-rejection solar evaporators with boosted water production efficiency. *Nat. Commun.* **13**, 6653 (2022).

16 Kuang, Y. *et al.* A High-Performance Self-Regenerating Solar Evaporator for Continuous Water Desalination. *Adv Mater* **31**, e1900498 (2019).

17 Zhang, L. *et al.* Passive, high-efficiency thermally-localized solar desalination. *Energy Environ. Sci.* **14**, 1771–1793 (2021).

18 Nield, D. A. & Bejan, A. *Convection in Porous Media*. 5th edn, (Springer, 2017).

19 Cussler, E. L. *Diffusion: mass transfer in fluid systems*. (Cambridge university press, 2009).

20 Meneses, J. P. C. H., Calcada, L. A., Scheid, C. M. & Magalhães, S. d. C. Determination of the convective mass transfer coefficient in the dissolution of NaCl particles in non-Newtonian fluids. *J. Nat. Gas Sci. Eng.* **45**, 118–126 (2017).

21 Shavandi, A., Silva, T. H., Bekhit, A. A. & Bekhit, A. E.-D. A. J. B. s. Keratin: dissolution, extraction and biomedical application. *Biomater. Sci.* **5**, 1699–1735 (2017).

22 Chen, X. *et al.* Spatially separated crystallization for selective lithium extraction from saline water. *Nat. Water* **1**, 808–817 (2023).

23 Xu, R., Kang, Y., Zhang, W., Pan, B. & Zhang, X. Two-dimensional MXene membranes with biomimetic sub-nanochannels for enhanced cation sieving. *Nat. Commun.* **14**, 4907 (2023).

24 Zhang, C. *et al.* Designing a next generation solar crystallizer for real seawater brine treatment with zero liquid discharge. *Nat. Commun.* **12**, 998 (2021).

25 Zhang, S. *et al.* Solar-driven membrane separation for direct lithium extraction from artificial salt-lake brine. *Nat. Commun.* **15**, 238 (2024).

26 Wu, L. *et al.* Highly efficient three-dimensional solar evaporator for high salinity desalination by localized crystallization. *Nat Commun* **11**, 521 (2020).

27 Yang, H. *et al.* Tailoring the salt transport flux of solar evaporators for a highly effective salt-resistant desalination with high productivity. *ACS Nano* **16**, 2511–2520 (2022).

28 Jiang, H., Zhang, Z. & Gong, W. Design and evaluation of a parallel-connected double-effect mechanical vapor recompression evaporation crystallization system. *Appl. Therm. Eng.* **179**, 115646 (2020).

29 Balis, E., Griffin, J. C. & Hiibel, S. R. Membrane Distillation-Crystallization for inland desalination brine treatment. *Sep. Purif. Technol.* **290**, 120788 (2022).

30 Culcasi, A. *et al.* Towards sustainable production of minerals and chemicals through seawater brine treatment using Eutectic freeze crystallization and Electrodialysis with bipolar membranes. *J. Clean Prod.* **368**, 133143 (2022).

31 Ahmaruzzaman, M. A review on the utilization of fly ash. *Prog. Energy Combust. Sci.* **36**, 327–363 (2010).

32 Simon, B. Dissolution rates of NaCl and KCl in aqueous solution. *J. Cryst. Growth* **52**, 789–794 (1981).

33 Raunio, G. & Rolandson, S. Lattice Dynamics of NaCl, KCl, RbCl, and

RbF. *Phys. Rev. B* **2**, 2098–2103 (1970).

34 AYOGU, P., Ezugwu, M. & Eze, F. Principle of Common-ion Effect and its Application in Chemistry: a Review. *J. chem. lett.* **1**, 77–83 (2020).

Supporting Information for Chapter 5

1. COMSOL modeling

To better understand how enhanced downward $MgSO_4$ transfer mitigates salt scaling, we developed a mechanistic model coupling fluidic flow and mass transfer within the evaporator (Figure 5.2a). Numerical simulations were performed using the finite element method (FEM) in COMSOL Multiphysics 6.1. Given the axisymmetric structure of the evaporator (Figure 5.2a), we constructed a two-dimensional (2D) axisymmetric model for simulation analysis. The model maintained an evaporator diameter of 11 mm, while the height was treated as a variable parameter determined by specific simulation conditions. The porous microstructure parameters, specifically a characteristic pore size of 14 μm and porosity of 82%, were assigned based on the nonwoven fabric's measured properties. The flow dynamics in the porous medium were governed by the continuity equation and the momentum equation, collectively forming the *Darcy Equations*[1]*:*

$$v=-\frac{k}{\mu}(\nabla p+\rho g) \qquad \text{Equation 5.2}$$

$$\nabla\cdot(u\rho)=Q_m \qquad \text{Equation 5.3}$$

where p is the pore pressure (Pa), μ is the dynamic viscosity of the fluid ($kg\cdot m^{-1}\cdot s^{-1}$), u is the velocity vector ($m\cdot s^{-1}$), ρ is the density of the fluid ($kg\cdot m^{-3}$), p is the pressure (Pa), ε_p is the porosity of the porous medium, k (m^2) is

the permeability of the porous medium, and Q_m is a mass source or sink (kg·m^{-3}·s^{-1})[2-4].

For salt transport, we used the *Transport of Diluted Species* module, which accounted for the diffusion of solutes through the porous medium. The transport equation applied was:

$$\frac{\partial C}{\partial t} = \nabla \cdot (D \nabla C) \qquad \text{Equation 5.4}$$

where C is the solute concentration (g·L^{-1}) and D is the mutual diffusion coefficient of salt (m^2·s^{-1}).

The *Kozeny–Carman* equation was used to estimate the permeability of the evaporator:

$$k = \frac{d_p^2}{180} \frac{\varepsilon_p^3}{(1-\varepsilon_p)^2} \qquad \text{Equation 5.5}$$

where d_p is the average pore size of the evaporator (m).

Due to the reduced solution-phase volume and increased diffusion length, the effective diffusion coefficient of species i in the evaporator can be expressed as:

$$D_i^e = \frac{\varepsilon}{\tau} D_i \qquad \text{Equation 5.6}$$

where D_i is the diffusive coefficient i in the source solution (m^2·s^{-1}), ε is the porosity of the evaporator and τ is the tortuosity of the evaporator.

For the boundary conditions, a fixed saturation concentration (245 g·L^{-1}

NaCl and 150 g·L^{-1} KCl) was applied at the top surface of the evaporator to simulate salt dissolution conditions. The bottom boundary of the evaporator was maintained in contact with water or mixed NaCl/KCl solution, establishing a stable concentration gradient to drive salt dissolution. The system temperature was held constant at 25°C, and salt concentrations remained stable during evaporation.

2. Regulation of salt dissolution rate by the evaporator height

In the evaporator, the salt dissolution rate is governed by height, as the convective mass transfer coefficient depends on the system's geometry. In convective mass transfer, momentum, energy, and mass transport share analogous mechanisms[40], with their relationship described by the following equations[5]:

$$k_{con} = \frac{h}{\rho C_p} = \frac{KN_u}{H} \cdot \frac{1}{\rho C_p} \qquad \text{Equation 5.7}$$

where k_{con} is the convective mass transfer coefficient (m·s^{-1}), h is the heat transfer coefficient (W·m^{-2}·K^{-1}), ρ is the density of the solution (kg·m^{-3}), C_p is specific heat capacity of solution (J·kg^{-1}·K^{-1}), K is thermal conductivity (W·K^{-1}·m^{-1}), H is the height of the evaporator (m), and N_u is Nusselt number.

From Equation 2, the convective mass transfer coefficient is inversely proportional to the evaporator height.

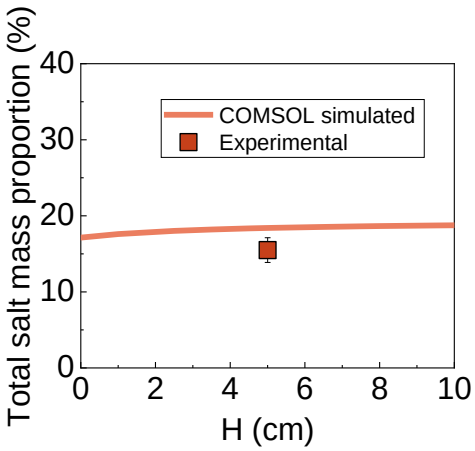

Supplementary Figure 5.1. COMSOL simulated the pure KCl mass proportion of the original solid after the dissolution process. Initially, the mass ratio of NaCl/ KCl in the mixed salt crystals was 1:1.

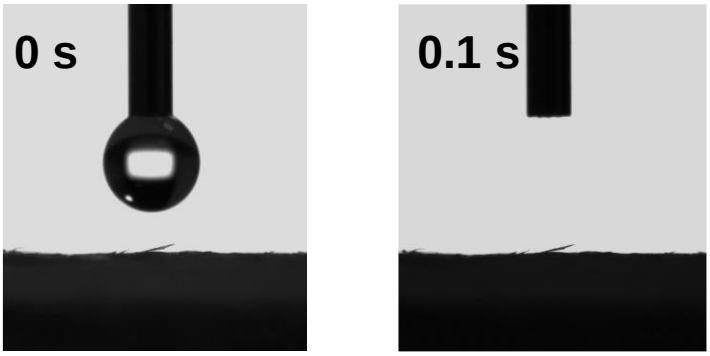

Supplementary Figure 5.2 Image of the water drop hanging above the non-woven fabric and the moment it touches the non-woven fabric surface. The non-woven fabric coated with carbon black can absorb a water droplet upon touching it within 0.1 s, indicating its high hydrophilicity

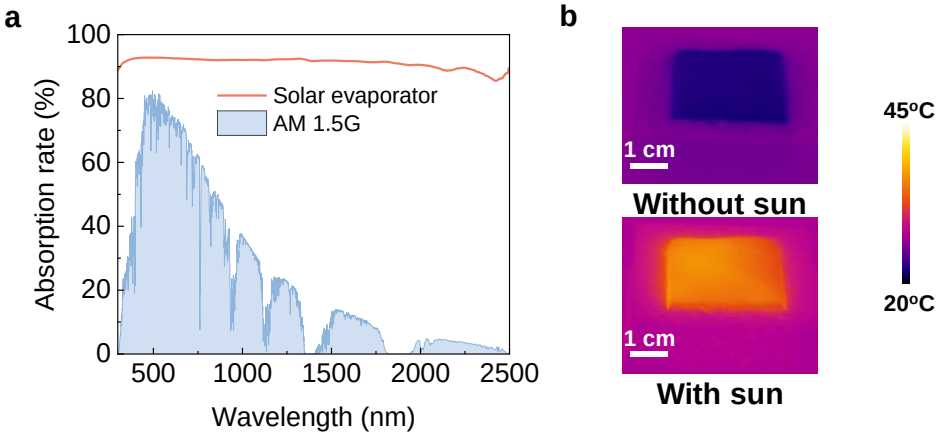

Supplementary Figure 5.3. (a) UV–Vis-NIR spectra of the non-woven fabric coated with carbon black. (g) Infrared thermal images of the bridge-like solar evaporator floating on water under 1 sun illumination.

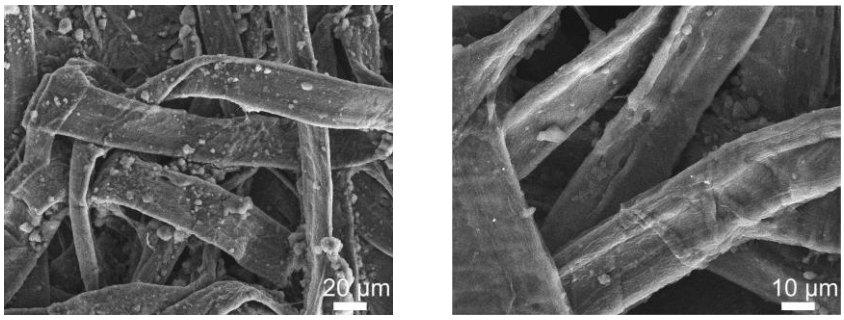

Supplementary Figure 5.4 SEM image of the non-woven fabric coated with carbon black, displaying hydrophilic microchannels that enable efficient ion transfer during solar evaporation.

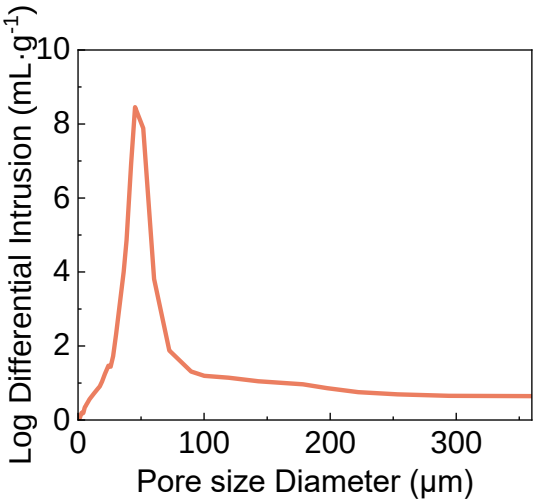

Supplementary Figure 5.5. Pore size distribution of the non-woven fabric coated with carbon black.

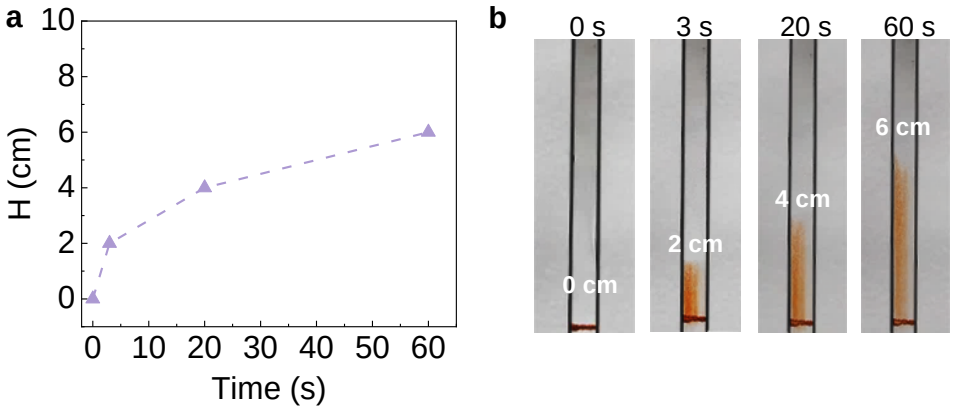

Supplementary Figure 5.6. Anti-gravity transport of water along the non-woven fabric.

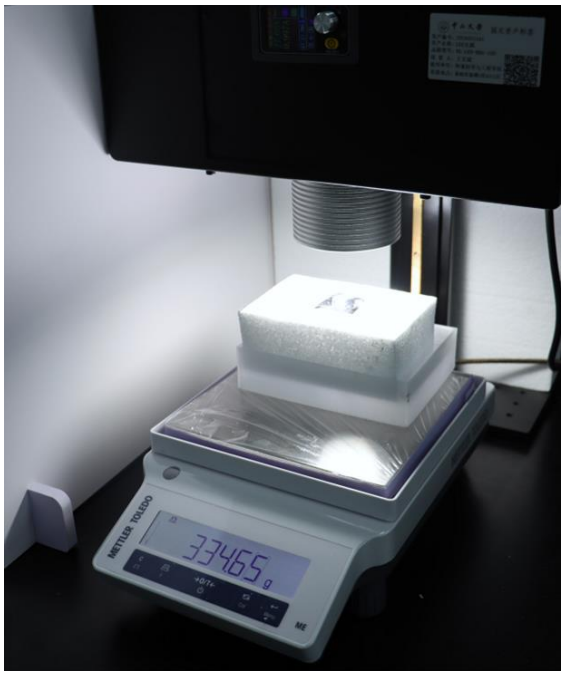

Supplementary Figure 5.7. Lab-made experimental setup for the solar evaporator evaluation.

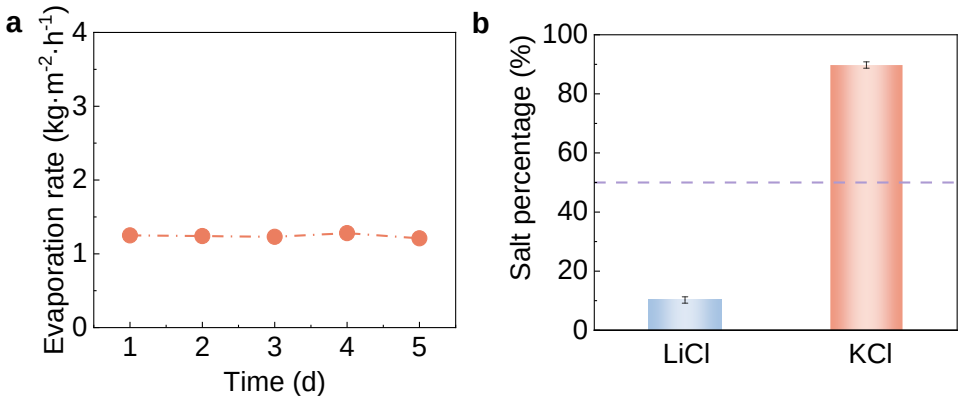

Supplementary Figure 5.8. Selective KCl crystallization from a mixed KCl/LiCl solution. Evaporation rate (a) and the LiCl/KCl proportion (b) within the crystallized salt when the evaporator floats on a mixed LiCl/KCl solution under one sun illumination. The total salt concentration was 40 g/L, with a mass ratio of LiCl to KCl of 1:1.

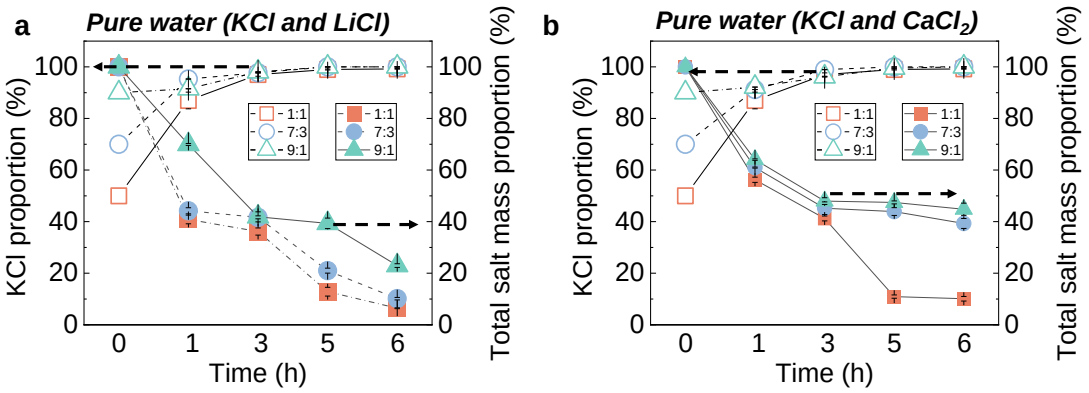

Supplementary Figure 5.9. KCl proportion in the mixed salt crystals and mass proportion of the original salt during dissolution of mixed KCl/LiCl (a) and $KCl/CaCl_2$ (b) crystals using their original solution. Mixed salt crystals were obtained by drying mixed salt solutions with equal mass ratios. The total salt concentration was maintained at 40 $g \cdot L^{-1}$ during the dissolution process, which was conducted at 25°C.

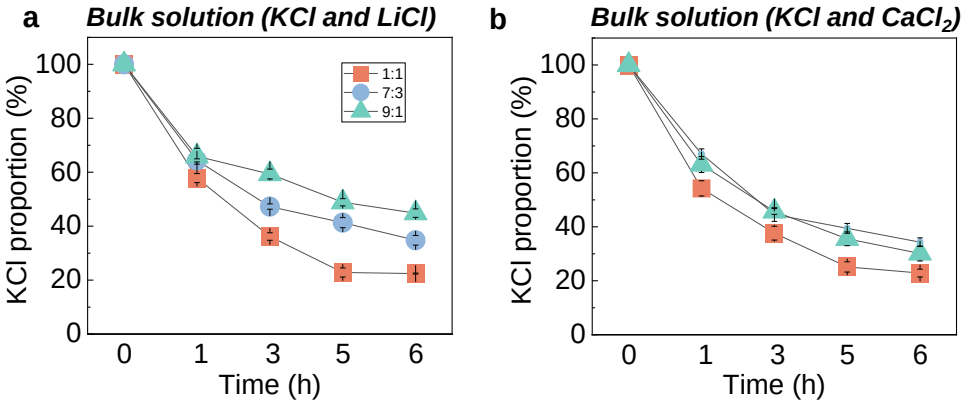

Supplementary Figure 5.10. Undissolved salt mass proportion of the original salt during dissolution of mixed KCl/LiCl (a) and $KCl/CaCl_2$ (b) crystals using their original solution. Mixed salt crystals were obtained by drying mixed salt

solutions with equal mass ratios. The total salt concentration was maintained at 40 $g \cdot L^{-1}$ during the dissolution process, which was conducted at 25°C.

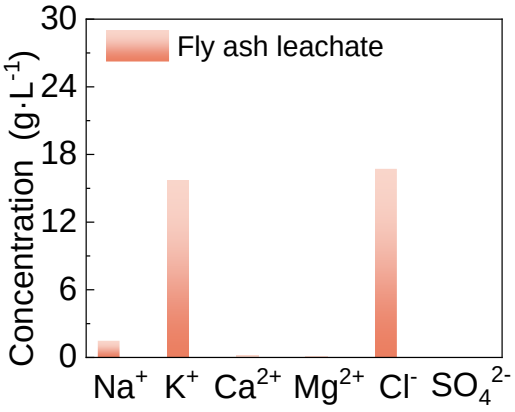

Supplementary Figure 5.11. Ion composition of fly ash leachate.

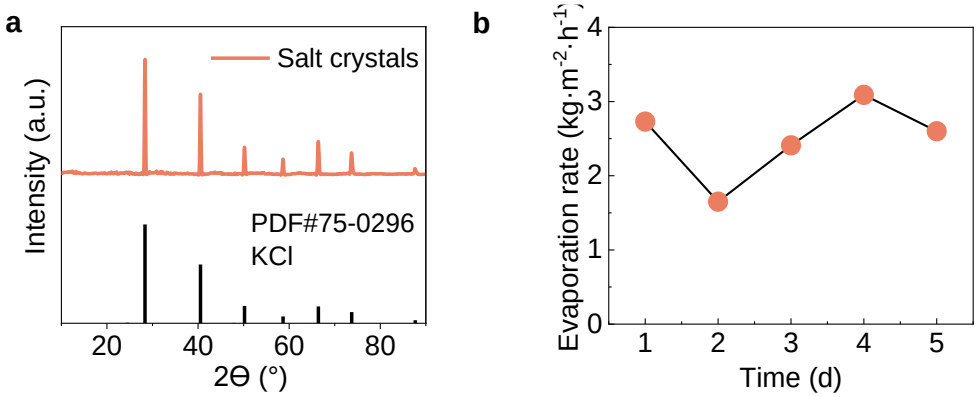

Supplementary Figure 5.12 Outdoor high-purity KCl extraction from fly ash leachate. (a) Average evaporation rate of the solar evaporator during 5-d selective crystallization test. (b) XRD pattern of the collected crystallized salt.

Reference

1 Mukherjee, R., Bhunia, P. & De, S. Long term filtration modelling and scaling up of mixed matrix ultrafiltration hollow fiber membrane: a case study of chromium(VI) removal. *J. Membr. Sci.* **570-571**, 204–214 (2019).

2 Yang, H. *et al.* Tailoring the salt transport flux of solar evaporators for a highly effective salt-resistant desalination with high productivity. *ACS Nano* **16**, 2511–2520 (2022).

3 Zhang, L. *et al.* Highly efficient and salt rejecting solar evaporation via a wick-free confined water layer. *Nat. Commun.* **13**, 849 (2022).

4 Tu, J., Yeoh, G.-H. & Liu, C. *Computational Fluid Dynamics (Third Edition)*. (Butterworth-Heinemann, 2018).

5 Kays, W. M., Crawford, M. E. & Weigand, B. *Convective heat and mass transfer*. Vol. 4 (McGraw-Hill New York, 1980).

6 Conclusion and Future Directions

6.1 Conclusions

This thesis comprehensively delineates selective crystallization technologies based on differences in ion diffusion and salt dissolution. The knowledge obtained will enable more sustainable and highly efficient extraction of high-purity salts from saline water, thereby meeting society's growing needs. The major conclusions are as follows:

1. We established a clear theoretical framework for selective crystallization by leveraging differences in ion diffusion. Building on this theory, we successfully extracted high-purity salts from complex mixed salt systems through a one-step interfacial evaporation process. Our findings not only advance fundamental understanding but also provide a robust method for high-purity salt production, offering significant implications for industrial applications.
2. To address real-world high-purity salt extraction scenarios, we designed a solar evaporator based on the theoretical framework presented in the first chapter. This allowed for the successful extraction of high-purity NaCl directly from real seawater without any pretreatment. This represents a significant step forward for our innovative technology toward practical implementation.
3. To broaden selective crystallization theory, we pioneered a novel

strategy that leverages salt dissolution rate differences to achieve high-purity salt production. Utilizing this strategy, we not only accomplished the one-step selective crystallization of high-purity salts from mixed solutions, but also successfully extracted high-purity salts directly from mixed solid salts through a single dissolution step. This strategy represents a significant theoretical innovation in selective crystallization technology, offering a scalable, energy-efficient, and environmentally friendly method for one-step high-purity salt production.

6.2 Future directions

While this thesis has significantly advanced interfacial evaporation selective crystallization, future research should focus on exploring promising avenues to further enhance their performance and ensure industrial viability in real-world applications.

1. Mitigating salt scaling in selective crystallization

Practical source water may contain minor salt species such as $MgSO_4$, which can co-crystallize with major components like NaCl, leading to the formation of a dense salt layer on the evaporation surface. This scaling layer significantly hinders water transport and can ultimately halt evaporation—a phenomenon known as salt scaling. While interfacial evaporation selective

crystallization holds great promise for high-purity salt extraction, it can also be susceptible to salt scaling under real-world conditions. Addressing this challenge requires the development of effective anti-scaling strategies, such as employing advanced materials or optimizing operational parameters, to ensure long-term efficiency and stability in practical applications.

2. Selection of strategies for high-purity salt extraction from mixed salt systems

The two selective crystallization strategies proposed here can be selected based on the specific characteristics of the mixed salt system encountered. If the differences in diffusion coefficients are more pronounced, the strategy based on diffusion-driven crystallization should be preferred. Conversely, if dissolution rate differences are more significant, the dissolution-based approach would be the better choice. By selecting the strategy that maximizes the difference in the relevant property (diffusion or dissolution), it becomes easier to achieve high-purity salt extraction.

3. Broadening the scope and integration of selective crystallization

Building on successful applications in real seawater and fly ash leachate, the next crucial step is to transfer these selective crystallization technologies to other saline water sources, like industrial brines and salt lakes, for high-purity salt extraction. Demonstrating their effectiveness across diverse ionic compositions and impurity profiles will enhance their universality and practical

value. This requires identifying valuable salts in various water sources and aligning the technology with current resource demands through targeted application and validation.

Simultaneously, integrating selective crystallization with existing industrial processes, like MVR, represents an important direction for future research. Such integration would not only drive innovation in current treatment technologies but also accelerate the adoption and scalability of selective crystallization technology. This effort will necessitate a comprehensive assessment of existing process workflows and the development of customized system designs tailored to specific industrial contexts.

4. Scaling up and field trials of selective crystallization

While the selective crystallization technologies demonstrated in this thesis show promising results in small-scale systems, their large-scale, real-world application remains limited. Scaling up laboratory findings often introduces new technical and operational challenges, potentially leading to performance deviations from initial expectations. This underscores the urgent need to investigate and validate the practical scalability of this technology. To bridge this gap, initiating pilot-scale studies and field tests as soon as possible is essential.

Publications from this thesis

Journal papers

1. **Yang Liu**, Changting Wang, Jinjuan Chen, Canjie Lin, Wenjie Kuang, Yekai Lian, Zhenle He, Zhen Wang, Jintong Lin, Khaled Bin Bandar, Saud Aldrees, Mohammed Alhussaini, Yifeng Shi, Jianping Cao, Bei Liu, Yi Jiang, Yetao Tang, Hanchao Zhang, Wenbin Wang & Peng Wang. Diffusion-driven selective crystallization of high-purity salt through simple and sustainable one-step evaporation. ***Nat Water*** (2025).

Note: Chapter 3 is a reprint of this published article.

2. **Yang Liu**, Yekai Lian, Jinjuan Chen, Amal Baqais, Changting Wang, Jiaqi Chen, Canjie Lin, Chao Wang, Zhenle He, Bei Liu, Yi Jiang, Dalal Matar Al Shamsi, Ahmed Al Raeesi, Mohsen Sherif, Jianping Cao, Wenbin Wang, Peng Wang. Simple mass transfer regulation achieves the longest stable scaling-free Zero Liquid Discharge of seawater desalination brine without chemical additive. (Submitted to ***Science Advances***)

3. **Yang Liu**, Jinjuan Chen, Changting Wang, Yekai Lian, Canjie Lin, Chao Wang, Zhenle He, Bei Liu, Yi Jiang, Dalal Matar Al Shamsi, Ahmed Al Raeesi, Mohsen Sherif, Jianping Cao, Wenbin Wang, Peng Wang. Dissolution-driven salt separation method for high-purity salt

extraction. (To be submitted)